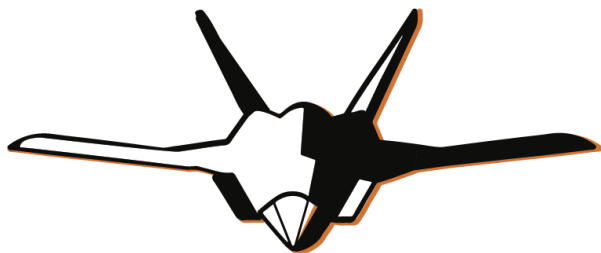




Professor: Maurizio Boffadossi

Aerodynamic Design of The STAD-1 Kestrel



Authors:

Personal code	SURNAME	NAME
10667431	Baio	Matteo
10672007	Magni	Thomas
10685222	Matteucci	Niccolò
10701065	Nazir	Ali
10674294	Rancati	Elia
10683447	Schifone	Marco

Table of Contents

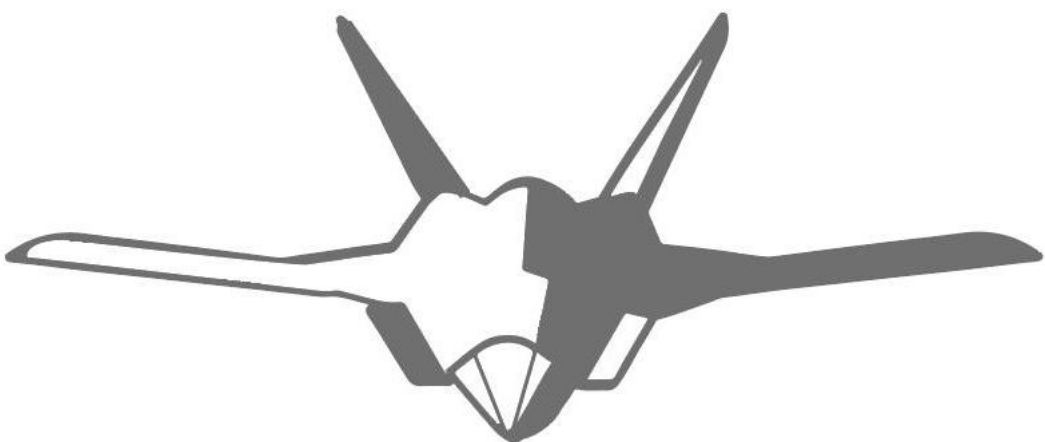


Table of Contents

The table of contents is reported below.

Table of Contents	I
List of Images	IV
List of Tables	VI
1. Problem Introduction and Design Inputs.....	1
2. Initial Aerodynamic Sizing	5
2.1. Wing Planform Considerations	5
2.2. Wing Root-Fuselage Interaction	7
3. Wing Planform Design	10
3.1. Results	11
3.2. Spanwise Distribution	12
3.3. Sweep Sensitivity Analysis	13
4. Tail Volume Sizing	15
4.1. Results	17
5. High-Lift and Control Surfaces	20
5.1. High-Lift Design	20
5.1.1. High-Lift First Sizing	21
5.1.2. Second Sizing Iteration	22
5.2. Flapped Polars	26
6. Higher Order Methods Setup	27
6.1. DUST: Mid-Fidelity Aerodynamic Solver	27
6.2. SU2: High Fidelity CFD Code	27
6.3. Euler Analyses	28
6.4. RANS Analyses	28
6.5. Meshing for SU2	29
6.5.1. Mesh Topology	29
6.5.2. Surface Mesh Generation	30
6.5.3. Volume Mesh Generation	30
6.5.4. Grid Quality Criterions	30
6.5.5. Boundary And Freestream Conditions	31
6.5.6. Grid Convergence	32
6.6. STAD-1 Model in DUST	32
6.6.1. Lifting Line Vortex Model	33
6.6.2. VLM TE Vortex Model	33
6.7. DUST Sensitivity Analysis	33

6.7.1. Mesh Size	33
6.7.2. Time Step.....	34
6.7.3. Fuselage Gap	35
6.7.4. Wake Box.....	36
6.8. DUST Comparison with Euler	37
6.8.1. Isolated Wing	37
6.8.2. Complete Aircraft	39
7. Wing Airfoil Selection and Analysis.....	41
7.1. Euler Analyses.....	42
7.2. RANS Analyses	47
8. Complete Aircraft Euler Analyses	49
8.1. Tail Fuselage Section Design.....	49
8.2. Tail Airfoil Selection.....	51
9. LEX Design.....	52
9.1. LEX First Sizing	52
9.2. Root Chord Analysis	54
9.3. Leading Edge Sweep Analysis.....	55
9.4. LEX Interaction with Air Intake.....	56
9.5. LEX Design Verification and Comparison	57
9.6. Rans Problem Setup	61
10. Adjoint Optimization	63
10.1. Adjoint Optimization Method on SU2	63
10.2. Isolated Wing Optimization	64
10.3. Results	65
11. Conclusions and Open Points	69
Acknowledgements.....	70
References	71
A. Appendix.....	A-1
A.1. Wing Position	A-1
A.2. Ruddervator	A-2
A.3. Planform Design Validation	A-3
A.4. RANS Grid Convergence	A-4
A.5. Full Body Grid Convergence	A-5
A.6. DUST Mathematical Model.....	A-7
A.6.1. Hypothesis and Governing Equation.....	A-7
A.6.2. Solution of Lagrange Equation.....	A-8
A.6.3. Solution of Poisson Equation.....	A-9
A.6.4. Dynamic System and Time Evolution.....	A-11

Table of Contents

A.6.5. Load Computation	A-12
A.7. More on DUST	A-14
A.7.1. DUST Workflow	A-14
A.7.2. DUST Analysis Architecture	A-14
A.8. Validation on ONERA M6	A-16
A.8.1. ONERA M6 Geometry	A-16
A.8.2. DUST Model	A-16
A.8.3. SU2 Model.....	A-17
A.8.4. Subsonic Testing.....	A-17
A.8.5. Transonic Testing.....	A-19

List of Images

Summary of all the figures present in this document.

Figure 1 - STAD-1 external shape and lofting.....	2
Figure 2 – Fuselage section's lofting examples.....	2
Figure 3 - Lambda wing (left) and trapezoidal wing (right) configurations from the conceptual design.....	5
Figure 4 - Lift Slope with AR [4].....	6
Figure 5 - Exposed Area and Planform Area [1].....	6
Figure 6 - Isobar effects on a swept wing [6].....	8
Figure 7 - F-35 Leading Edge Extensions [8].....	8
Figure 8 - Supersonic Area Rule [RAYMER].....	9
Figure 9 – Example of Supersonic Area Rule application on an early fuselage.....	9
Figure 10 - Isolated Designed Lambda Wing OpenVSP geometry.....	10
Figure 11 - Lambda Wing with simplified fuselage OpenVSP geometry.....	11
Figure 12 – Planform sizing results with legend.....	12
Figure 13 – Spanwise lift distribution at $Ma = 0.85$	13
Figure 14 - Sweep sensitivity results for configuration with legend.....	14
Figure 15 - Tail volume coefficients geometry definitions.....	15
Figure 16 - OpenVSP complete V-tail model.....	17
Figure 17 – V-tail aerodynamic results with legend.....	18
Figure 18 – NACA 65 configuration results.....	19
Figure 19 - Flaps considered topologies [1].....	20
Figure 20 - Typical airfoil maximum lift increment for different devices.....	21
Figure 21 – Reference and Flap Surfaces Definition [1].....	21
Figure 22 - High-lift surface OpenVSP visualization.....	22
Figure 23 - Theoretical airfoil lift increment for plain flaps [1].....	23
Figure 24 - Empirical correction for plain flap lift increment [1].....	23
Figure 25 -Rate of change of airfoil lift coefficient with leading edge flap deflection [11]	24
Figure 26 - Correction factor plots for leading edge flap [11]	24
Figure 27 - Estimation of the drag contribution coefficients [10]	25
Figure 28 - Leading edge high-lift surfaces polar [12]	26
Figure 29 – Polars of different configurations at sea level (without landing gear drag).....	26
Figure 30 - On the left the right lower edge of the air intake, on the right the intersection between the nozzle and the fuselage.....	30
Figure 31 - Grid convergence results for the isolated wing for Euler.....	32
Figure 32 – Mesh size sensitivity analysis.....	34
Figure 33 – Compare between coarse and refined mesh	34
Figure 34 – Time step sensitivity analysis	35
Figure 35 – Compare between biggest and smallest time step	35
Figure 36 – Fuselage gap sensitivity analysis	36
Figure 37 – Compare between negative and positive fuselage gap	36
Figure 38 – Wake box sensitivity analysis	37
Figure 39 – STAD-1 wing surface pressure distribution at Mach 0.30 and AOA 5°.....	38
Figure 40 – STAD-1 wing surface pressure distribution at Mach 0.30 and AOA 15°.....	38
Figure 41 – Aerodynamic force coefficient for STAD-1 isolated wing at $Ma = 0.30$ and $h = 15,000\text{ft}$	39
Figure 42 – STAD-1 wing surface pressure distribution at Mach 0.30 and AOA 5° (left) and 15° (right).	39
Figure 43 – Aerodynamic force coefficient for STAD-1 aircraft at $Ma = 0.30$ and $h = 15,000\text{ft}$	40
Figure 44 – Initial wing Euler CFD analysis at $Ma = 0.85$ and 15,000 ft.	43
Figure 45 - Case 1 (Left) and Case 2 (Right) Euler analysis at $Ma = 0.85$ and 15,000 ft.	43
Figure 46 – NACA 65 Euler CFD analysis at $Ma = 0.85$ and 15,000 ft.	45
Figure 47 - Wing tip cap construction section and geometry.	45
Figure 48 - NACA 65 with tip cap Euler CFD analysis at $Ma = 0.85$ and 15,000 ft.	46
Figure 49 - C_p comparison between inviscid (left) and viscous (right) simulations.	48
Figure 50 – Initial Tail Section Geometry	50
Figure 51 - Modified Tail Section Geometry.	50
Figure 52 - Final Tail Section Geometry.	51
Figure 53 – V-tail initial (left) and final (right) tail configuration with Euler CFD.	51
Figure 54 - LEX influence on the CL_{max} [4].	52

List of Images

Figure 55 – Example of integral loads convergence for LEX configuration	53
Figure 56 – wake envelope at $Ma = 0.30$, $h = 15,000\text{ft}$ and $\alpha = 15^\circ$	53
Figure 57 -Vortex lift of a slender delta wing [24]	54
Figure 58 – LEX 2D sketch on FreeCAD for chord analysis	54
Figure 59 – Effect of different LEX root chord length on aerodynamic coefficients	55
Figure 60 – LEX 2D sketch on FreeCAD for sweep analysis.....	55
Figure 61 – Effect of different LEX LE sweep on aerodynamic coefficients.....	56
Figure 62 - Fighter intake modeling from [26].....	56
Figure 63 - Comparison between the air intake designs.....	57
Figure 64 - Zoom in on the vortex's streamlines.	58
Figure 65 - On the left LEX 65°, on the right LEX 70°.	58
Figure 66 - Flow streamlines close to the LEX for $\alpha = 5^\circ$ (left) and $\alpha = 7^\circ$ (right).	59
Figure 67 - Flow streamlines close to the LEX for $\alpha = 10^\circ$	59
Figure 68 - Final Configuration Euler Results Top View ($Ma = 0.85$ at 15,000 ft).	60
Figure 69 - Final Configuration Euler Results Side View ($Ma = 0.85$ at 15,000 ft).	60
Figure 70 - Final Configuration Euler Results Iso View ($Ma = 0.85$ at 15,000 ft).....	60
Figure 71 - Section of the wing near the tip.....	61
Figure 72 - Section of the lex and the wing.	62
Figure 73 – FFD boxes and control points.	64
<i>Figure 74 - Convergence history of the objective function.</i>	65
Figure 75 - Mach number (left picture) and pressure coefficient over the wing (right picture) before and after the optimization process.	66
Figure 76 – Sectional airfoil shape and pressure coefficient extracted at $y/b = 0$	66
Figure 77 - Sectional airfoil shape and pressure coefficient extracted at $y/b = 0.23$	67
Figure 78 - Sectional airfoil shape and pressure coefficient extracted at $y/b = 0.6$	67
Figure 79 - Sectional airfoil shape and pressure coefficient extracted at $y/b = 0.83$	67
Figure 80 - Initial and optimal polar curve (left), $CL - \alpha$ curve (right).	68
Figure 81 - Initial and optimal lift-to-drag ratio.....	68
Figure 82 – Initial and final V-tail OpenVSP geometry.	A-2
Figure 83 - CL curve OpenVSP and semi-empirical formula comparison.	A-3
Figure 84 - Grid convergence results for the isolated wing for RANS.....	A-4
Figure 85 - Full body grid convergence.	A-5
Figure 86 – Full body grid convergence with coefficients obtained considering only the wing	A-6
Figure 87 – Scheme of the wake panel to particle conversion in DUST	A-11
Figure 88 – suggested workflow for DUST	A-14
Figure 89 – DUST analysis MATLAB code architecture	A-15
Figure 90 – ONERA M6 wing original wind tunnel testing model.....	A-16
Figure 91 – ONERA M6 wing DUST panel model.....	A-17
Figure 92 – ONERA M6 integral loads at Mach 0.30 and AOA 3.06°	A-18
Figure 93 – ONERA M6 surface pressure distribution at Mach 0.30 and AOA 3.06°	A-18
Figure 94 – ONERA M6 chordwise pressure distribution at Mach 0.3000 and AOA 3.06°	A-19
Figure 95 – ONERA M6 integral loads at Mach 0.84 and AOA 3.06°	A-20
Figure 96 – ONERA M6 surface pressure distribution at Mach 0.84 and AOA 3.06°	A-20
Figure 97 – ONERA M6 chordwise pressure distribution at Mach 0.84 and AOA 3.06°	A-21

List of Tables

Summary of all the tables present in this document.

Table 1 - Endurance Mission new data	3
Table 2 – Rapid Response Mission new data	3
Table 3 - Sustained Turn new data	3
Table 4 - Instantaneous Turn new data.....	3
Table 5 - Lambda Wing Section Data.....	10
Table 6 - Lambda Wing global geometric parameters	10
Table 7 - Airfoils selection for first lambda wing analyses	11
Table 8 - Parasite Drag tool results.....	11
Table 9 - Sensitivity analysis data	13
Table 10 – Resulting Tail volume method parameters	16
Table 11 - Tail Geometry Data	16
Table 12 - V-tail model drag coefficients	17
Table 13 - Control surfaces sections data	22
Table 14 - Lift variations with high-lift devices.....	22
Table 15 - High-lift surfaces lift increments	24
Table 16 - High-lift surfaces drag increments.....	26
Table 17 - Values imposed for inlet and outlet marker.....	31
Table 18 – Free stream conditions for DUST sensitivity analysis	33
Table 19 - Isolated Wing Flow Conditions	42
Table 20 – NACA 64 airfoil configuration over the wing.....	43
Table 21 – Coefficient for NACA 64 designs, from Euler analysis at $Ma = 0.85$ and 15,000 ft.....	44
Table 22 – Coefficient for NACA 64 designs, from Euler analysis at $Ma = 0.50$ and 15,000 ft.....	44
Table 23 – NACA 65 airfoil configuration over the wing.....	45
Table 24 - NACA 65 Results at $Ma = 0.85$ and 15,000 ft.....	46
Table 25 - NACA 65 Results at $Ma = 0.50$ and 15,000 ft.....	46
Table 26 - Case 4 airfoils configuration	46
Table 27 - Case 5 airfoils configuration	47
Table 28 - Case 7 airfoils configuration	47
Table 29 - Results for supercritical airfoils at $Ma = 0.85$	47
Table 30 - Comparison between inviscid and viscous simulations for the wing at $Ma = 0.85$	48
Table 31 – Complete Aircraft Flow Conditions	49
Table 32 - Comparison between the two designs	57
Table 33 - Final Configuration Results for the Design Condition	61
Table 34 - Summary of the STAD-1 wing optimization problem	65
Table 35 - Results of the optimization process.....	65
Table 36 - Ruddervator geometrical parameters and airfoils	A-2
Table 37 - Different meshes prepared to investigate the convergence	A-5
Table 38 - ONERA M6 geometrical data	A-16
Table 39 – ONERA M6's DUST panelization parameters.....	A-16
Table 40 – ONERA M6 subsonic testing free stream condition	A-17
Table 41 – ONERA M6 transonic testing free stream condition.....	A-19

1. Problem Introduction and Design Inputs

An introduction of the STAD-1 aircraft, its data and mission goals and its aerodynamic design objectives are here briefly presented.

The objective of the problem presented herein is to design, from an aerodynamic point of view, an aircraft with a lambda wing configuration (after selecting it as the optimal wing shape), denoted as “STAD-1 Kestrel”. The design takes input data from a conceptual design done during the “Metodi di Progetto di Velivoli” course, and subsequently every aspect of the aerodynamics (mainly the wing) is designed up to a preliminary level. The STAD-1 Kestrel is an unmanned combat aerial vehicle created on the following request for proposal:

*“Design a **remotely-piloted attack aircraft** for fighting primarily **low-speed manned flying targets**, including **attack helicopters** and **propeller-driven fixed-wing aircraft** (either attack or unarmed/cargo). The aircraft should have also **ground strafing capabilities**. The **range in an operational mission should at least 1,500 km**, including the outbound and return phases. Airborne or land infrastructure and other considerations are required. Target applications are among **current high-tension/open warfare scenarios**.”*

After in-depth preliminary research on the topic, the output is a turbofan powered aircraft capable of sustaining a low stall speed, good maneuverability, a high transonic maximum speed and a long endurance. Thus, a high L/D is required, as well as good transonic behavior. After some changes made in the preliminary design done in “Laboratorio di Progetto di Velivoli”, the design point has been selected with a nominal wing loading $(M/S)_{Gross} = 260.28 \text{ kg/m}^2$ and nominal thrust to weight ratio $T/W = 0.652$, related to the estimated mass of 6,913 kg. The flight conditions that are the focus of the aerodynamic design are still taken from the conceptual design and are reported below:

- **Loiter flight** at $M_a = 0.50$ and 15,000 ft as the main driver of the design since it requires the maximum L/D in order to achieve the requirements on the loitering time. The condition is analyzed with the fuel required for takeoff, climb and cruise detracted. Furthermore, it will be the focus of the aerodynamic design presented in this chapter.
- **Sustained turn** at $n_{SUS} = 5.1$, $M_a = 0.85$ and 15,000 ft with 80% of the MTOM. This condition is needed to assess the drag rise and buffeting effects on the aircraft and to also evaluate if the engine has enough thrust to achieve a sustained turn. Furthermore, it will be the focus of the aerodynamic optimization presented in subsequent chapters.
- **Instantaneous turn** at $n_{INS} = 8.0$, $M_a = 0.77$ and 15,000 ft with 80% of the MTOM. This condition is needed to verify the maximum obtainable lift in a maneuvering condition.

These flight conditions also have different values of M/S since each condition is evaluated after considering the consumed fuel before the considered condition and after (and the selected payload mass).

Also, in the preliminary design done in the “Laboratorio di Progetto di Velivoli” course, a fuselage has been designed for the aircraft, which is proposed in Figure 1. The fuselage is made to contain all the required systems and payload while also taking into consideration aspects of low radar observability and aerodynamics. It has been obtained using the lofting procedure explained by [1], by defining some meaningful cross-sections, then longitudinal control lines are used in order to “loft” the control sections following them and obtaining the fuselage shape. The choices made for the fuselage also impact the wing design, so a small recap has been made.

STAD-1 KESTREL

MTOM: 7153 kg + 450 kg (external)
NTOM: 6913 kg

Length: 11.3 m
Span: 10.7m

Height: 3.0 m
Angles: 60°

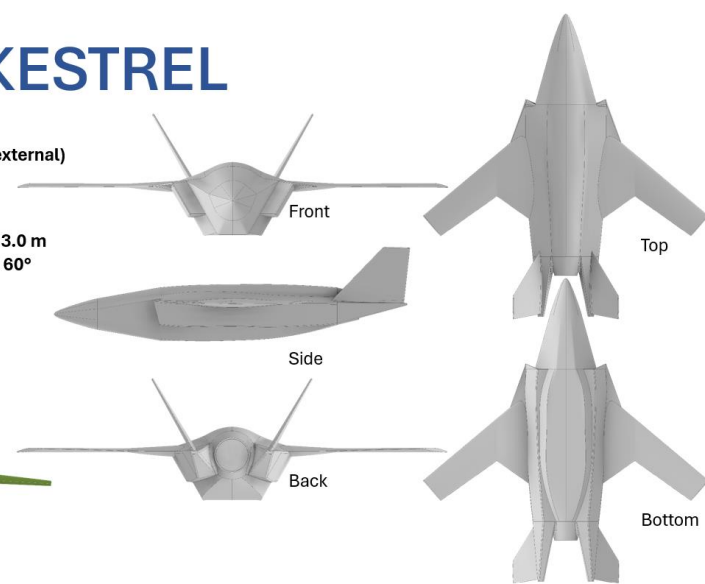
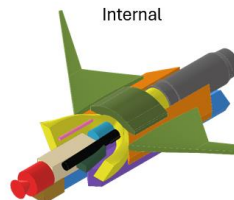
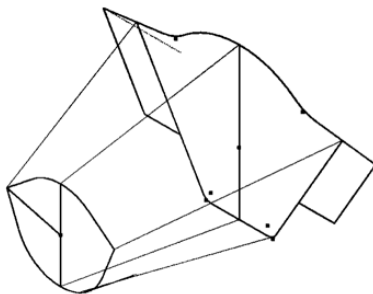


Figure 1 - STAD-1 external shape and lofting.

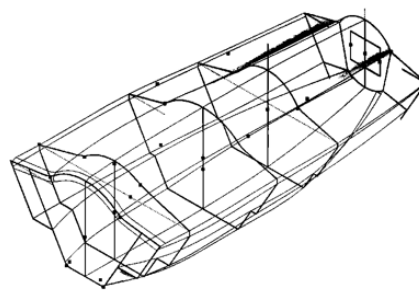
The radar cross section factors that influence the shape of the whole aircraft (considering lifting and non-lifting parts) are the following [2]:

- **Planform shaping and alignment:** This means that every angle for the aircraft must be as similar as possible to each other. In Figure 1 it's shown how the angles for both the fuselage lateral portion and the v-tail are 60°, as well as how both wing and tail have a leading edge sweep of 60°.
- **Relative angles:** this relates to not having surfaces that are 90° between each other, as this would cause a refraction of radar waves and increase the radar signature of the aircraft. This, for example, leads to the need of designing a V-tail rather than a classical horizontal and vertical tail surface combination. With the same logic, considering the least possible gaps in the shape (for example the gap in slotted control surfaces) should be taken as practice.

The components are placed inside the fuselage and an external design is done using control sections and control lines as shown in Figure 2. This also has the objective of designing a lifting fuselage, which is done by having a relatively slim shape from a vertical point of view.



Nose Section Lofting.



Central Section Lofting.

Figure 2 – Fuselage section's lofting examples.

With these considerations made, it is possible to subsequently design the wing; the first step is to evaluate its required performance.

Problem Introduction and Design Inputs

For all three mission phases, the following formula is used to evaluate the required lift coefficient of the wing:

$$C_L = \frac{W/S \cdot n}{0.9 \cdot 1/2 \cdot \rho \cdot V^2} \quad (1.1)$$

Where W/S is the wing loading (namely M/S multiplied by the gravitational acceleration), ρ is the air density, V is the flight speed and n is the load factor (which is equal to 1 on the first two conditions). The 0.9 coefficient is considered to account for the lift that the wing should provide to compensate for the wing region covered by the fuselage [3].

It is consequently possible to compute the lift coefficient of the equivalent airfoil C_L^a :

$$C_L^a = \frac{C_L}{\cos(\Lambda_{LE})^2} \quad (1.2)$$

Where Λ_{LE} is the sweep angle at leading edge.

For the chosen flight conditions, the data are reported in the tables below; in particular, the new wing loadings \bar{M}/S values are reported. The values are reported only for the final Λ_{LE} , as reporting the values for each range considered in the sensitivity analysis would be too abundant.

Endurance Mission $M_a = 0.50$ and 15,000 ft

	$\bar{M}/S \left[\frac{kg}{m^2} \right]$	C_L^{wing}	C_L^a	$\rho [kg/m^3]$
<i>Initial condition</i>	255.40	0.28	0.47	0.7708
<i>Final condition</i>	228.92	0.25	0.43	0.7708

Table 1 - Endurance Mission new data.

Rapid Response Mission $M_a = 0.85$ and 10,000 ft

	$\bar{M}/S \left[\frac{kg}{m^2} \right]$	C_L^{wing}	C_L^a	$\rho [kg/m^3]$
<i>Initial condition</i>	257.27	0.07	0.12	0.9050
<i>Final condition</i>	255.90	0.07	0.12	0.9050

Table 2 – Rapid Response Mission new data.

Sustained Turn $M_a = 0.85$ and 15,000 ft (80% MTOM)

$\bar{M}/S \left[\frac{kg}{m^2} \right]$	n_{SUS}	$n_{SUS} C_L^{wing}$	$n_{SUS} C_L^a$	$\rho [kg/m^3]$
208.22	5.1	0.40	0.68	0.7708

Table 3 - Sustained Turn new data.

Instantaneous Turn $M_a = 0.77$ and 15,000 ft (80% MTOM)

$\bar{M}/S \left[\frac{kg}{m^2} \right]$	n_{INS}	$n_{INS} C_L^{wing}$	$n_{INS} C_L^a$	$\rho [kg/m^3]$
208.22	8.0	0.77	1.30	0.7708

Table 4 - Instantaneous Turn new data

Another value worth mentioning for the aerodynamic sizing is the maximum lift coefficient $C_{L,max}$, whose target is set to 1.25. The value may seem low, but it's due to a larger wing area compared to standard combat aircraft. Also, the minimum lift to drag ration L/D required in the loiter condition to satisfy the aircraft's performance is equal to 14.

2. Initial Aerodynamic Sizing

First qualitative considerations related to the wing design are here reported in this chapter.

In order to satisfy the many aerodynamic requirements in a relatively short time, it is necessary to consider similar aircraft design, understanding and choosing some of their features in order to greatly reduce the amount of design iterations.

This approach can be seen as a study of similar aircraft (mainly latest generation fighters, UCAV and attack aircraft) to understand which are their design best-practices. Unfortunately, often, there are not publicly available data and studies. It is particularly relevant for complex aerodynamic features that are not easy to simulate without doing extensive CFD analyses or tunnel testing, and for RCS minimizations, since even if many methods have already been considered in the conceptual design report, it is complex to verify their effectiveness.

Other considerations come from design books and papers, from which it is possible to find more general design methodologies typically in the form of semi-empirical methods and analyses based on older aircraft. Such procedures are still valuable in a modern aerodynamic design.

From these semi-empirical methods and literature considerations, by comparing them with modern aircraft, it is possible to start the initial aerodynamic sizing.

2.1. Wing Planform Considerations

Once a consideration on a small number of airfoils is done, the wing planform design started. The wing planforms chosen in the conceptual design phase, which are shown in Figure 3, have been considered and are denoted as lambda wing and trapezoidal wing. The trapezoidal wing configuration has been discarded due to its low L/D when designed and analyzed in the "Laboratorio di Progetto di Velivoli" course. For this reason, the design process described herein considers only the lambda wing configuration.

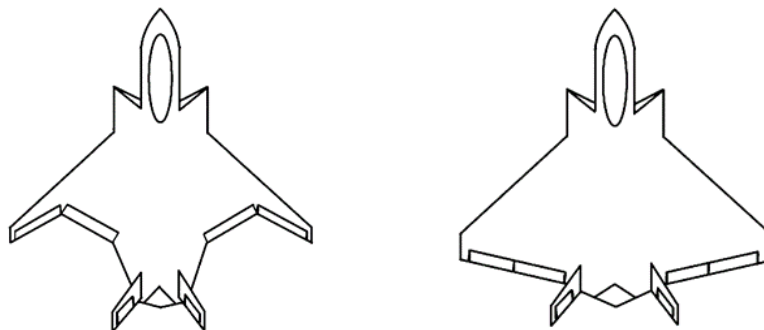


Figure 3 - Lambda wing (left) and trapezoidal wing (right) configurations from the conceptual design.

The value of AR of the STAD-1, from the conceptual design and from the results of the sizing, lay in the range of medium aspect ratio (Figure 4). For this value some semi-empirical methods might not be precise enough or might need further corrections.

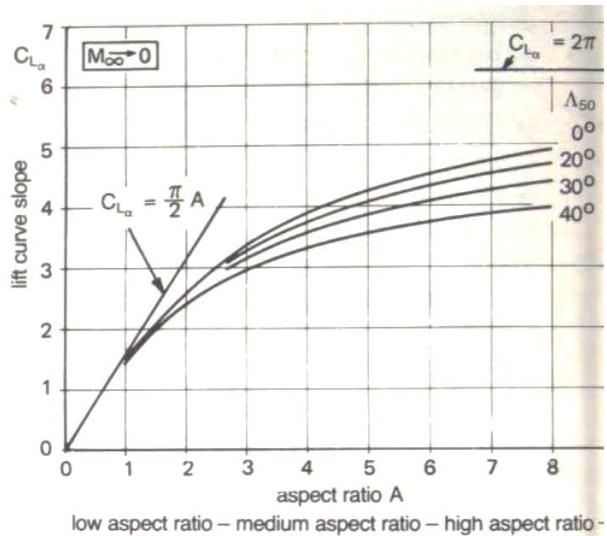


Figure 4 - Lift Slope with AR [4].

The wing has been first sized considering the wing area obtained from conceptual design. The wing area S_{Wing} is defined as the true planform area as depicted in Figure 5.

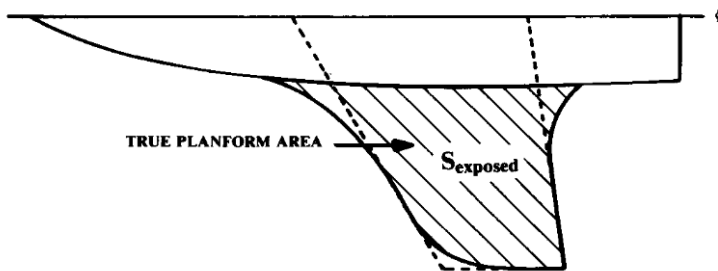


Figure 5 - Exposed Area and Planform Area [1].

Other than the planform's overall shape, defining the wing geometry means defining the following parameters:

- Sweep angle Λ .
- Root chord.
- Taper ratio (and so Tip chord).
- Twist distribution.
- Incidence.

The geometry has been defined with OpenVSP's geometry design tool through the following approach:

1. Λ is found by imposing a suitable leading edge sweep angle obtainable without changing the AR substantially (in order to satisfy the RCS constraint), and consequently depending on the chosen wing geometry.
2. For the root chord and the taper ratio, a first process based on the geometry definition on OpenVSP is taken in order to obtain the aspect ratio considered in the conceptual design. With such requirements the planform is almost completely defined since modifying other parameters will result in a geometrically unfeasible planform or a different AR . The airfoil thickness at the root was defined by the Korn equation (7.1) considering an increment of 30% [1].

3. The twist is chosen to have a lift distribution as close as possible to an elliptical one without having the wing tips stalling before the inner portion of the wing.
4. The incidence is chosen as 0° since very low values of incidence are considered for fighters; furthermore, the incidence value is typically a result of an aerodynamic optimization on the entire aircraft which is not possible at this design stage.
5. Lastly, dihedral angle is preliminary set to 0° for RCS reason. In a latter design phase, the wing should be placed in a such way that the aircraft has 0° dihedral in the deformed configuration (as it is done in the F-22 [5]).

With the first baseline geometry defined with the geometry builder on OpenVSP, a first vortex lattice calculation is made using OpenVSP's solver VSPAero, which includes corrections for highly swept and low AR wings. It also includes corrections for the leading-edge vortex lift and fuselage presence effects.

OpenVSP is also capable of estimating the parasite drag with a tool separated from the vortex lattice solver. This drag is estimated with the use of empirical formulas (such as DATCOM or six-series airfoils corrections) which are the same typically available in wing design books and papers, therefore, the prediction has the same fidelity as those ones. Since the prediction tool is external to the solver, the values of C_D and L/D are computed in a post-processing phase and the final results are finally obtained by merging the two outputs in MATLAB.

The sizing's target is to obtain the L/D value at the main design lift condition (to maximize the loiter condition) and aim to have the highest value without a substantial performance loss during every other design flight conditions. The sizing's results are found in Chapter 3.

For the first design iterations, symmetric NACA 64A airfoils have been considered (as suggested by Raymer [1]), afterwards subsequent modifications, using airfoils with a design C_L of 0.10 and 0.20, which means an increase in the camber, have been made to achieve good stall behavior and lift distribution. Other 6-series airfoils have initially not been considered since VLM methods are not capable of considering other airfoil characteristics besides the mean line camber and semiempirical C_{D_0} corrections. This also limits the possibility to analyze the more promising supercritical airfoils. The airfoil choice is not fixed nevertheless in this design stage since optimization is carried out in subsequent phases.

2.2. Wing Root-Fuselage Interaction

For a swept wing the root section is characterized by a particular flow behavior: the forward part of the chord has an increase in pressure, which is caused by the sudden change in the sweep angle [6]. This causes a change in the isobars on the wing: these would be parallel to the leading-edge sweep in an ideal case but tend to have a direction normal to the flow near the root, as it can be seen in Figure 6. This consequently leads to an increase in wave drag at the root, as the flow travels substantially normal to the isobars, which is especially crucial close to the drag divergence Mach. This can be mitigated through the application of isobar tailoring, meaning that the wing shape is tailored to match the real isobars as much as possible to the ideal ones.

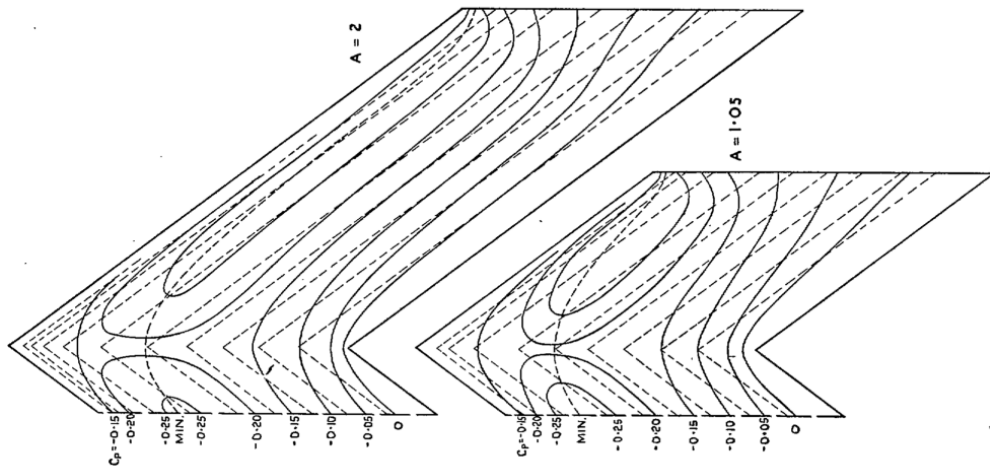


Figure 6 - Isobar effects on a swept wing [6].

This tailoring may be done in the following ways:

- Change the root to have an exaggerated sweep, thus having a global effect closer to the ideal case, as said by Raymer [1].
- Change the root airfoil to have a chordwise pressure distribution similar to the outboard section, as said by Sol in [7]. This is characterized by, in sequence:
 - a. Increasing the thickness of the forward part of the root section and decreasing the thickness of the rear part of the root section, to obtain similar chordwise upper-surface velocity distributions due to thickness along the span.
 - b. Increasing the t/c of the root section, to obtain identical chordwise upper-surface velocity distributions due to thickness along the span.
 - c. Decreasing the positive camber or applying negative camber on the root section, to adapt the pattern of the chordwise upper-surface velocity distribution due to lift to the one of the basic airfoil sections.
 - d. Increasing the incidence of the root section to obtain identical chordwise upper-surface velocity distributions along the span.

Since Leading Edge Extensions similar to the ones of the F-35 shown in Figure 7 have been added to the wing, the first solution is more compelling for the project, and is described with greater detail in Chapter 9.

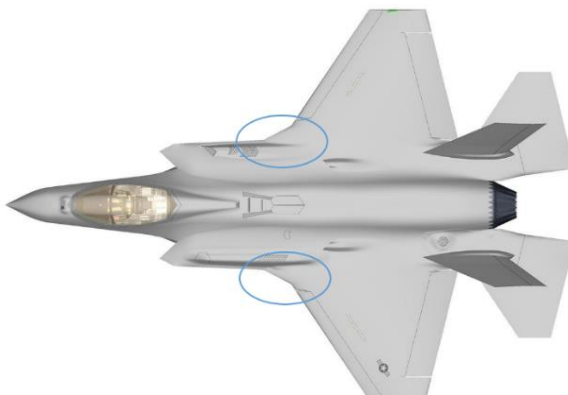


Figure 7 - F-35 Leading Edge Extensions [8].

Another consideration must be made to improve the wing-fuselage interaction. Typically, for a supersonic aircraft, in order to minimize the wave drag in transonic flight, the cross-sectional area of the fuselage is shaped following the Sears-Haack body [1]. Since this shape is impossible to obtain, supersonic aircraft are shaped follow the “supersonic area rule” as shown in Figure 8.

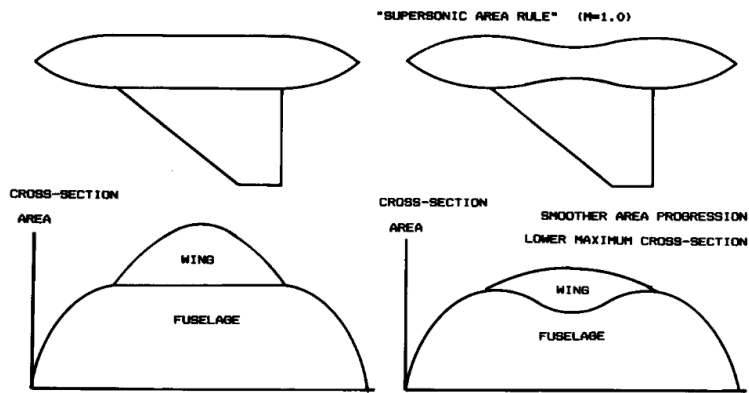


Figure 8 - Supersonic Area Rule [RAYMER].

While this approach is developed for supersonic aircraft, it is possible to apply it to a transonic aircraft like the STAD-1 since it is aimed at a reduction of the wave drag in transonic regions. This shaping pushes the airflow onto the wing reducing the tendency to separate and reducing shocks formation.

In Figure 9 it is possible to see how it is applied to the STAD-1 for a general wing configuration (in this case a lambda wing).

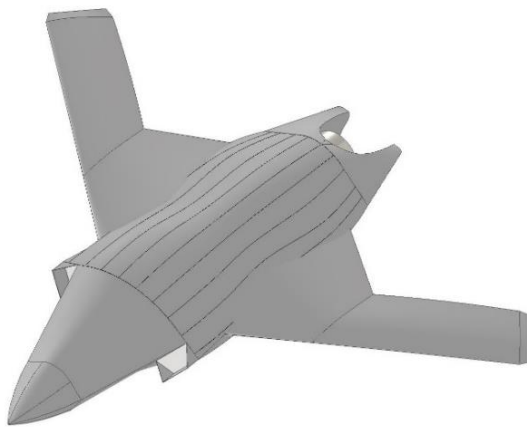


Figure 9 – Example of Supersonic Area Rule application on an early fuselage.

3. Wing Planform Design

A description of the wing planform design process and the results are provided in this chapter.

From the previous considerations, it has been possible to begin the wing planform design, with the main objective of a high L/D whilst still retaining a low RCS. For this reason, it has been designed by fixing the leading-edge sweep and trying to obtain the same sweep at the trailing edge in order to minimize the RCS. The first values chosen are $\Lambda_{LE} = 40^\circ$ and $\Lambda_{TE} = 35^\circ$. The wing twist has been chosen to try to get a spanwise sectional lift distribution which has the closest resemblance possible to an elliptical shape, while also having the wing tips' stall delayed with respect to the inner portions of the wing. This is to have the highest L/D possible while also avoiding the loss of controllability in roll when the wing is stalled. Satisfying both requirements also leads to the choice of higher curvature airfoils at the tip.

The designed wing is composed by two main sections with the following data:

	Root Section	Tip Section
<i>Leading edge sweep</i>	40°	40°
<i>Trailing edge sweep</i>	-35°	35°
<i>Section span</i>	2.58 m	2.70 m
<i>Root chord</i>	5.61 m	1.64 m
<i>Tip chord</i>	1.64 m	1.26 m
<i>Taper ratio</i>	0.292	0.771
<i>Twist</i>	0°	-4°

Table 5 - Lambda Wing Section Data.

While the global wing data are reported below:

Leading edge sweep	40°
Reference surface	26.56 m ²
Mean chord	2.65 m
Wingspan	10.56 m
Aspect ratio	4.198

Table 6 - Lambda Wing global geometric parameters.

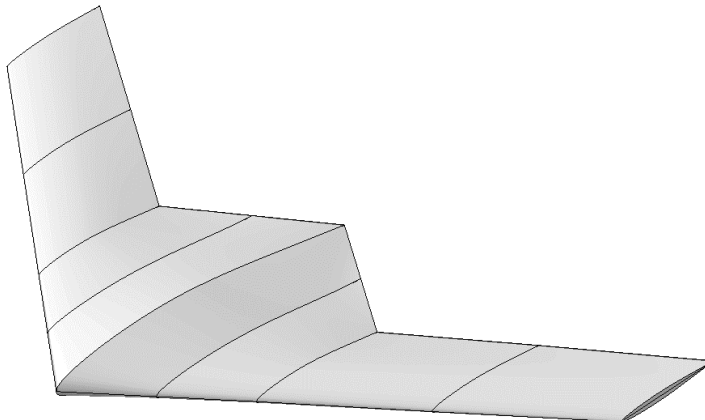


Figure 10 - Isolated Designed Lambda Wing OpenVSP geometry.

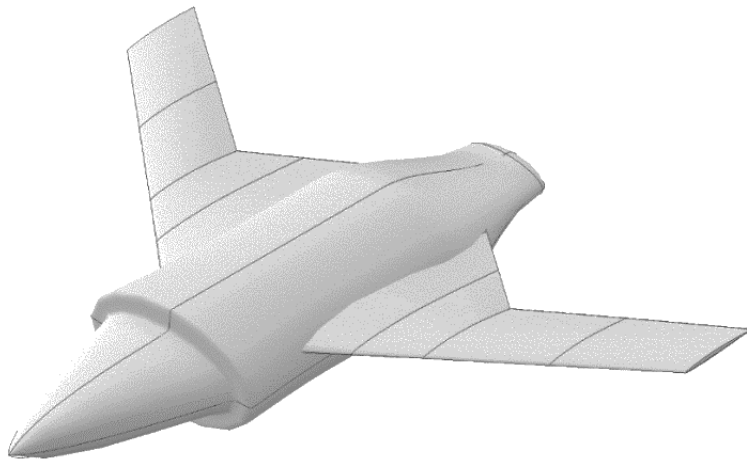


Figure 11 - Lambda Wing with simplified fuselage OpenVSP geometry.

The airfoils used for these analyses are reported in the table below:

Airfoil	Section position [m]	t/c	Design C_L	Chord [m]	Twist [°]
NACA 64A010	1.100	0.10	0.0	3.921	0.0
NACA 64A008	1.842	0.08	0.0	2.780	0.0
NACA 64A208	2.583	0.08	0.2	1.638	0.0
NACA 64A206	3.880	0.06	0.2	1.458	-2.0
NACA 64A206	5.280	0.06	0.2	1.264	-4.0

Table 7 - Airfoils selection for first lambda wing analyses.

3.1. Results

The analyses have been performed in OpenVSP by first checking the results of the Parasite Drag tool, which returned the contribution of the OpenVSP C_{D_0} and the Reynolds numbers of the wing and the fuselage. Using the computed Reynolds numbers, it has been possible to set the VSPAero analyses. Afterwards the results have been postprocessed in MATLAB by adding the C_{D_0} from the parasite tool to the computed induced drag C_{D_i} and then plotted.

The OpenVSP C_{D_0} consists in the sum of the parasite drag and the viscous drag. The parasite drag is computed by using semi-empirical viscous and parasite drag corrections. This consists of the Component-Buildup Method described in Raymer and used in OpenVSP; in this model the drag coefficient is computed by the following equation:

$$C_{D_0} = \sum_c \frac{C_{f_c} FF_c Q_c S_{wet_c}}{S_{ref}} \quad (3.1)$$

Where S_{wet_c} is the component's wet surface (automatically computed in OpenVSP), C_{f_c} is the component's skin friction coefficient internally computed by the Parasite Drag tool, FF_c and Q_c are the component's Form Factor and Interference Drag parameters. The appropriate NACA six-series model has been used for the FF of the wing, while the Hoerner Streamlined Body model has been used for the fuselage. As suggested by Raymer [1] the Q factor has been set to 1 since the fuselage has negligible interference in most of the cases. The computed C_{D_0} are reported in the Table 8 for an altitude of 15,000 ft.

C_{D_0} at $M_a = 0.50$	Re at $M_a = 0.50$	C_{D_0} at $M_a = 0.85$	Re at $M_a = 0.85$
0.00866	$2.45 \cdot 10^7$	0.00820	$4.8 \cdot 10^7$

Table 8 - Parasite Drag tool results.

The resulting wings have been compared in the design conditions at $M_a = 0.50$ and 0.85 . The results are shown in the plots in Figure 12. Here the lift to drag ratio, the pitch moment coefficient and the lift coefficient are reported in function of the angle of attack; a polar of the wing is also reported in the bottom left plot.

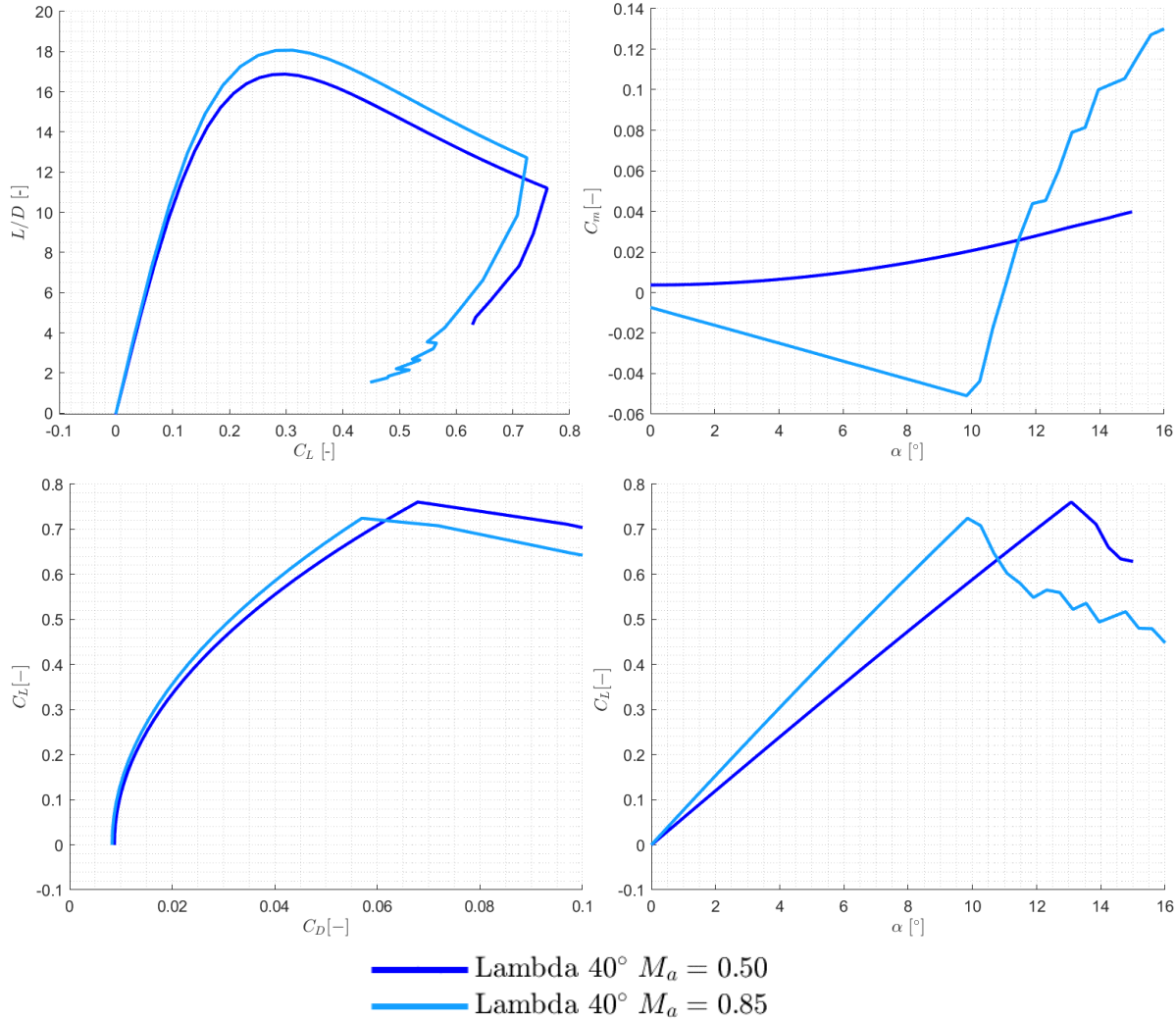


Figure 12 – Planform sizing results with legend.

From the results it is possible to notice that at $M_a = 0.50$ a $(L/D)_{\max} = 16.88$ is obtained, which is satisfactory.

The stall is evaluated in OpenVSP with the inbuilt Carlson Pressure Correlation [9]. The correlation detects a stall angle around 13° at $M_a = 0.50$. Instead at $M_a = 0.85$, the stall angle is detected at lower values of the angle of attack, but, since transonic effects take in place, this is less likely to be a good correlation.

3.2. Spanwise Distribution

As previously said, the wing twist and airfoil selection is strongly influenced by the target spanwise lift distribution, which must be as close as possible to an elliptical distribution and must have a delayed wing tip stall. This has been satisfied for the designed planform as shown in Figure 13, where c_s is the sectional chord, c is the mean aerodynamic chord, and C_l is the sectional lift coefficient. It can be further seen how the stall propagates from the inner wing sections to the tip even at higher angles.

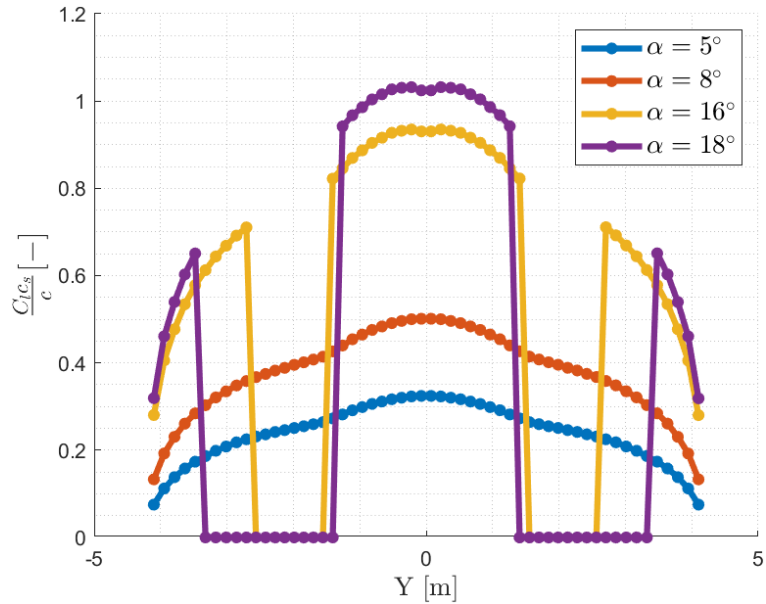


Figure 13 – Spanwise lift distribution at $M_a = 0.85$

3.3. Sweep Sensitivity Analysis

A sensitivity analysis on the sweep angle is carried out in order to obtain the best solution in terms of L/D , $C_{m\alpha}$ and C_{Lmax} and it is reported in Figure 14.

Since the sweep angle greatly influence the entire planform design, the compared configurations have different airfoil thickness ratio, fixed by the results of the Korn equation (7.1), different Λ_{TE} , wingspan (b), mean chord (\bar{c}) and most importantly different AR .

$\Lambda_{LE} [^\circ]$	$S_{ref}[m^2]$	AR	$Twist [^\circ]$	$b [m]$	$\bar{c} [m]$	$Airfoil^t/c$	$\Lambda_{TE} [^\circ]$
35	26.30	4.368	-2	10.71	2.81	6%	± 35
40	26.56	4.198	-4	10.56	2.65	8%	± 35
45	26.21	3.839	-4	10.03	2.76	10%	± 45
50	28.47	3.802	-4	10.40	2.95	10%	± 45

Table 9 - Sensitivity analysis data.

Higher Λ_{LE} have not been considered since they result in geometrically or structurally unfeasible geometries.

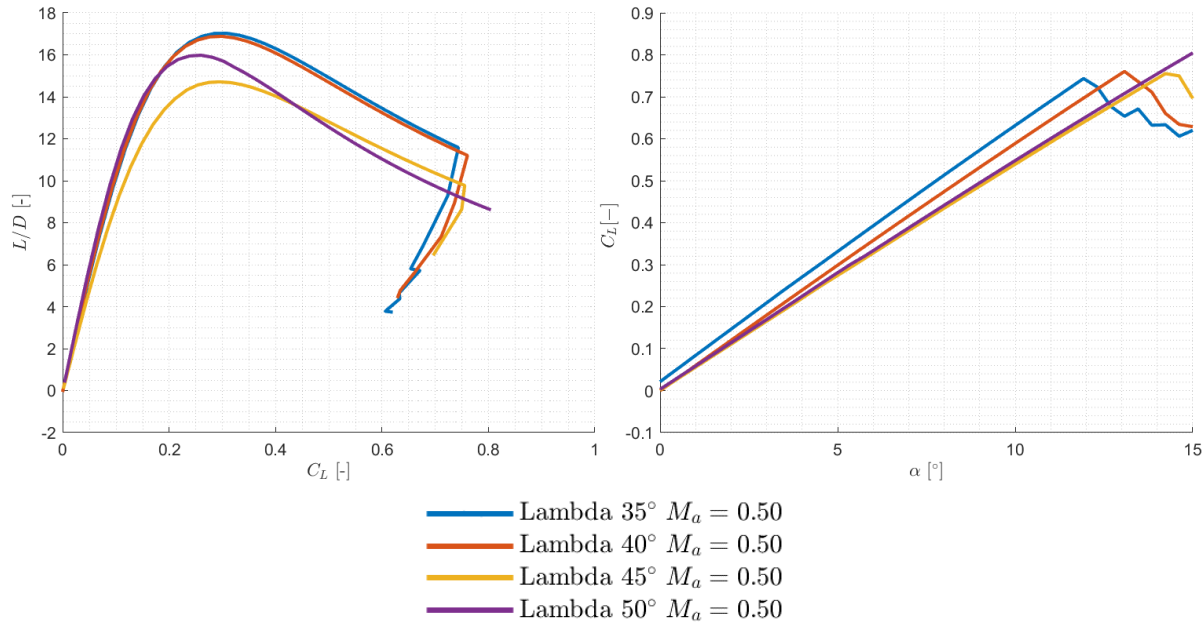


Figure 14 - Sweep sensitivity results for configuration with legend.

From the sensitivity analysis it is evident that the optimum configuration in terms of L/D are Λ_{LE} equal to 35° and 40° . Since the results are quite similar for both angles, the configuration with $\Lambda_{LE} = 40^\circ$ was chosen since it stalls at a higher angle of attack.

4. Tail Volume Sizing

A process of the sizing of the V-tail is here presented, with updated aircraft results with the addition of the tail.

The approach taken to size the tail of the aircraft is here presented. The process to evaluate the tail volume has been partially modified from the classical one proposed by Raymer [1] since a V-tail is preferred due to RCS reasons. The same reasons also lead to a request on the dihedral angle of the tail (γ), which is set equal to 60 degrees from horizontal plane.

Thus, with a set angle, the idea is to obtain the vertical and horizontal plane surfaces through the tail volume coefficients (c_V^t and c_H^t), Equation (4.1) and Equation (4.2) provided by Raymer [1], which are derived from statistical data, and define them as the projection of the V-tail on the vertical and horizontal plane, multiplied by two (as there are two tail parts). The vertical surface is used as sizing target rather than the horizontal one as the objective is to satisfy the yaw control; the pitch control instead will be mainly affected by the use of elevons and slats. For fighters, the vertical tail volume coefficient is equal to 0.08 while the horizontal tail volume coefficient is equal to 0.40 [1].

$$S_V^t = \frac{c_V^t S_{Ref} b_{wing}}{L_V^t} \quad (4.1)$$

$$S_H^t = \frac{c_H^t S_{Ref} \bar{C}}{L_H^t} \quad (4.2)$$

The tail's arms, as defined in Figure 15, have been iteratively fixed since they greatly affect the tail span and position and so the aircraft length and height. Since a V-tail has been used, the arms of the vertical and horizontal tails are equal, meaning $L_V^t = L_H^t$.

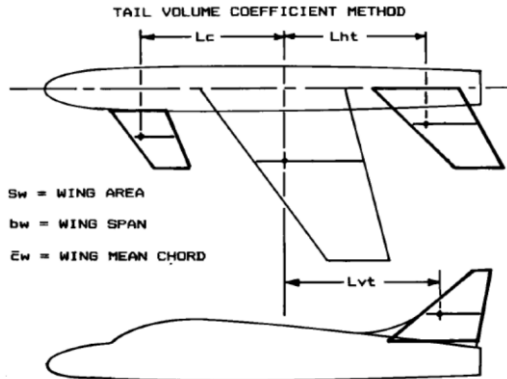


Figure 15 - Tail volume coefficients geometry definitions.

As previously said, only the vertical part has been considered for the sizing of the actual surface through Equation (4.3). This allows to greatly reduce the final tail size but with an undersized equivalent horizontal surface. The equivalent horizontal tail surface has then been computed from Equation (4.4).

$$S^t = \frac{S_V^t}{\sin(\gamma)} \quad (4.3)$$

$$S_H^t = \frac{S_V^t}{\tan(\gamma)} \quad (4.4)$$

To set the distance between the aerodynamic center of the wing and the one of the tails, the wing must be longitudinally positioned again. The wing is placed so that the center of gravity is at about

40% of the MAC of the wing, as suggested by Raymer [1]. This leads to a nose to LE distance of 3.6 m (from the beginning of the wing considering the extension inside the fuselage). Afterwards, the tail position is set from its longitudinal mean quarter chord.

It is possible to compute the longitudinal tail mean chord position \bar{x}^t and the wing mean chord position \bar{x}^w by following equation:

$$\bar{x}^t = \frac{b^i (1 + 2\lambda_{Tail})}{6 (1 + \lambda_{Tail})} \tan (\Lambda^i) \quad (4.5)$$

Once the wing position and the tail arm are fixed, it is possible to compute the tail position. Doing this requires fixing the tail aspect ratio λ_{Tail} first. From Raymer [1] suggestion a taper of 0.4 has been considered.

The resulting surfaces are given by:

Vertical Surface (from Tail Volume Method)	5.61 m ²
Horizontal Surface (from Tail Volume Method)	7.04 m ²
Actual Tail Surface	6.48 m ²
Equivalent Vertical Surface	5.61 m ²
Equivalent Horizontal Surface	3.24 m ²

Table 10 – Resulting Tail volume method parameters.

Once the area is known, the planform has been defined. Using a trapezoidal planform (ideal for low observability) would require an incredibly high root chord, so a swept planform is preferred. The leading-edge sweep is fixed from RCS requirements to 40°. Lastly, to define the root chord and the span, a compromise between both dimensions must be reached. This is done by trying to obtain a vertical projected span smaller than the height of the fuselage. To fine tune the parameters, a MATLAB script has been used iteratively which allows to compute the tail's span b^t with Equation (4.6) after fixing the tail root chord c_{Root}^t .

$$b^t = \frac{S^t}{(1 + \lambda)c_{Root}^t} \quad (4.6)$$

This finally leads to the results presented in Table 11:

Longitudinal Position [m]	8.93
Tail Surface [m²]	6.48
Mean Chord [m]	1.68
Root Chord [m]	2.40
Taper Ratio	0.4
Leading Edge Sweep [°]	40
Dihedral Angle [°]	60
Span [m]	1.93
Height [m]	1.67

Table 11 - Tail Geometry Data.

These modifications on the fuselage have been implemented in the simplified OpenVSP model, where it is has been possible to compute the new aerodynamic results as described in paragraph 4.1.

The tail has been placed slightly higher than the wing, at one meter between them in order to avoid the influence of the fuselage and wing vortices and to avoid having most of the V-tail's aerodynamic surface covered by the wing's wake at medium angles of attack (around 10°).

Afterwards, the choice of the tail's airfoil has been made by finding the best compromise between trim performance and drag minimization. Only symmetrical airfoils have been considered since they are preferable for a ruddervator or, more in general, a vertical tail. It is then necessary to impose a small enough t/c in order to avoid having shockwaves on the tail. By following the advice of [10] the same thickness ratio of the trapezoidal part of the wing (8%) has been selected. The first airfoil chosen has been the NACA 0008. After some trials, on some NACA 4 and 6 series airfoils, the NACA 65A008 have been selected in order to minimize trim drag and C_{D_0} .

After some higher order analyses, shown in section 8.2, it was necessary to select a thinner airfoil in order to avoid shockwaves on the tail. For such reason the final airfoil chosen for the tail is the NACA 65A006.

4.1. Results

After fixing the tail and wing geometry, the new aircraft configuration has been modelled in OpenVSP. The fuselage has been stretched to accommodate the V-tail and has been further modified to improve internal components placing. These modifications require changing the fuselage model in OpenVSP as shown in Figure 16 with also the V-tail included.

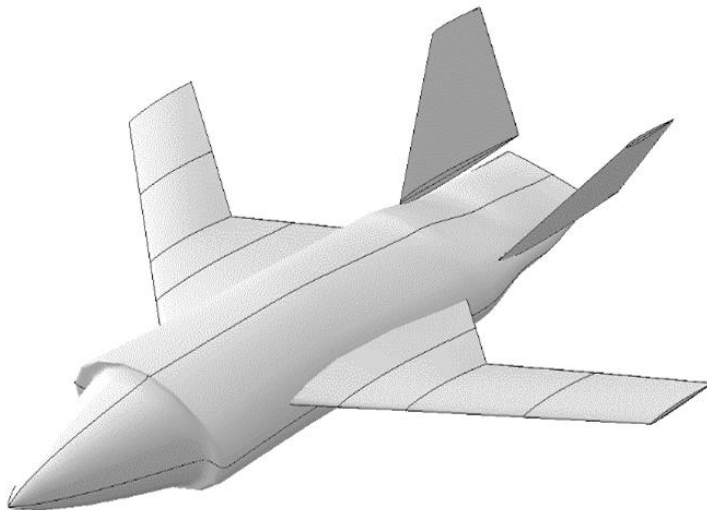


Figure 16 - OpenVSP complete V-tail model.

Once again, the C_{D_0} has been computed by using the Parasite Drag Tool and summed with the C_{D_i} . Here the same settings of the model without tail have been used for the wing and fuselage; for the V-tail, instead, an Interference Factor of 1.08 and the NACA 6 series Form Factor estimation have been used as suggested by Raymer [1].

The results have been reported in the following table:

Altitude [ft]	C_{D_0} at $M_a = 0.50$	Re at $M_a = 0.50$	C_{D_0} at $M_a = 0.85$	Re at $M_a = 0.85$
0	0.01081	$3.80 \cdot 10^7$	0.01002	$6.40 \cdot 10^7$
10,000	0.01126	$2.85 \cdot 10^7$	0.01043	$4.80 \cdot 10^7$
15,000	0.01112	$2.45 \cdot 10^7$	0.01064	$4.20 \cdot 10^7$
30,000	0.01236	$1.51 \cdot 10^7$	0.01143	$2.58 \cdot 10^7$

Table 12 - V-tail model drag coefficients.

As expected, the presence of the V-tail and a longer fuselage noticeably increase the drag coefficients of the aircraft. The presence of the tail severely worsens the L/D but it is mandatory for trim considerations.

The results computed in OpenVSP are reported in the plot in Figure 17. Here the moment coefficient has been computed considering a reference position of 5.9 m from the nose of the aircraft. This reference point has been selected close to the resulting nominal CG position.

In the plot in Figure 17 the results in term of L/D , C_m , C_L and the polar plot are reported. This configuration results in a $(L/D)_{MAX} = 14.80$ for the loiter phase at $M_a = 0.50$, while it results in a $(L/D)_{Turn} = 15.50$ in the sustained turn conditions at $M_a = 0.85$.

The stall correlation also detects a stall angle of attack of around 12.5° at $M_a = 0.50$ which is slightly before the model without the V-tail but the C_{LMAX} has similar values. Instead, the clean stall angle results in $\alpha_{Stall}^{Clean} = 14.0^\circ$ related to the flying condition at $M_a = 0.20$.

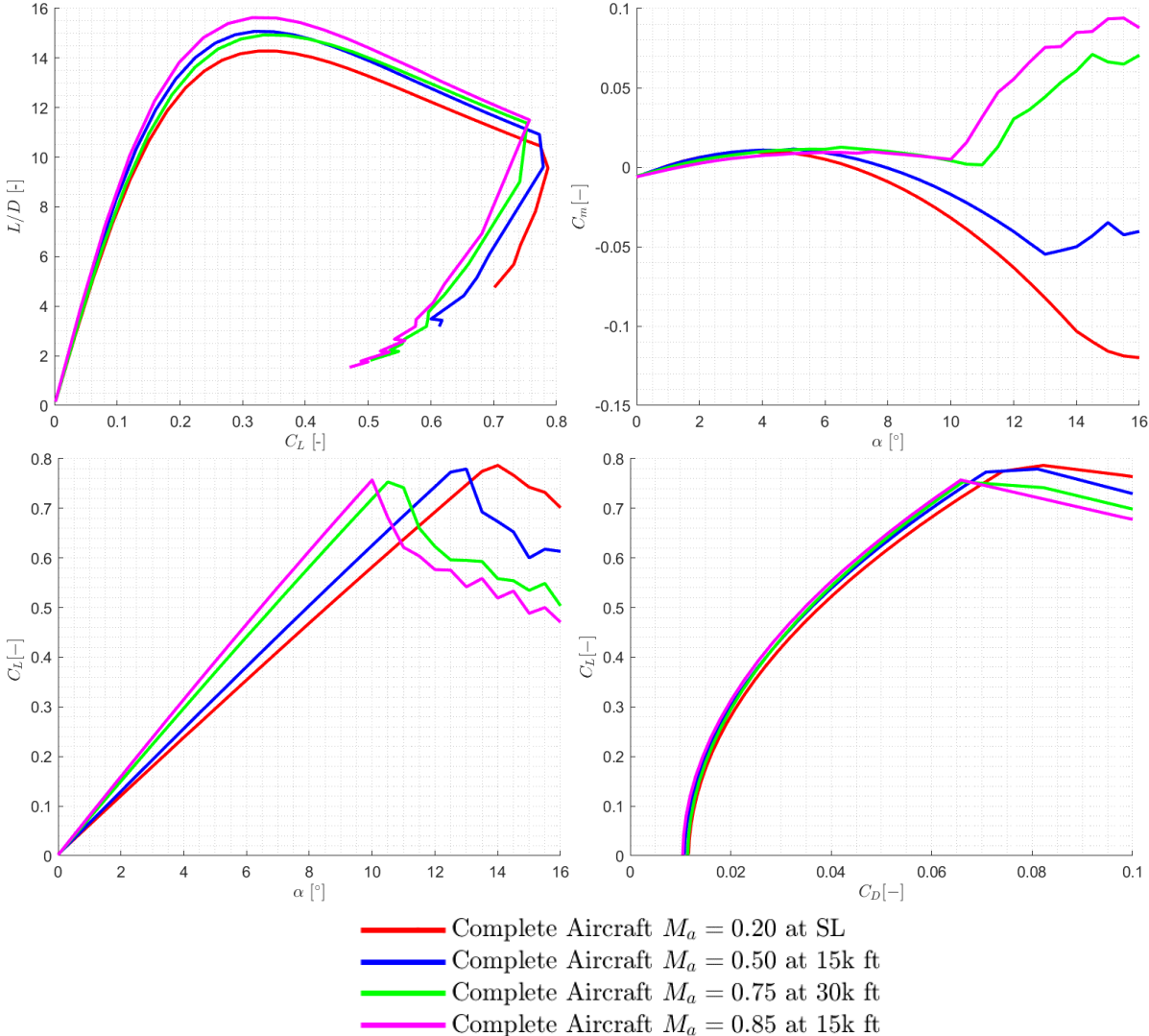


Figure 17 – V-tail aerodynamic results with legend.

Afterwards, from the consideration made in Chapter 7 and Chapter 8, the airfoil of the wing and the tail have been changed. This configuration, composed by NACA 65 airfoils, will be considered the final one used for computing the polars shown in Figure 18, the stability derivatives and the control and high-lift surfaces shown in the following paragraphs. Nevertheless, it is not the final configuration, as will be shown in Chapter 10. An aerodynamic optimization will be performed in order to further improve the wing performance in transonic conditions. Since the results of this process resulted in custom airfoils for which OpenVSP or other VLM can't distinguish between the pre-optimization and post-optimization configurations, it is not possible to compute its polar without

Tail Volume Sizing

using higher fidelity method. This verification will be left for successive design phases and won't be included in this report.

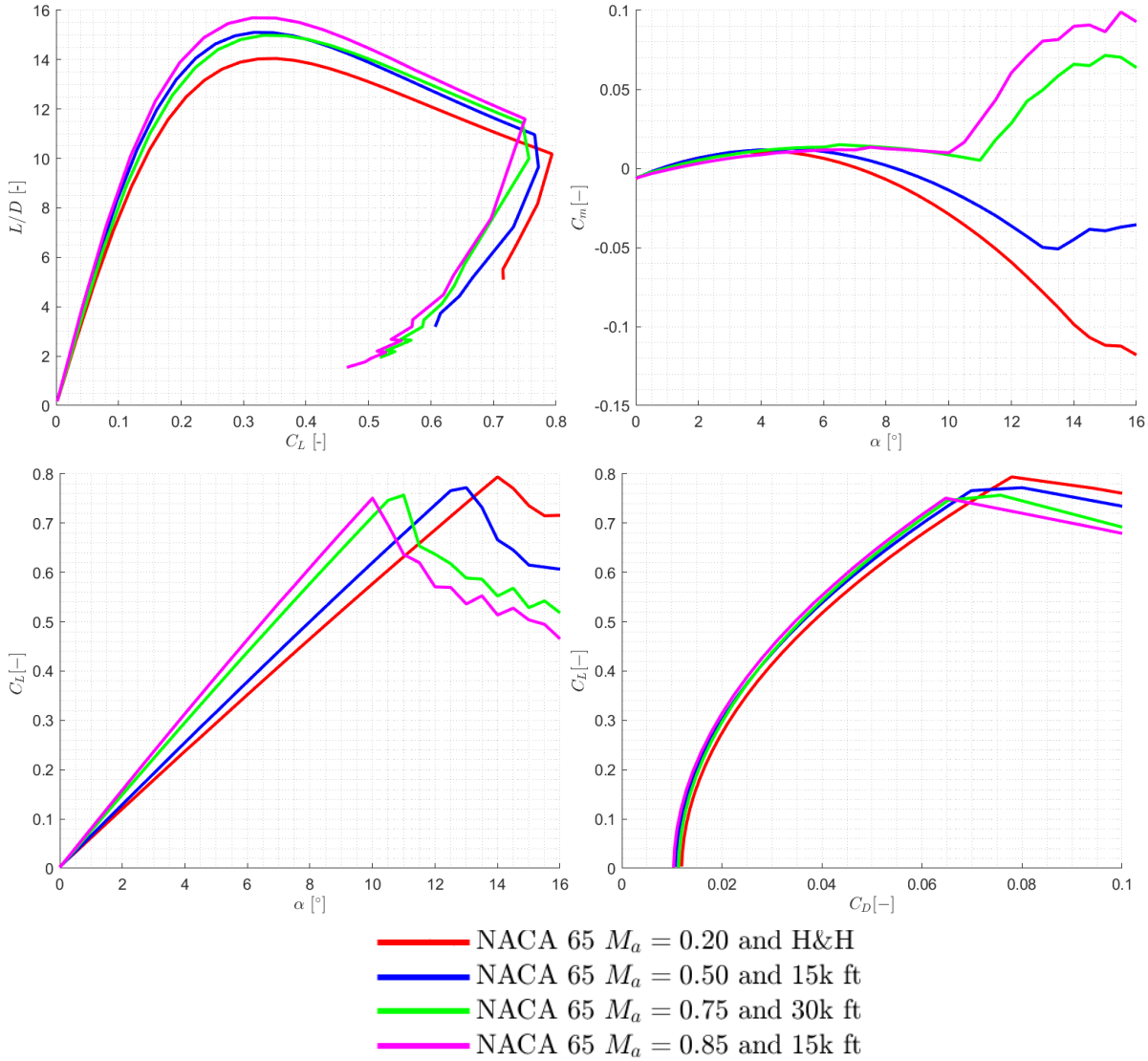


Figure 18 – NACA 65 configuration results.

5. High-Lift and Control Surfaces

The sizing of control surfaces that act as high-lift devices is presented, as well as flapped aerodynamic polars with the addition of landing gear drag.

To satisfy the requirement regarding the stall speed (and so on the $C_{L_{max}}$ in landing and take-off configurations, equal to 1.25 as said in Chapter 1) it is necessary to employ high-lift surfaces.

The first considered high-lift surfaces are placed in the inboard wing section and spans for all its length. These surfaces act primarily as landing and take-off flaps but can be also used for helping the pitch control. In this way it is possible to satisfy trim and pitch rate requests while compensating for the undersized tail for longitudinal control, as explained in Chapter 4.

In the outboard wing sections two ailerons that span all along the swept portion of the wing are placed. These surfaces can also act as high-lift surfaces, making them effectively flaperons. This allows to increase the maximum lift while avoiding adding another high-lift surface, and they can also help with aircraft trim when they are deflected symmetrically. Unfortunately, they also have cons: in order to obtain enough roll authority in landing conditions the surfaces have their deflections limited and so they provide less lift increment compared to standard flaps. Furthermore, since they operate at low speed and high angle of attack, using them as flaperons might anticipate aileron stall. Another disadvantage is that flaperons introduce adverse yaw, since for roll control one aileron needs to be deflected more than the other one, thus creating a force asymmetry causing a yaw moment. Even considering these disadvantages, the use of ailerons as high lift devices has been taken since it is not possible to place more trailing edge high-lift surfaces.

The last considered high-lift surfaces are two leading-edge high-lift surfaces, placed along all the span of the wing. These surfaces have been considered in order to increase maneuverability during high AOA maneuvers and to further increase the maximum lift coefficient on landing and take-off configurations.

Finally, on the V-tail, a couple of ruddervators have been included for yaw and pitch control and are presented in Appendix A.2.

5.1. High-Lift Design

The most common trailing-edge flaps for fighters are plain flaps and slotted flaps. Leading-edge flaps and slats are also commonly used in these kinds of aircraft. For low-observability reasons, it is necessary to avoid introducing gaps in the structure, thus excluding slotted flaps and slats. Furthermore, since they need to also act as a control surface, plain flaps are preferred since they allow sufficient upward deflection.

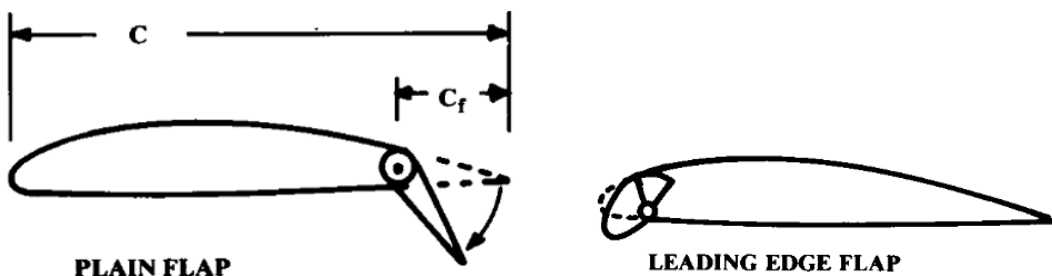


Figure 19 - Flaps considered topologies [1].

The analysis of these devices has been done, at first, considering typical sectional lift increment values and afterwards using semi-empirical methods derived from DATCOM. The values and the methods are present in [1].

5.1.1. High-Lift First Sizing

The maximum lift coefficient obtainable is defined in equation (5.1), where $C_{L_{Max}} = 0.78$ of the clean configuration has been obtained by the analysis on OpenVSP in paragraph 4.1. As previously said in Chapter 1, the objective is $C_{L_{Max}}^{Flap} = 1.25$, this requires a $\Delta C_{L_{Max}} \geq 0.47$.

$$C_{L_{Max}}^{Flap} = C_{L_{Max}} + \Delta C_{L_{Max}} \quad (5.1)$$

The lift increments have been computed separately for the leading-edge flaps (ΔC_L^{LE}), the elevons ($\Delta C_L^{elevons}$), and the ailerons ($\Delta C_L^{ailerons}$) and then summed to obtain the maximum lift coefficient increment ($\Delta C_{L_{Max}}$) by taking into account the portion of the flap surfaces ($S_{flapped}$) and the hinge line sweep (Λ_{Hinge}). The flapped surfaces are defined as explained in [1] and depicted in Figure 21. The airfoil's maximum lift increment is taken from the following table:

High-lift device	$\Delta C_{L_{max}}$
Flaps	
Plain and split	0.9
Slotted	1.3
Fowler	1.3 c'/c
Double slotted	1.6 c'/c
Triple slotted	1.9 c'/c
Leading edge devices	
Fixed slot	0.2
Leading edge flap	0.3
Kruger flap	0.3
Slat	0.4 c'/c

Figure 20 - Typical airfoil maximum lift increment for different devices.

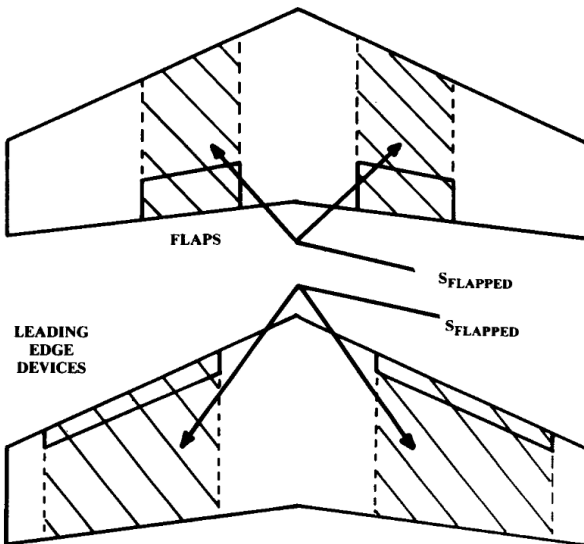


Figure 21 – Reference and Flap Surfaces Definition [1].

It is worth noting that this method is suitable only for a planform sizing of the high-lift surface since it doesn't take into account the surfaces' deflection.

In Table 13 the geometric parameters of the flaps used for the first design iteration are reported. The hinge sweep Λ_{Hinge} has been chosen by following the planform alignment method in order

to reduce the aircraft's RCS. The hinge line is forced to be parallel to the leading edge or trailing edge and the flaps chord are forced to be parallel to the local wing sectional chords. This choice spans from the planform alignment method for RCS reduction. In the following figure it is possible to see the sized flap configuration:

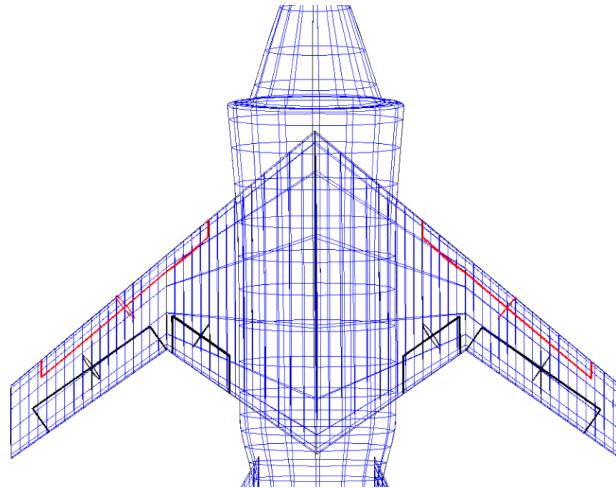


Figure 22 - High-lift surface OpenVSP visualization.

	$S_{flapped}$ [m ²]	Chord [m]	Span [m]	Λ_{Hinge} [°]
$S_{Elevons}$	5.00	0.66	1.96	-35
$S_{Ailerons}$	6.09	0.50	4.06	35
$S_{LE flaps}$	11.80	0.30	5.81	40

Table 13 - Control surfaces sections data.

Equation (5.2) accounts for the variations of the single wing section. To compute the total variation with respect of the wing all the contributes are summed considering their flapped surface S_{flap_i} and multiplied by the local sweep angle Λ_i^{local} :

$$\Delta C_{L_{max}} = 0.9 \sum_i \Delta C_{L_{max,i}} \frac{S_{flapped,i}}{S} \cos(\Lambda_{Hinge}) \quad (5.2)$$

The following results are thus obtained:

ΔC_L^{LE}	$\Delta C_L^{Elevons}$	$\Delta C_L^{Ailerons}$	ΔC_L^{LEX}	$\Delta C_{L_{Max}}$
0.13	0.12	0.61	0.32	0.73

Table 14 - Lift variations with high-lift devices.

5.1.2. Second Sizing Iteration

Proceeding with the design, a more accurate method has been used to verify the lift increments of the high-lift surfaces and to fix their maximum deflection. For the trailing edge high lift surfaces (elevons and ailerons) Equation (5.3) has been used to compute the lift coefficient variation with respect to the surface deflection $\delta_{TE} \left(\frac{\partial C_L}{\partial \delta_f} \right)_{TE}$, where $\left(\frac{\partial C_L}{\partial \delta_f} \right)_{TE}$ is obtained from Figure 23 and K_f from Figure 24.

$$\left(\frac{\partial C_L}{\partial \delta_f} \right)_{TE} = 0.9 K_f \left(\frac{\partial C_l}{\partial \delta_f} \right)_{TE} \frac{S_{flapped}}{S_{ref}} \cos(\Lambda_{Hinge}^{local}) \quad (5.3)$$

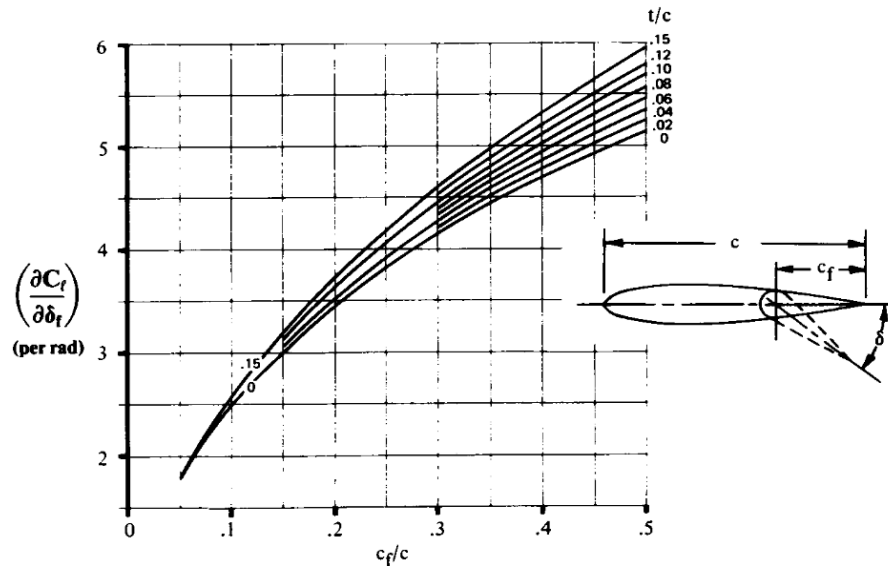


Figure 23 - Theoretical airfoil lift increment for plain flaps [1].

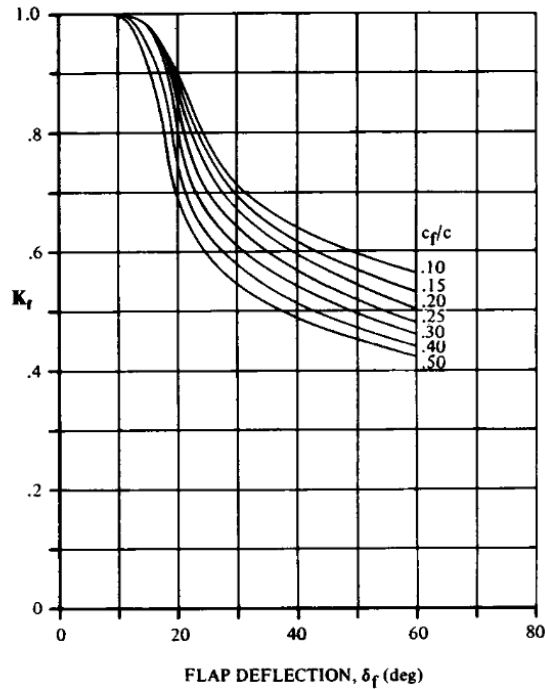


Figure 24 - Empirical correction for plain flap lift increment [1].

It is then possible to obtain the lift increment by multiplying by the surfaces' deflection angle. For the elevons a deflection of 50° has been considered by referring to typical cases shown in [10], while for the ailerons a maximum deflection of 50° has been considered as well. But in order to retain enough roll authority during landing and take-off the high-lift deflection has been conservatively limited to 15°. These values are used for the landing configuration. For the takeoff configuration the elevons are set to 30° and the ailerons to 0°.

For the sizing of leading edge flaps a similar procedure taken from [11] has been followed.

$\left(\frac{\partial C_L}{\partial \delta_f}\right)_{LE}$ is computed from Equation (5.4) using (5.5) and (5.6).

$$\left(\frac{\partial C_L}{\partial \delta_f} \right)_{LE} = \left(\frac{\partial C_l}{\partial \delta_f} \right)_{LE} \frac{S_{flapped}}{S_{ref}} K_A \quad (5.4)$$

Where:

$$\left(\frac{\partial C_l}{\partial \delta_f} \right)_{LE} = 0.9 \eta_{MAX} \eta_\delta \quad (5.5)$$

$$K_A = (1 - 0.08 \cos^2 \Lambda_{Hinge}) \cos^{3/4} \Lambda_{Hinge} \quad (5.6)$$

By multiplying by the leading edge's flap maximum deflection, it is possible to obtain the maximum lift increment. The maximum deflection has been set to 25° , which is 5° higher than typical commercial aircraft since fighters typically deflect the leading edge surfaces at higher angles. This configuration is used for both landing and take-off after the ground-roll. During the ground-roll, instead, the deflection is set to 0° .

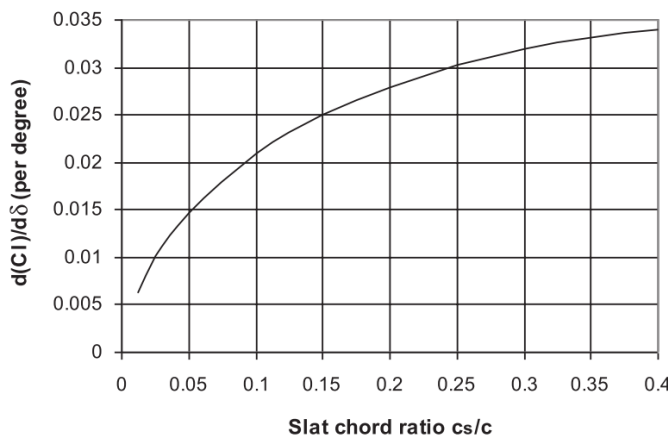


Figure 25 -Rate of change of airfoil lift coefficient with leading edge flap deflection [11].

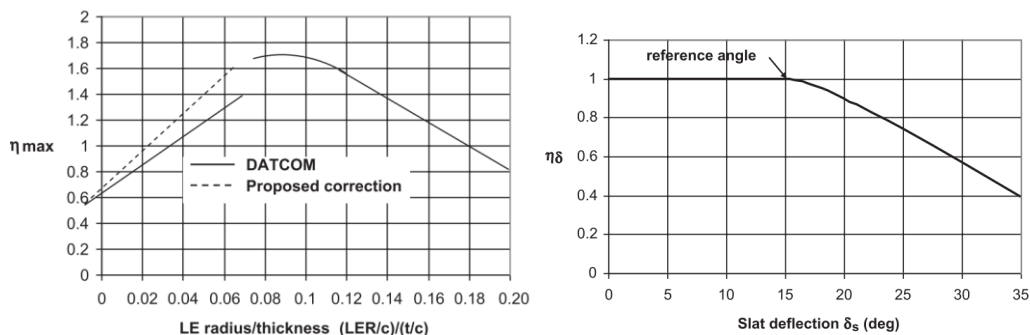


Figure 26 - Correction factor plots for leading edge flap [11].

The results are shown in the following table:

	ΔC_L^{LE}	$\Delta C_L^{Elevons}$	$\Delta C_L^{Ailerons}$	ΔC_{LMax}	C_{LMax}
Landing	0.18	0.25	0.16	0.59	1.37
Take-Off	0.18	0.15	0.00	0.33	1.11
Ground-Roll	0.00	0.15	0.00	0.15	0.93

Table 15 - High-lift surfaces lift increments.

The results satisfy the C_{LMax} requirement even without accounting the presence of the LEX, but these methods are expected to overestimate the real value of C_{LMax} , as it is expected that the

real value will be minor than the sum of each separate components due to mutual interaction. Even including the LEX effects, it is expected that the $C_{L_{Max}}$ of both the leading-edge flaps and the elevons will be reduced while globally it should increase. Lastly the stall predicted by OpenVSP is likely to be an overestimation of the real $C_{L_{Max}}^{Clean}$. For these reasons it is crucial to retain enough margin to overcome problems that might arise from successive design phases. Eventually the high-lift surfaces could be downsized if not necessary at the end of the full design process.

It is also necessary to evaluate the C_D contribution given by the high-lift surfaces. As explained in [1], the high-lift surfaces cause an increase in C_{D_0} and in C_{D_i} that can be computed by some semi-empirical corrections, but the correction on the C_D variation is used more often. The correction used are taken from [10] and are shown in Equation (7.2) where $\frac{c_f}{c}$ is the average chord ratio between the flap and the wing section and δ_{Flap} the flap deflection. Parameters δ_1 and δ_2 are taken from the plots in Figure 27, considering the correction for plain flaps.

$$\Delta C_D = \Delta_1 \left(\frac{c_f}{c} \right) \Delta_2 (\delta_{Flap}) \frac{S_{flap}}{S_{Ref}} \quad (5.7)$$

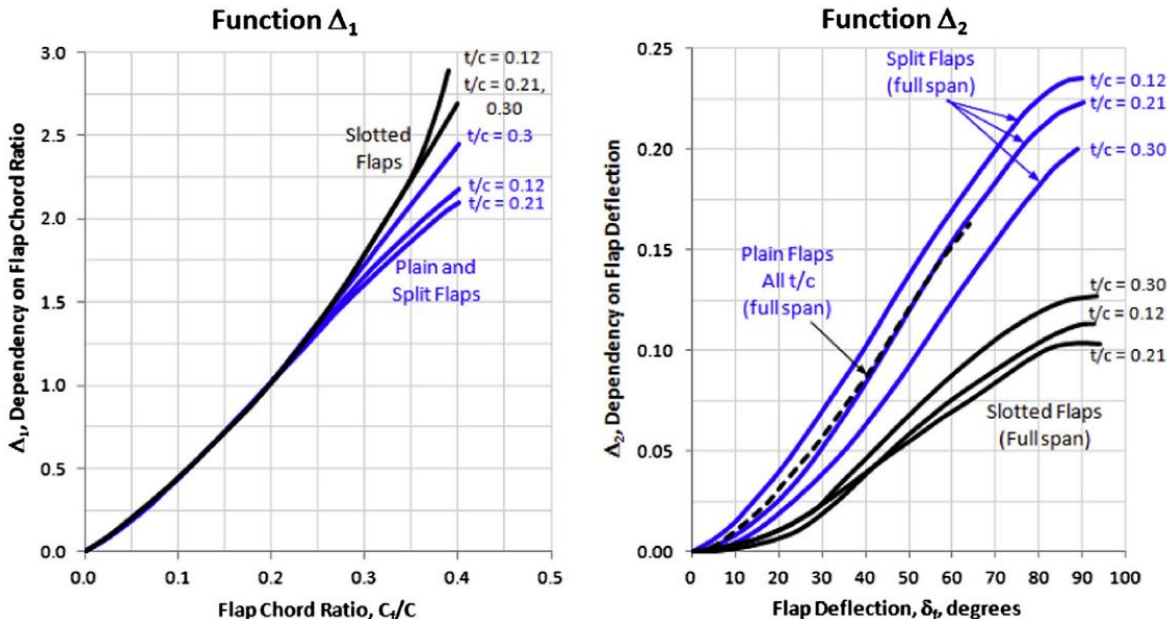


Figure 27 - Estimation of the drag contribution coefficients [10].

This approach is valid for both the elevons and the ailerons, while for the leading edge flaps it is possible to neglect its drag increase at this design stage, since, as shown in Figure 28 (D-nose curve), their effect are very small. Furthermore, computational methods are necessary to correctly evaluate the variation, but this is outside the scope of the preliminary design. A recap of the drag contributions is presented in Table 16.

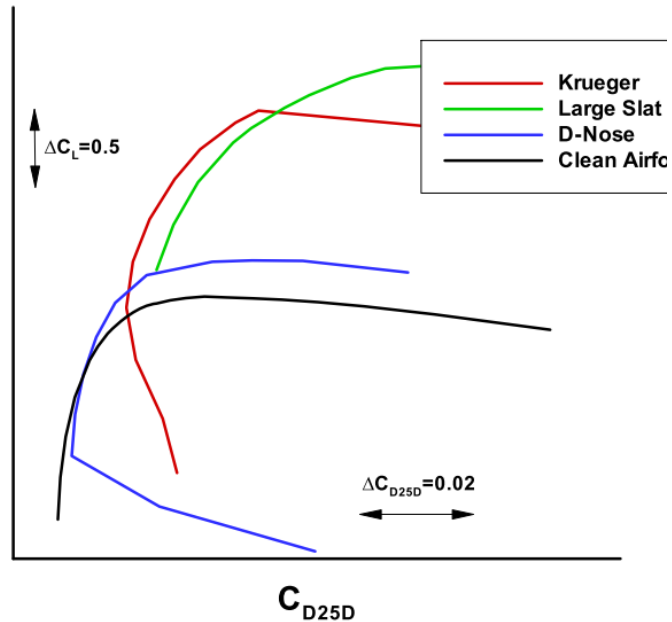


Figure 28 - Leading edge high-lift surfaces polar [12].

	ΔC_D^{LE}	$\Delta C_D^{Elevons}$	$\Delta C_D^{Ailerons}$	ΔC_D^{Flap}	ΔC_D^{Gear}
Landing	0.0000	0.0352	0.0084	0.0436	0.019
Take-Off	0.0000	0.0168	0.0000	0.0168	0.019
Ground-Roll	0.0000	0.0168	0.0000	0.0168	0.019

Table 16 - High-lift surfaces drag increments.

5.2. Flapped Polars

Finally, it is possible to compute the polar in the landing and take-off configurations by adding the C_L and C_D corrections to the polar at $M_a = 0.20$ computed in paragraph 4.1. This is shown in the plot below:

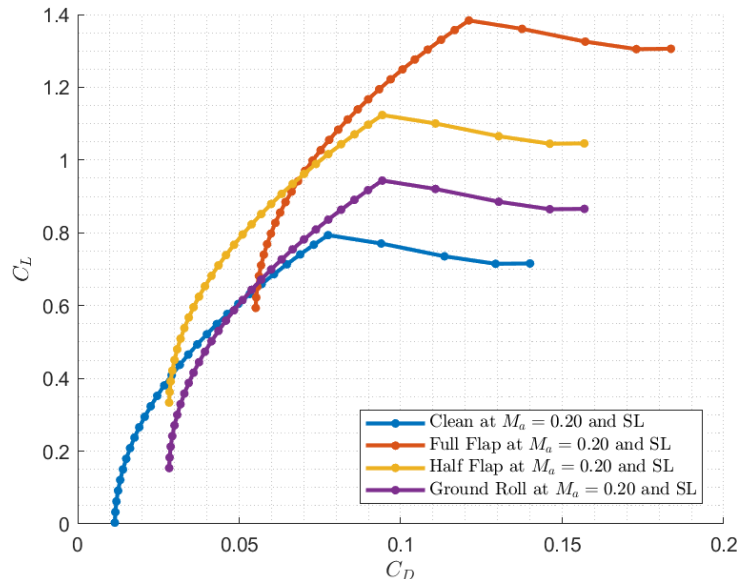


Figure 29 – Polars of different configurations at sea level (without landing gear drag).

6. Higher Order Methods Setup

An introduction on one of the higher order methods used in the following design and optimization process is presented here, as well as preliminary considerations.

Since the problem is noticeably complex, it is necessary to perform higher order CFD analyses starting from the preliminary design as many tridimensional and transonic effects are not possible to be evaluated with lower order methods. Main examples of these are strong interaction-based surfaces like the LEX, and shockwaves at higher M_a that influence the airfoil choice. CFD in preliminary and even conceptual design are always more frequently used in industries for a main reason: it is necessary to build enough sensitivity on the aerodynamics from the beginning of the project in order to better evaluate every consequence of the choices made in those phases. It is fundamental to say that the objectives of these analyses are not to find the right values of the aerodynamic coefficients or to totally redesign the wing, but the objective is to evaluate the effects that lower order methods cannot consider, mainly shockwaves and airfoil shape effects.

Lastly, those simulations, even if more demanding from a computational point of view with respect to VLM, can still give meaningful results in a relatively short time. Although results might not be extremely precise, they allow to obtain a rough result of the coefficients and of the flow behavior.

In this chapter, the software used for these analyses and the numerical consideration are proposed.

6.1. DUST: Mid-Fidelity Aerodynamic Solver

DUST is an open-source software developed by Politecnico di Milano and released under MIT license that solves different aerodynamic problems with flexible and reliable approach.

The code is written using the latest object-oriented paradigms of FORTRAN and integrates different aerodynamic models for solid bodies, such as surface panel, vortex lattice and lifting line, that allows for different model fidelity levels.

The mathematical formulation of the problem is founded on the Helmholtz decomposition of the velocity field, a Lagrangian description of vorticity field and the incompressible flow hypothesis.

DUST requires only the surface mesh of the model that is used to build a piecewise-uniform distribution of doublets and sources associated with surface panels (as done in Morino formulation [13]). The wake is shed from a prescribed point of the lifting bodies and is initially modelled as a panel (shares same characteristic of the surface panel of the bodies). As the simulation evolves in time, based on a time step algorithm, the wake develops and at a certain point (defined by the input given by the user) the wake panels are converted into vortex particles. This method is called Vortex Particle Method (VPM) and allows a more robust wake formulation that can well represent the interactional aerodynamics between different bodies.

The code computes aerodynamic loads using different approaches and simplifications based on the aerodynamic model used to describe the different bodies. It's worth noting that for both surface panel and vortex lattice elements the viscous effect on the aerodynamic load isn't considered (current DUST version 0.8.2-b) and the compressibility effects are only partially recovered using Prandtl-Glauert correction.

A deeper explanation of the DUST formulation can be found in Appendix A.6 and [14].

6.2. SU2: High Fidelity CFD Code

SU2 (Stanford University Unstructured) is an open-source collection of software tools written in C++ and Python with the specific aim of solving partial differential equations (PDE's), multiphysics simulations and PDE-constrained optimization problems. For these reasons it has been chosen as the high-fidelity tool. SU2 primarily employs the Finite Volume Method (FVM) to

discretize the governing equations, which is widely regarded for its conservation properties and flexibility in handling complex geometries and robustness in solving fluid dynamics problems.

6.3. Euler Analyses

For these first analyses the solver employed is the compressible Euler in SU2, a compressible and inviscid solver, which allows to decrease drastically the computational power needed with respect to a viscous simulation and allows to conduct also an optimization study. The reduced computational time is because the viscous term's solution does not need to be solved, thus requires less equations to be solved and a less costly mesh topology. Although this hypothesis seems very strong, the effect of viscosity can be neglected in this preliminary phase, being that the idea is to capture an estimate of the wave drag and the lift coefficient. By also considering that the maximum angle of attack considered in this work is 6° , it is realistic to say that the lift coefficient is not extremely influenced by viscosity. Moreover, the capability of the Euler solver to consider the presence of shock waves is a powerful tool, which allows to study in a proper way the behavior of the wing in transonic conditions and for such reason, the objective of this chapter is greatly focused on reducing wave drag in sustained turn.

The computational cost of a viscous design process is at least an order of magnitude higher than for design using the Euler equations. This is true also for the simple wing case: the simulations done with a Euler solver took less than half an hour to reach full convergence, while the RANS simulation took around 6 hours to reach convergence. This is due to different reasons: first the mesh needs to be more refined in order to resolve the boundary layer solution as well. Secondly there is an additional computational cost coming from the computation of viscous terms and the turbulence modeling. Moreover, the convergence is also slower when compared to an inviscid flow simulation.

Since Euler analyses fail to consider viscous drag and so all the results of L/D in this section must be taken with care as are overestimation of the real aircraft performance.

Some considerations are made on next paragraphs regarding simulations and meshing. To avoid repetitions, these sections relate to every simulation done with SU2 for both RANS and Euler, as well as for both isolated wing and complete aircraft.

6.4. RANS Analyses

RANS simulations have been carried out to understand the difference in transonic behavior when viscosity is considered and to analyze one high angle of attack condition. A RANS simulation is the most economic approach in CFD for predicting turbulent flows. This method involves averaging the Navier-Stokes equations over time, thus transforming the inherently unsteady and chaotic nature of turbulence into a more manageable set of steady-state equations. The primary goal of a RANS simulation is to compute the mean flow properties, which necessitates the introduction of turbulence models to account for the effects of turbulence on the mean flow. All the simulations performed for the project were developed deploying the Spalart-Allmaras turbulence model, which the literature shows to be one of the most adequate for external flows (especially in the aeronautical field) [15]. Enhancing the resolution of the boundary layer within a RANS simulation is fundamental for accurate predictions, as the boundary layer encompasses the region where viscous forces are significant and gradients in velocity, temperature, and other flow variables are steep.

Adequate resolution in this region ensures that the intricate dynamics of the boundary layer, including the development of turbulence and its interaction with the mean flow, are captured with high fidelity. This often requires fine mesh spacing near the walls to resolve the velocity and temperature profiles accurately, ensuring that the $y+$ values fall within an optimal range, typically between 30 and 300 for standard wall functions without having perfect accuracy, which is nearly impossible to obtain with limited computational power. This feature characterizes the first layer height of the grid h , to let the wall functions work as their optima:

$$h = y^+ \frac{\mu}{U_{fric} \rho}, \quad U_{fric} = \sqrt{\tau/\rho}, \quad \tau = c_f \rho U^2 / 2 \text{ and } c_f = 0.026 / Re^{1/7} \quad (6.1)$$

The mesh was then set up on this h , in order to maintain the computational cost as low as possible but with no compromise on solution accuracy. Enhanced boundary layer resolution is crucial for obtaining reliable and precise simulations of aerodynamic performance, heat transfer, and other phenomena influenced by near-wall turbulence effects.

As the analysis was performed on a wing, the same domain shape and size of the Euler analyses was used. Practically speaking the application of the no slip condition on the wing is the only modification, as the other boundary conditions were not modified. As for other numerical methods, the SU2 tutorials [16] present an analysis of the ONERA M6 wing, whose numerical setup is provided, as well as the results are compared with the experimental ones. As said in the Euler isolated wing setup described in Chapter 7, the flow conditions for the designed wing are similar to the ONERA M6's conditions thus, the same numerical approach as [16] can be used to carry on this study.

Obviously, a grid convergence analysis has been done for this analysis too and is presented in Appendix. It is easy to notice that an effective grid convergence is not met in this case, although the trend seems to signal a near-convergence. It is not possible to analyze a case with a higher cell count because of the computational limitations: 4.8 million cells are the estimate of maximum cell count for a compressible RANS simulation with SU2 and 16 GB of RAM memory. The RANS simulations have a lower maximum cell count due to the higher number of equations needed to solve the viscous contribution.

6.5. Meshing for SU2

This section will be dedicated to all the considerations and passages strictly related to the meshing process.

To obtain affordable and accurate results from the CFD analysis it is of fundamental importance to prepare the mesh carefully. The objective of this phase is to distribute the elements in the computational domain where a more accurate solution is needed, according to which computational power is available for the analysis. For this reason, more elements will be concentrated in zones where we need to get more accurate results, giving less importance to parts where less accuracy is needed.

During this process, a powerful industrial tool which easily provides extensive capabilities for generating high-quality meshes is utilized. Moreover, in the context of a complex 3D geometry like the STAD-1, the possibility to interact with a user-friendly interface is extremely useful for taking full advantage of the features available.

Since these analyses have been done with a symmetrical body in symmetric conditions, as is common in most CFD analyses, it has been decided to work on half of the model. This can be achieved by applying a boundary condition of symmetry, which acts like a mirror, enforcing that the flow variables on the symmetry plane are identical to those on the mirrored side, ensuring that the simulated half behaves as if the entire model was being analyzed. This choice allows to significantly reduce the domain size and thus the number of cells needed, consequently reducing the computational costs of the numerical simulations.

6.5.1. Mesh Topology

Regarding the choice of mesh typology, an unstructured mesh was opted for the entire domain. Compared to a structured mesh, it requires more time to be generated but offers higher precision when adapting to complex geometries. It is in fact particularly suitable for meshing irregular and curved surfaces. Another important aspect to consider is that, when dealing with a

significant number of elements, an unstructured mesh allows for a change to the element density in a specific region without the need for major changes in the surrounding areas.

6.5.2. Surface Mesh Generation

This process involves transforming a geometric model into a discrete representation that approximates its surface. In the following section, a brief dive into the methods and techniques employed in the generation of surface meshes will be done, highlighting their significance and applications.

While the mesh software used helps in generating an initial automatic mesh of the model, the real challenge remains in making all the elements match the smallest construction lines of the CAD model so that they reproduce the geometry as faithfully as possible. Zones where more attention must be paid include the air intake, the leading and trailing edges of the wing and tail, and areas where the geometry curvature is more accentuated and sharp edges are present.

To illustrate the level of detail required, the following images show a small portion of the total mesh, which required more detailed attention to ensure accuracy and regularity of the grid.

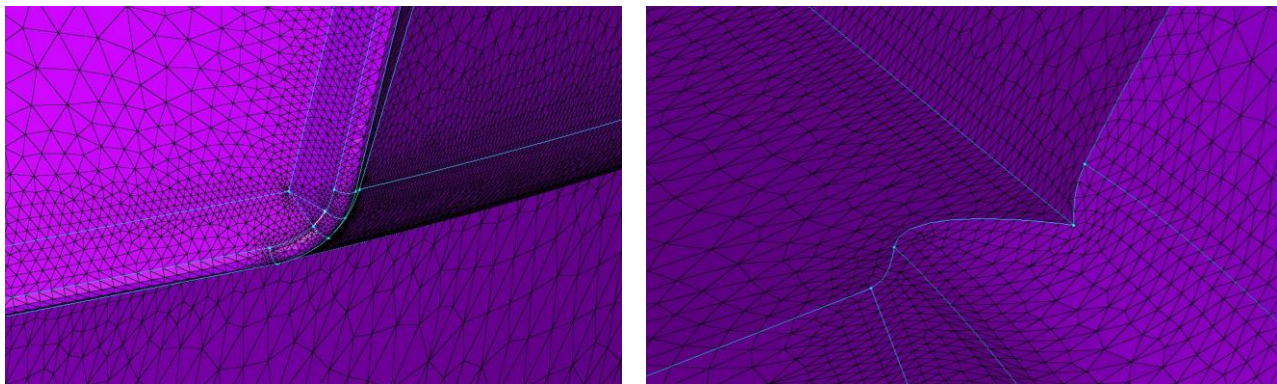


Figure 30 - On the left the right lower edge of the air intake, on the right the intersection between the nozzle and the fuselage.

6.5.3. Volume Mesh Generation

Once the surface mesh has been created, an extension of the generation of elements to the farfield can be done, which, with respect to the symmetry plane, has been set as a box of 100x80x100 meters. Here, the variation of element dimensions from the aircraft to the farfield has been controlled using the '*Decay*' parameter, set to a value of 0.8. (it varies from 0.0 to 1.0; a value of 0.0 indicates no influence beyond the boundary of the influence topology while a value of 1.0 indicates maximum influence).

Regarding the choice of domain dimensions, they are based on having nearly five times the length of the aircraft in the X, Y, and Z directions. Since inviscid simulations are carried out at first, there is no wake to capture along the X-axis. This is why not much importance is given to the backward zone, as would be necessary in a RANS simulation.

6.5.4. Grid Quality Criterions

One of the iterative steps done during the meshing phase is to check its 'quality'. This term refers to how the dimension, position and shape of the elements are set so that the CFD solver is put in an advantageous position to reach convergence. In general, it has been demonstrated that the quality of the mesh has a greater impact on the speed and reliability of the simulation's convergence than on the precision of the results [17]. As a result, any errors in the solution that arise from poor or incomplete convergence cannot be overlooked and must be taken into account.

Different parameters are available to monitor the mesh quality:

- **Intersections:** this is one of the first parameters to be checked, as a volume mesh cannot be generated if some elements intersect. In fact, a watertight grid is crucial for accurate simulations because gaps or overlaps can lead to incorrect calculations of flow fields.
- **Aspect ratio:** the ratio of the longest edge length to the shortest edge length in a cell is an important metric. In these analyses' case, there is only a small zone where a few elements with a high aspect ratio are concentrated, which coincides with the intersection between the air intake and the LEX. Due to the complexity of the geometry in this area, a better result cannot be achieved. Nevertheless, every element of both the surface and the volume mesh is well below the desired maximum value of 10.
- **Skewness:** measures the deviation of a cell from the ideal triangular shape on the surface and equiangular in the volume for the unstructured mesh. By checking this parameter, which ranges from 0 to 1, a satisfactory mean value of 0.197 across the entire domain is obtained for the worst case.

6.5.5. Boundary And Freestream Conditions

Once the volume mesh of the domain is fully developed, the last stage where the mesh software generator is needed is the setting of the boundary conditions, so that they get included in the input file for SU2. The following considerations allow for an explanation of the conditions used.

A list of the conditions imposed is reported here:

- **SYMMETRY:** defined on the surface where the plane of symmetry of the aircraft is located.
- **FARFIELD:** defined on the other five faces of the domain box where asymptotic conditions are imposed.
- **MARKER_INLET:** this marker allows to set the air density and velocity at the nozzle of the aircraft. It is important to note that SU2 interprets the concepts of input and output relative to the defined domain. Therefore, it may seem counterintuitive, but because the interior of the aircraft is outside the meshed domain, an inlet condition at the nozzle is applied.
- **MARKER_OUTLET:** set the freestream static pressure on the surface of the air intake, with the same logic explained for the inlet.

	Air Density at the Inlet [kg/m ³]	Velocity at the Inlet [m/s]	Static Pressure at the Outlet [Pa]
Mach 0.50	0.5849	319.87	57182
Mach 0.85	0.9589	282.33	57182

Table 17 - Values imposed for inlet and outlet marker.

The final boundary conditions are all either MARKER_WALL for the Euler analyses, which imposes a slip condition, or MARKER_HEATFLUX for RANS, set with a null heat flux, have a no slip condition. These are specified for the whole aircraft. In particular, the three main sections of the model (fuselage, wing, and tail) are further subdivided to facilitate easier analysis and evaluation of how each component contributes to the overall aircraft performance during postprocessing, but the subdivisions have been different based on each simulation's objective and thus they are not presented. Obviously, for the isolated wing analysis, the fuselage, tail, intake and nozzle regions do not exist, and the symmetry plane is considered at the root of the wing to have a less stringent condition with respect to a slip wall. This is physically incorrect but acceptable because the wing analyses' objective is to compare the different airfoils.

6.5.6. Grid Convergence

After the numerical setup has been done, the next step has been to evaluate the effect of the grid on the global aerodynamic coefficients. When dealing with a CFD simulation it is important to ensure that the results are grid independent, which means that they do not change with the grid size and with the number of elements of the mesh. This is done by refining the mesh until the results are not affected by the grid size. Generally, the surface mesh is refined by changing the minimum and maximum allowable cells, thus changing the volume mesh count as well, being that the meshing software starts from the surface cell size and subsequently decays the discretization going further from the body.

The process has been employed for every type/condition of analyses done. For the sake of generality, only one grid convergence analysis is presented, which is the one for the baseline isolated wing analysis with Euler. Every isolated wing analysis also reached a 10^{-12} order of magnitude of the residual on the density, which is used as the merit parameter for iteration's convergence; using this value allows to have extreme stable aerodynamic coefficients up to the 6th decimal. For reference, Figure 31 depicts the grid convergence results for the sustained turn condition; a similar behavior can be observed for the loitering condition too.

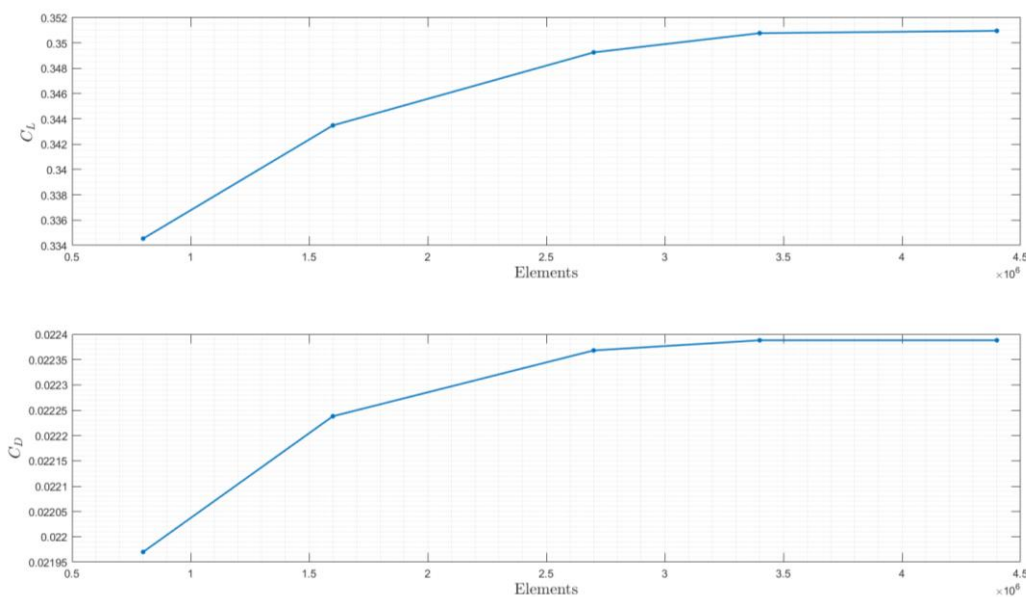


Figure 31 - Grid convergence results for the isolated wing for Euler.

The drag coefficient's difference between the grids is so small that it could even be due to computational error, thus the criterion for choosing the grid is based only on the lift coefficient. Due to the limited computational resources, every cell selection is done by conserving a good trade-off between CPU time and accuracy.

6.6. STAD-1 Model in DUST

As explained in [14] DUST has two possible ways to build component: using a parametric built-in editor or by importing surface mesh in ASCII or CGNS format.

Both input procedures have been used to model the STAD-1 aircraft configuration. An ASCII surface mesh built using the meshing software has been imported to model the fuselage while for all the “aerodynamic surfaces” a parametric definition has been used. All the data has been retrieved from the CAD of the aircraft apart from the LEX that has been designed following an iterative process directly in DUST.

Finding the correct way to model the aircraft in DUST has been a key part of the work. Since DUST is a potential solver based on a VPM method the lifting leading edge vortex generated by the LEX can't be observed directly.

Two simplified models have been developed to have the possibility to observe the effect of the vortex generated by the LEX on the wing, fuselage, tail and wake.

6.6.1. Lifting Line Vortex Model

In this model the fuselage has been modelled as a bluff body which doesn't release wake in the domain, the wing and tail are two panel lifting surfaces while the LEX is composed of two sub-components. A lifting line, which models the vortex lift generated from the leading edge, and a Vortex lattice lifting surfaces, which models the actual LEX surface and shape.

In this way the effect on both the LEX and wing surface of the longitudinal vortex generated by the LEX leading edge would be observed. Unfortunately, a way to predict the intensity of the LE vortex starting from the free flow condition and LEX shape were unable to be found. The only way to find this data would have been through a long series of RANS simulations that were too expensive for our computational capabilities.

6.6.2. VLM TE Vortex Model

An easier but still good model that overcomes the difficulty just presented can be built as follows: the fuselage, wing and tail are model as explained for the "lifting line vortex model" while the LEX is simply represented by a vortex lattice lifting surface.

In this model the effect of the lifting vortex on the LEX surface is lost since the vortex particles that represent such vortex are shed from the TE of the LEX surface. However, is still possible to observe the mutual influence that a longitudinal vortex structure and the wing have, which is the main interest of this work.

6.7. DUST Sensitivity Analysis

Once the model has been decided a series of sensitivity analyses has been performed to find the best trade-off between precision and computational cost (expressed in terms of CPU time). The input variables analyzed by the sensitivity analysis were:

1. wing mesh size
2. time step length of the simulation
3. gap between wing and fuselage components
4. wake box longitudinal dimension

The flow conditions and geometry component considered during the sensitivity analysis are reported in the following table:

Mach [-]	Static pressure [Pa]	Density [kg/m^3]	Kinematic Viscosity [m^2/s]	AOA [°]
0.30	57182	0.7708	$1.642 \cdot 10^{-5}$	5

Table 18 – Free stream conditions for DUST sensitivity analysis

6.7.1. Mesh Size

A spatial sensitivity analysis of the mesh of the isolated wing has been performed first. This run has been done considering the other variables set at a reasonable value to obtain high precision results. The time step has been set to 0.003 sec and the box length to 20 m. Six different meshing solutions have been considered, each one identified by the number of surface panel elements in chord, while the span-wise discretization has been adjusted proportionally. Once the parametric run has been finished the results have been post-processed in two

different sets of graphs. First of all, as reported in Figure 32, the convergence of F_z and M_y over time has been verified for all different meshing solution, then the integral loads have been nondimensionalized to evaluate the effect of the different discretization on C_z and C_m . Finally, the different CPU times required to execute the simulation have been plotted. The results have shown a good convergence over time for all the mesh tested. In terms of load a particular small variation in the force and moment coefficient of the two refined configurations has been observed. For this reason, the choice has been driven by the CPU time; so, the mesh with 20 elements along the wing chord have been chosen since it guarantees the best compromise between computational time and accuracy.

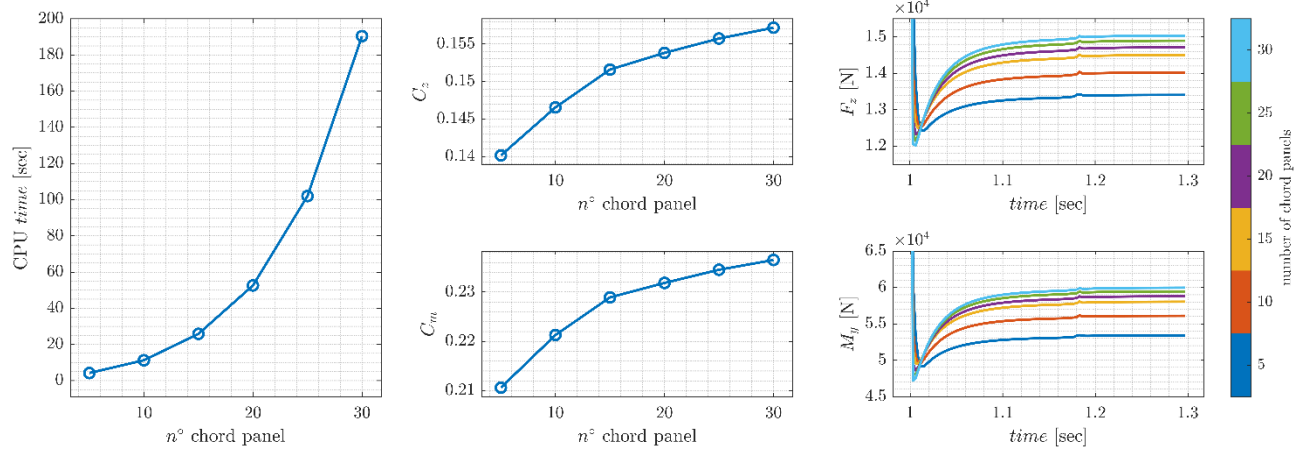


Figure 32 – Mesh size sensitivity analysis

An interesting observation can be made by watching the result obtained with the coarsest mesh tested. Due to the small amount of panel the wing airfoil hasn't been discretized sufficiently good and so the results in terms of integral loads results way more different compared to the other values.

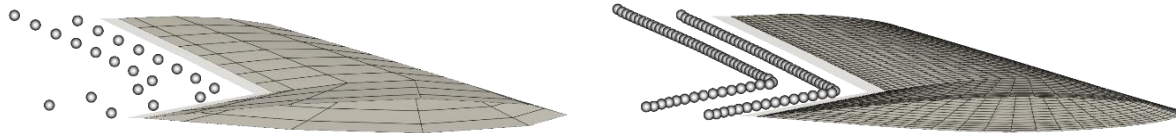


Figure 33 – Compare between coarse and refined mesh

This situation can be easily seen by watching the 3D visualization post processed using DUST_post reported in Figure 33.

6.7.2. Time Step

A time step sensitivity analysis has also been performed by running the same simulation between 1 and 1.3 sec and gradually decreasing the time step starting from $\Delta t = 0.1$ sec until $\Delta t = 0.001$ sec. As done for the mesh sensitivity analysis the model considered has been the isolated wing with a box length value of 20 m. The wing has been meshed with 20 element chord-wise since, as just verified, it guarantees the best compromise between precision and time cost. The results of this analysis have been post-processed in the exact same way as before in Figure 34.

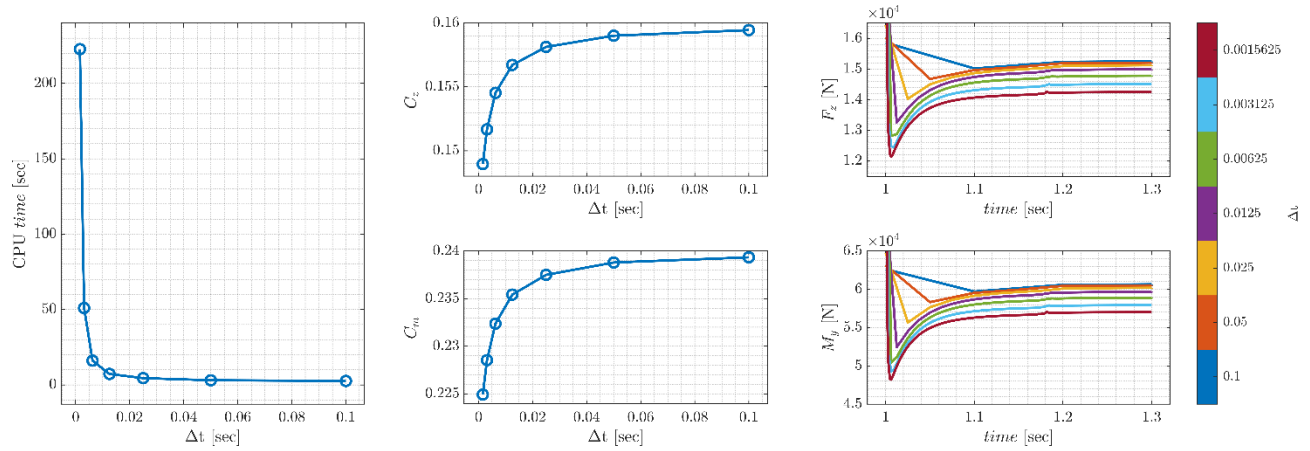


Figure 34 – Time step sensitivity analysis

It's interesting to notice how the integral loads change in a quite important way by reducing the time step to very small values. This is a common result in a VPM mathematic frame and is caused by the fact that the wake particles are shed with such a high frequency that the influence between each other (computed following the Biot-Savart theorem) tends to diverge to very high value due to the small relative distance between two consecutive vortex particles shown in Figure 35.



Figure 35 – Compare between biggest and smallest time step

The $\Delta t = 0.003125 \text{ sec}$ time step has been chosen since guarantee a well-defined wake without causing the integral loads to diverge to unphysical value. Also, in terms of convergence and CPU time seems to guarantee a reasonably good result as shown in Figure 34.

6.7.3. Fuselage Gap

Finally, the fuselage has been added to the model and meshed with a similar panel density to the wing. The effect of a different gap between fuselage and the root of the wing has been tested. Their analysis has been crucial since in DUST different geometric components, if some of them release wakes, must be placed next to each other avoiding panels intersections. For this reason, different mutual distances between wing root and fuselage tip panels have been tested. The gap tested starts from -50 mm and increases until 60 mm .

The simulations have been run with a time step of 0.003 sec and a box length of 20 m . The results have been post-processed as explained in the previous cases Figure 36.

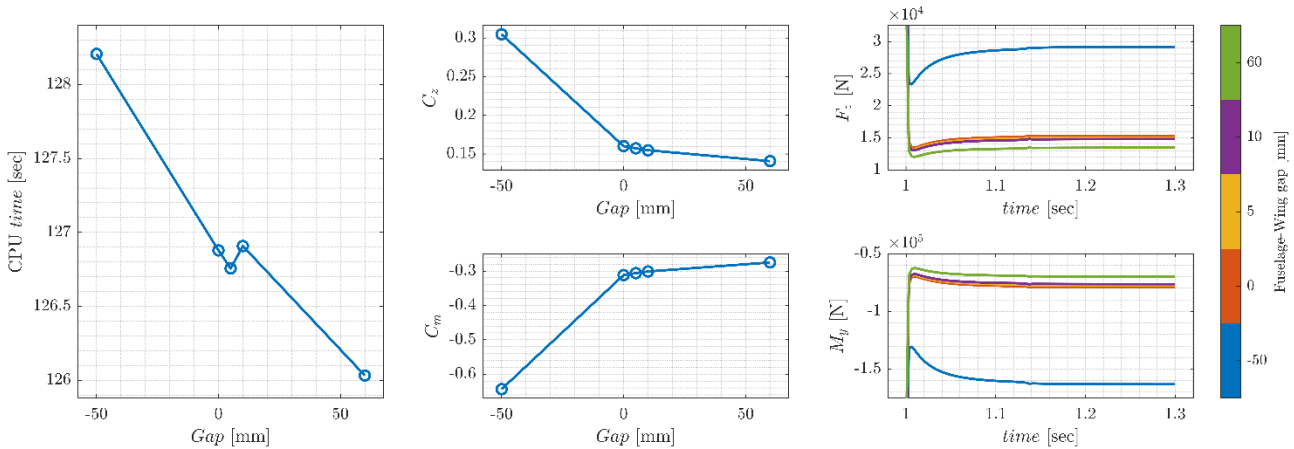


Figure 36 – Fuselage gap sensitivity analysis

Every gap value has led to a good convergence over time as visible in Figure 36. Since in terms of C_z and C_m the results are pretty much the same considering a gap between $0.000m$ and $0.010m$, the choice has been made based on the CPU time cost. So, the selected gap between fuselage and wing root has been $0.005m$. The same gap will also be used to model the connection between tail root and fuselage and LEX and fuselage.

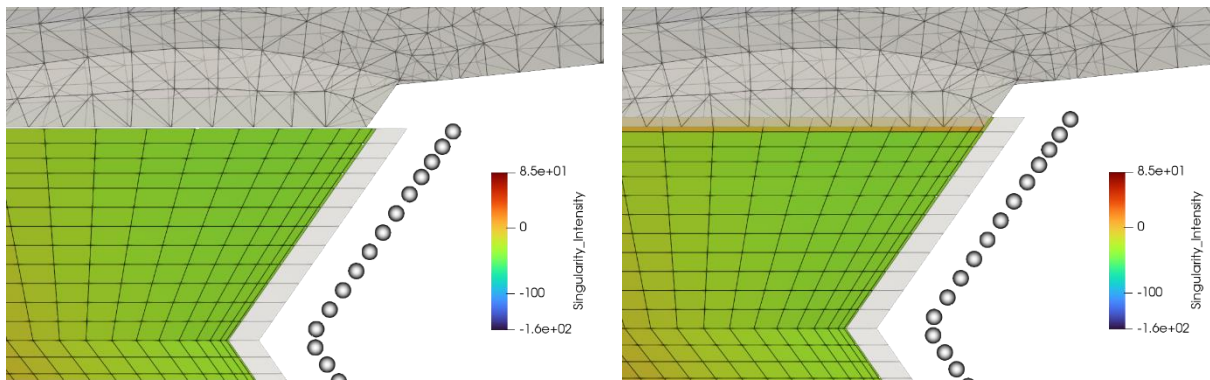


Figure 37 – Compare between negative and positive fuselage gap

As expected, the negative gap value produces an integral load extremely different compared to the other. The incorrectness of this value can be also verified by watching the visual time marching simulation of the -50 mm gap. The panels intersected with the fuselage present a very strange singularity distribution (Figure 37) on the surface panels. Also, the big positive gap of 60 mm has given a result quite different to the other. This happens because the “big” gap compared to other leads to a more mitigate effect of interaction between fuselage and wing.

6.7.4. Wake Box

At the end, a sensitivity analysis on the full aircraft configuration has been performed to assess the influence of the length of the computational domain. This has been done since DUST allows us to define a perimeter within the vortex particles influenced the aerodynamic problem. The different value of box length considered vary linearly between 10 m and 25 m . The simulation has been done considering as input variables for surface mesh, time step and fuselage gap the values just chosen and the results has been post-processed as for the previous cases and show in Figure 38.

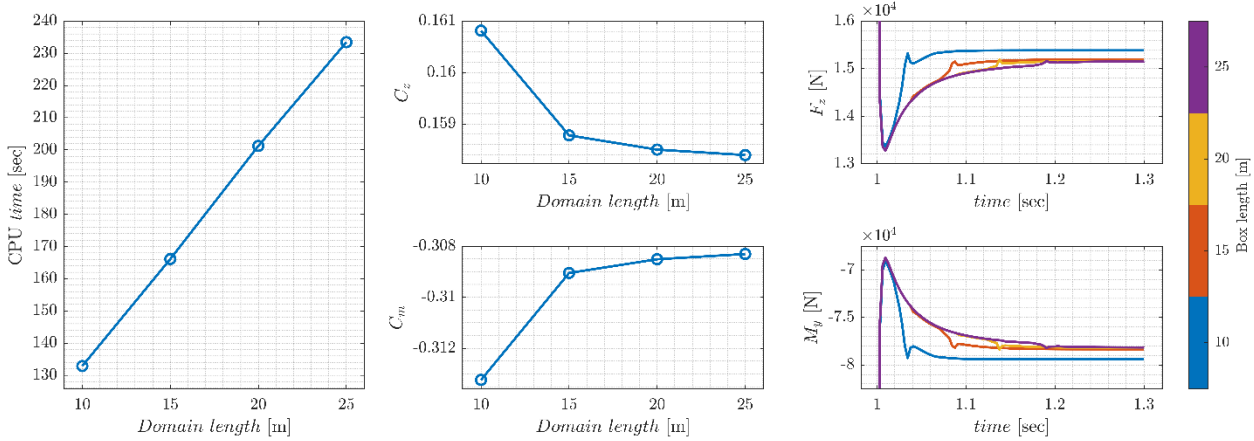


Figure 38 – Wake box sensitivity analysis

Once again, every box length value tested has led to convergence, but the result in terms of C_z and C_m is quite different between 10m and every other value. 15 m, 20 m and 25 m produced quite similar integral load values at convergence, so the choice has been driven by the trade-off between computational cost and precision. For this reason, the picked box length value is 20m.

6.8. DUST Comparison with Euler

After a preliminary validation of DUST executed on the well-known test case of the ONERA M6 (see Appendix A.8) some more specific comparison has been executed on the STAD-1 specific wing and aircraft geometry to verify that even by considering more complex geometry the results of the mid-fidelity software was pretty much aligned with SU2. This second phase of validation has been divided into two different steps: first, the STAD-1 lambda wing has been studied in subsonic condition, then the complete aircraft model has been considered, still in subsonic condition, to test that the presence of the fuselage and tail would have been well captured by DUST. Both comparisons have been executed in subsonic regime since, as seen in Appendix A.8.5, the considered mid-fidelity method is not capable of capturing complex compressibility effects and singularities such as shock waves.

6.8.1. Isolated Wing

The STAD-1 lambda wing has been built in DUST using the parametric built-in editor as surface panel lifting body. The mesh refinement and all the other DUST input variables has been selected through a sensitivity analysis (as done in [18]) reported in section 6.7. The free stream condition considered were $M_a = 0.30$ at $h = 15,000ft$ (the same used in the sensitivity analysis).

As already observed for the ONERA M6 in Appendix A.8.4, by comparing side-by-side the pressure distribution on the isolated STAD-1 lambda wing in pre-stall condition ($\alpha = 5^\circ$) as shown in Figure 39, the results are very good.

The two distributions are very similar over the whole wing except for some minor differences near the wing tips. This part has been modelled in a slightly different way on the two software models. For this reason, minor differences in the surface pressure distribution are expected. Though these differences should not impact the integral loads results in a significant way.

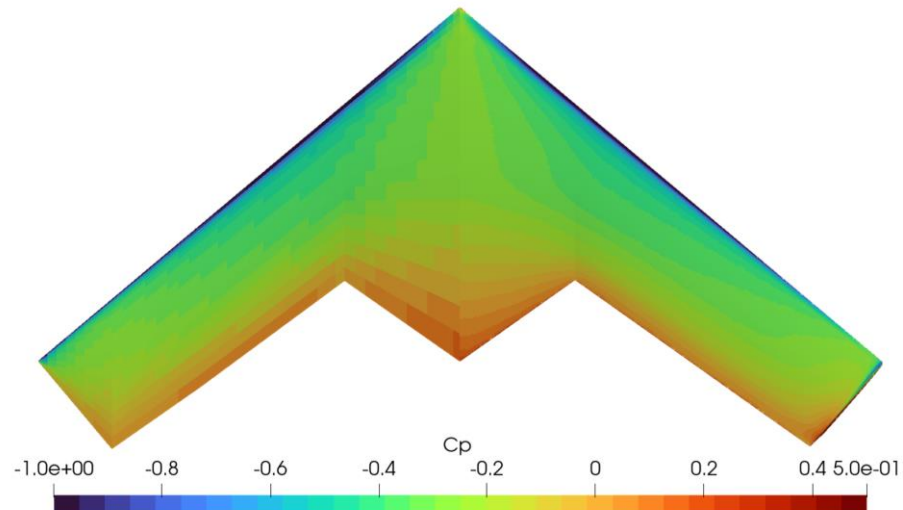


Figure 39 – STAD-1 wing surface pressure distribution at Mach 0.30 and AOA 5°.

The situation is very different when the condition analyzed is $\alpha = 15^\circ$ as shown in Figure 40. The surface pressure distribution results very differently because of the early separation (near leading edge) that isn't modeled by the potential method implemented in DUST. Anyway, even the SU2 results must be considered only indicative and not totally correct since for such a complex wing geometry (as delta and lambda wings) viscous phenomena act an extremely important role at near-stall to post-stall angles of attack. Complex 3D flow interaction such as lifting vortex cannot be seen and considered through a “simple” Euler CFD analysis.

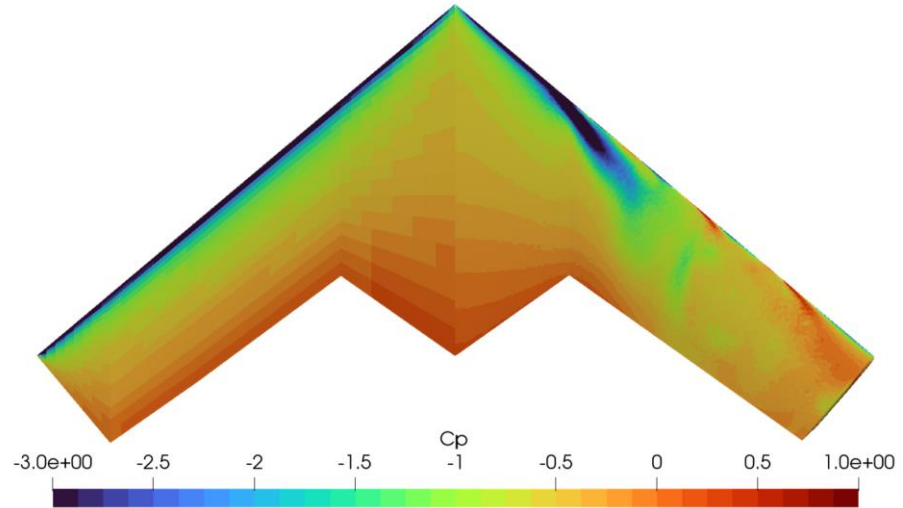


Figure 40 – STAD-1 wing surface pressure distribution at Mach 0.30 and AOA 15°.

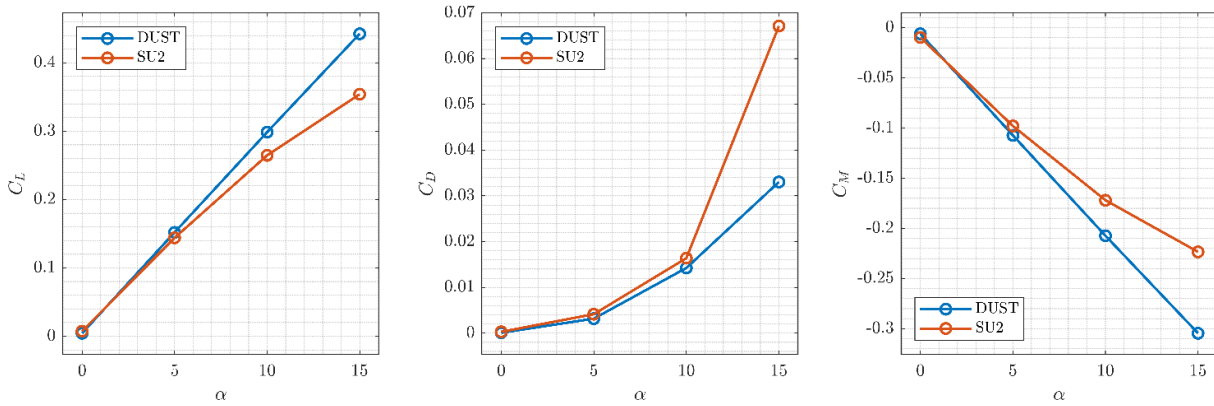


Figure 41 – Aerodynamic force coefficient for STAD-1 isolated wing at $M_a = 0.30$ and $h = 15,000\text{ft}$

The differences observed in the visual representations are, once again (as seen in A.8.5), confirmed by the aerodynamic force coefficient plots reported in Figure 41. So, the conclusion drawn from this comparison is that DUST can represent with good precision even complex wing geometry in pre-stall (until $\alpha \approx 10^\circ$) subsonic condition.

6.8.2. Complete Aircraft

Considering the good result obtained with the isolated lambda wing in DUST, a step forward has been executed in terms of complexity of the model considered.

The STAD-1 aircraft has been built in DUST following the “VLM TE vortex model”. Once again, the DUST input variables have been the one found during the sensitivity analysis and the free stream condition are the same as before ($M_a = 0.30$ at $h = 15,000\text{ft}$).

The results are quite like the ones obtained for the isolated wing. The surface pressure distribution obtained at $\alpha = 5^\circ$ as shown in Figure 42, DUST (left half) results are very well representative and similar to the one obtained with SU2 (right half).

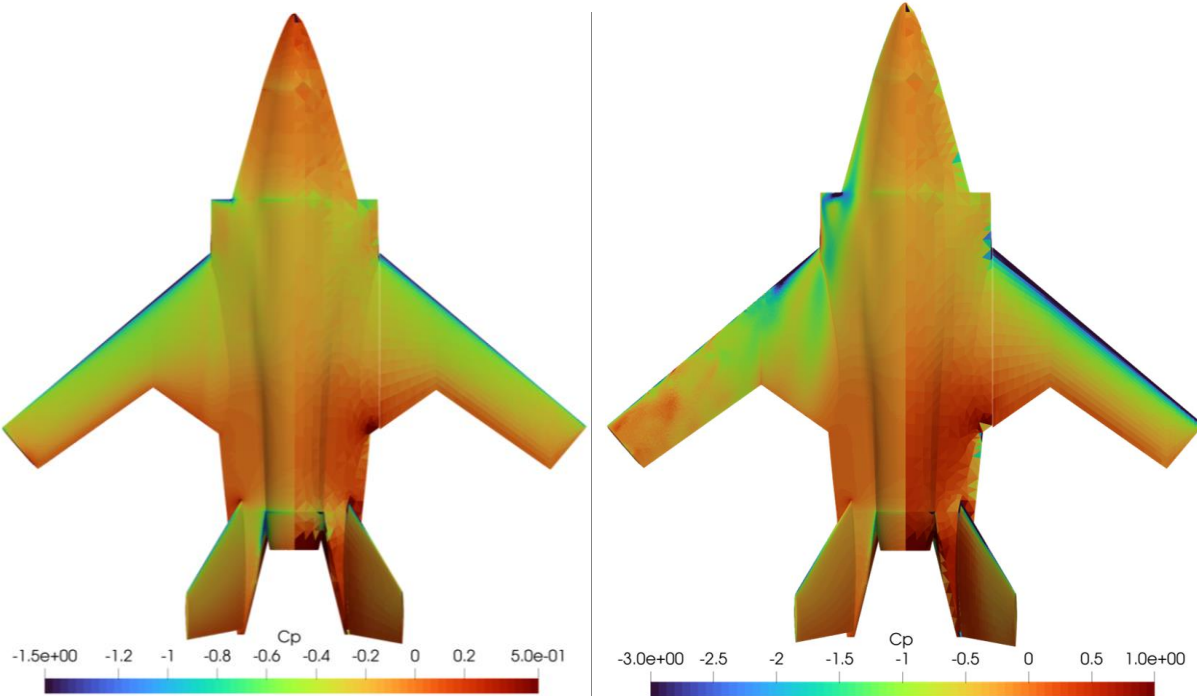


Figure 42 – STAD-1 wing surface pressure distribution at Mach 0.30 and AOA 5° (left) and 15° (right).

Some imprecisions can be noticed in correspondence of the root TE of the wing, the root LE of the tail, the aircraft nozzle and fuselage LE. These imprecisions are caused mainly by the fact that the surface panel distribution of the fuselage isn't perfectly uniform. In the small zone where the surface mesh results more refined the distance between control points of the panels is too small and, as explained for the wake particles, leads to local unphysical results. Anyway, this problem happens only on the fuselage part of the model, so it doesn't impact the integral loads of the wing in severe ways.

The situation is very different when the results of the simulation at $\alpha = 15^\circ$ is considered. As seen for the isolated wings the surface pressure distribution obtained is very different. The differences are bigger since, as seen for the wing, all the complex viscous phenomena on the fuselage and its interaction with the wing, typical of the near-stall regime, aren't considered. So, the error in the DUST results is expected to be even bigger.

Finally, it's, once again, important to remember that even the SU2 results at high angle of attack will be subjected to a quite important error since the solver employed is the compressible Euler (inviscid).

As expected, the results in terms of integral loads on the wing (reported in Figure 43) are quite good and aligned until 10 degrees of angle of attack (in terms of C_L).

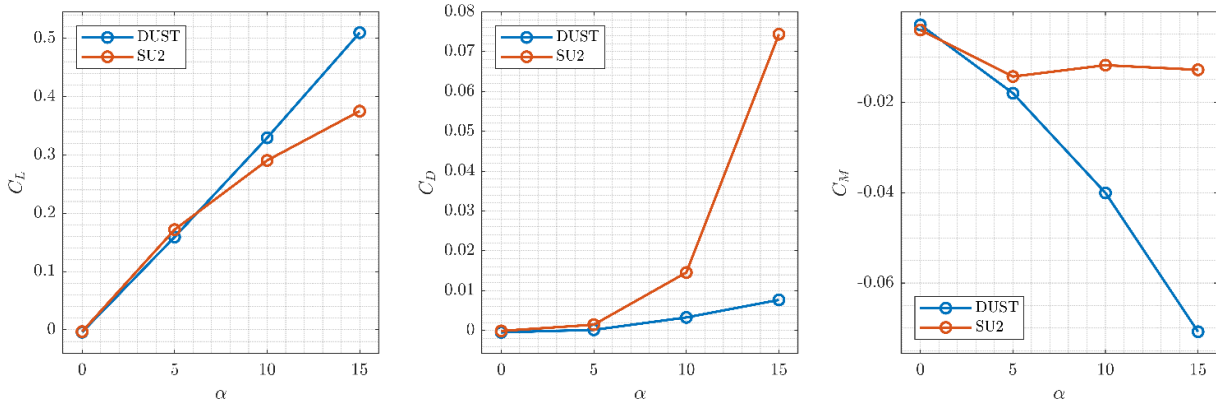


Figure 43 – Aerodynamic force coefficient for STAD-1 aircraft at $M_a = 0.30$ and $h = 15,000ft$

Considering the entity of the error committed by DUST until $\alpha = 10^\circ$ and, most important, the fact that the trend of results is aligned, even if with a different slope. DUST has been considered a good and reliable method to execute the LEX first sizing.

The two big advantages of DUST when compared with SU2 are: the computational time and the model pre-processing process.

In terms of DUST computational cost, when run with optimal input variables obtained through sensitivity analysis, the time needed to perform a complete simulation at a defined angle of attack of the full aircraft is around 4-6 minutes. Considering the same simulation performed with SU2 the computational time required to reach a good level of convergence on the same hardware is around 15-45 minutes depending on the conditions. Anyway, the big advantage of DUST against SU2 comes when the pre-processing time cost is considered. Since, as explained, the dust model is built by DUST_pre starting from easy editable text file all the CAD design and volume meshing mustn't be repeated every time an aerodynamic part is added to the model (as done with the LEX). This difference impacts tremendously the time needed to perform analysis in the same free stream condition on different LEX designs.

7. Wing Airfoil Selection and Analysis

Description of the process used to select the airfoils and resulting CFD analyses is here reported.

Due to the medium aspect ratio planform, the flow behavior is strongly tridimensional and thus airfoils are not as important as the planform. As said by Ing. Giorgio Travostino, for this type of wing the airfoil depends on the planform shape, so for this reason the airfoil selection has been done only after the full planform design.

As there is a vast amount of choice of airfoils, a preliminary requirement on the maximum thickness t/c and the curvature must be made. To evaluate the t/c , the Korn equation (7.1), derived from AGARD AR-256 [19] has been used. For selecting the curvature, a symmetric airfoil was chosen as the baseline, with higher curvature applied only to achieve an elliptical lift distribution and delayed wingtip stall. Moreover, inspiration was taken from similar aircraft, with data derived from the incomplete airfoil guide [20], leading to the curvature distribution presented in chapter 3. The Korn equation allows to find the maximum t/c' of the airfoil usable to avoid drag divergence on the wing given the normal drag divergence Mach $M_{a_{DD}}^{Normal}$, the airfoil coefficient C_L^a , and an airfoil technological factor K_a , which is equal to 0.87 for NACA airfoils, and 0.95 for supercritical airfoils:

$$\frac{t}{c'} = K_a - \frac{C_L}{10} - M_{a_{DD}}^{Normal} \quad (7.1)$$

The equation has been subsequently modified to consider the effect of the sweep angle. Torenbeek [21] gives the following relationships:

$$M_{a_n} = M_a \cos(\Lambda_{LE}); C_L^a = \frac{C_L}{\cos(\Lambda)^2}; c' = \frac{c}{\cos(\Lambda)} \quad (7.2)$$

The previous equations allow to derive equation (7.3), which outputs the maximum allowable t/c on the wing. The equation has been cross verified with the derivation made by Mason [22]:

$$(t/c)_{max} = \left(K_a - \frac{C_L}{10 \cos(\Lambda)^2} - M_{a_{DD}} \right) \cos(\Lambda_{LE}) \quad (7.3)$$

$M_{a_{DD}}$ is derived from the definitions given by Boeing and Douglas [1]: for Boeing, $M_{a_{DD}}$ is the Mach for which the drag increase due to compressibility effect is equal to 20 counts, while for Douglas, the $M_{a_{DD}}$ is the Mach for which $\frac{dC_{D_0}}{dM}$ is equal to 0.1. Typically, civil aircraft have a cruise Mach equal to $M_{a_{DD}}$ defined by Boeing, leading to a $M_{a_{DD}}$ defined by Douglas, which is 0.06 Mach above the one by Boeing, as said by Raymer [1].

The approach taken has been to consider the sustained turn at Mach 0.85, which has the highest flight Mach with the highest C_L required, as the sizing condition for the $(t/c)_{max}$. This leads to a $M_{a_{DD}}$, as defined by Douglas, of about 0.86, which yields the maximum allowable $t/c = 0.11$ for NACA airfoils and $(t/c)_{max} = 0.18$ for supercritical airfoils with $\Lambda_{LE} = 40^\circ$.

As it can be seen, the values for supercritical airfoils are high. This said, the supposed wing planforms have a low to medium aspect ratio and thus a flow behavior that may not perfectly respect the normal Mach rule. This, added to the fact that a low t/c leads to a lower C_{D_0} , induces a choice of a conservative $(t/c)_{max}$, which is 0.1 for NACA airfoils and 0.12 for supercritical airfoils.

These considerations done lead to the baseline choice of the airfoils described in Table 7, used for the VLM analyses. Subsequently, Euler analyses are done on different airfoils configurations to find the best solution.

7.1. Euler Analyses

The first analyses have been made by considering the isolated wing and by focusing on the sustained turn flying condition ($M_a = 0.85$ and 15,000 ft). This is done to analyze different airfoils combination and understand the difference from the semi-empirical equations. To do this, various CAD models have been created with the aid of Airfoil Tools, which is a database that collects geometrical data of various airfoils, and airfoils have been changed based on their thickness ratio (ranging from 4% up to 12%) and their curvature (Considered up to 3% for NACA airfoils, and up to 7% for supercritical airfoils). Furthermore, the starting configuration is the one defined in paragraph 4.1.

For the Isolated wing analyses a common reference angle of attack has been selected for each design condition, to obtain a meaningful comparison between the different designs.

The selected reference conditions of the flow are reported in Table 19. Those conditions have been taken by considering the analyses done in OpenVSP paragraph 4.1 to fix the flow condition related to the considered performance and the AOA that will likely result in the target C_L values. Finally, for all these analyses, 3.3 million cells are used as discussed in the grid convergence analysis presented in 6.5.6.

Flow Conditions	$M_a = 0.50$	$M_a = 0.85$
Pressure [Pa]	57182	57182
Temperature [K]	258.65	258.65
Density [kg/m^3]	0.7708	0.7708
Angle of Attack [°]	4.5	6.0

Table 19 - Isolated Wing Flow Conditions.

First, the baseline configuration has been analyzed in SU2. The results, presented in Figure 44, clearly show the presence of lambda shockwaves as defined in [23]. These shockwaves consist of a first one that starts from the leading edge, caused by the small leading edge radius that accelerates the flow quickly, increasing its intensity moving towards the wing tip. Another clearly visible shockwave starts behind half of the root chord and extends towards the wing tip until it encounters the first shockwave due to a second acceleration phase. A third shockwave (not clearly visible in the analysis) forms from the wing tip and soon reaches the other two shockwaves. This last one is expected to be greatly influenced by the flat tip cap that induces a high acceleration on the flow at the wing tip edge.

This analysis also shows that the airfoil thickness, selected with the Korn equation, doesn't work as intended at the design M_a value. That is expected to be caused by the low aspect ratio and high sweep of the analyzed wing planform.

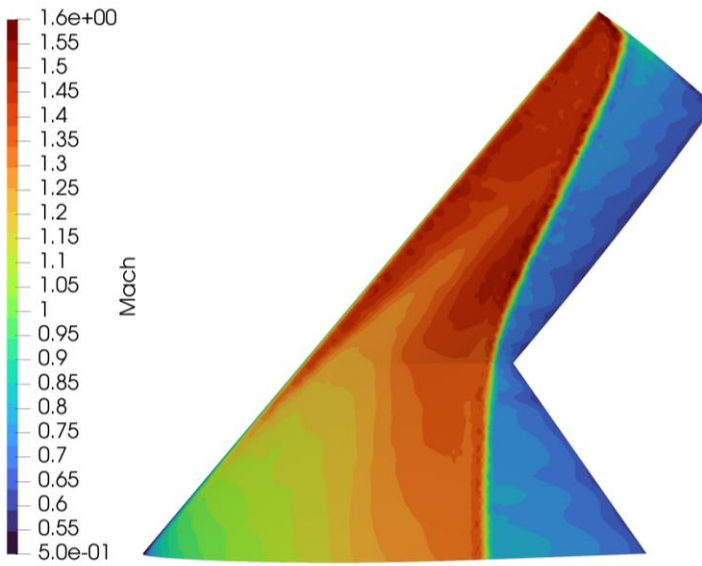


Figure 44 – Initial wing Euler CFD analysis at $M_a = 0.85$ and 15,000 ft.

Subsequently, different trials consisted of changing the airfoil thickness in order to see how that influenced the Mach number over the wing. Two cases have been tested, by changing only the airfoils' thickness and curvature and maintaining all the other wing geometric properties constant:

Wing Section	Initial Wing	Case 1	Case 2
Root	NACA 64A010	NACA 64A008	NACA 64A008
Mid	NACA 64A008	NACA 64A208	NACA 64A208
Pre-Tip	NACA 64A208	NACA 64A206	NACA 64A206
Tip	NACA 64A206	NACA 64A206	NACA 64A204

Table 20 – NACA 64 airfoil configuration over the wing.

The results are shown in Figure 45. Compared to the initial wing, it is possible to notice that the Mach number over the surface is noticeably reduced because the first shockwaves reached a position placed further along the span and so a greater wing portion has $M_a = 1.10 \div 1.30$. The results of these configurations are shown in Table 21.

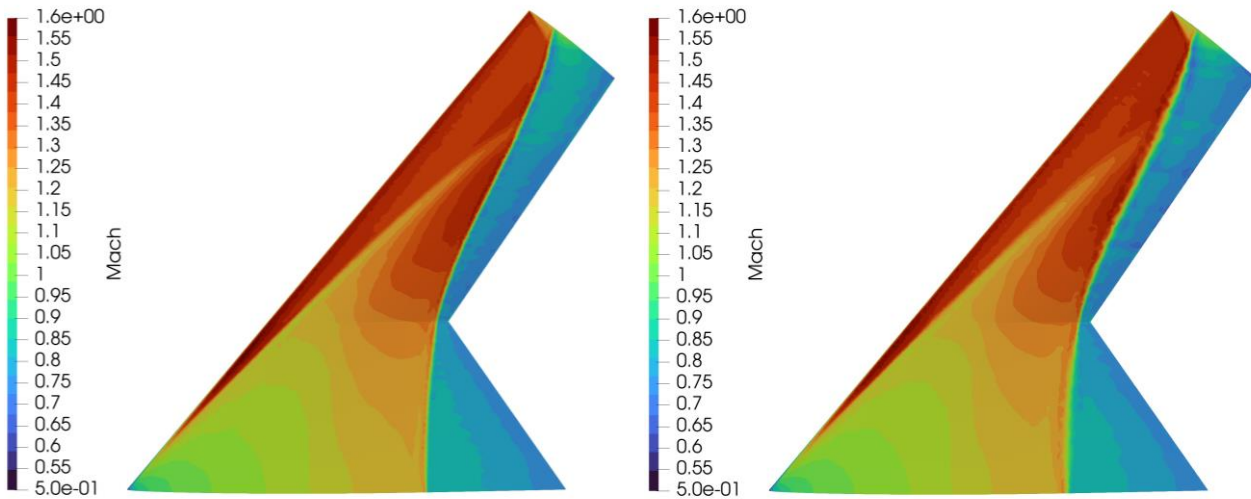


Figure 45 - Case 1 (Left) and Case 2 (Right) Euler analysis at $M_a = 0.85$ and 15,000 ft.

	Initial Wing	Case 1	Case 2
C_L	0.324	0.351	0.351
C_D	0.02790	0.02239	0.02278
L/D	11.61	15.68	15.41

Table 21 – Coefficient for NACA 64 designs, from Euler analysis at $M_a = 0.85$ and 15,000 ft.

	Initial Wing	Case 1	Case 2
C_L	0.158	0.181	0.182
C_D	0.00428	0.00523	0.00535
L/D	37.00	33.66	34.02

Table 22 – Coefficient for NACA 64 designs, from Euler analysis at $M_a = 0.50$ and 15,000 ft.

As expected, at $M_a = 0.85$, decreasing the thickness reduces the shock intensity over the wing, and thus supposedly reduces the wave drag contribution. The reason behind this is simple: a thinner wing imposes less acceleration on the flow compared to a thicker one, and so reduces the shockwave intensity. Further decreasing the thickness at the tip doesn't improve the C_D as expected, this is related to the flat wing cap.

Considering instead the results at $M_a = 0.50$, it is possible to see that by reducing the thickness the L/D get worse: a thicker airfoil accelerates the flow more and thus is able to generate a higher pressure difference, and thus a higher lift for a lower "cost" (since in these conditions shockwaves are not present). Considering that the focus of the optimization needs to be related at the transonic condition, it has been chosen to reduce the wing performance at $M_a = 0.50$ by preferring case 1. Differently from the situation at $M_a = 0.85$, placing an even thinner airfoil at the wing tip improves the L/D . For this reason and for also structural reasons a thinner wing tip has been adopted. Furthermore, these differences are minimal and do not change the wing performance noticeably, and so the main reason for the selection of a thinner tip airfoil is structural.

The leading edge has a big impact on the flow behavior: this is caused by the flow acceleration over the leading edge that causes the first shockwave to appear close to it. For this reason, an analysis has been performed changing the airfoil class. After some design trials considering more combinations of NACA 63, 64 and 65 airfoils, a new configuration has been selected with all NACA 65 airfoil reported in Table 23. It is important to note that 6 series airfoils are not chosen due to their laminarity, which cannot be considered without a viscous solver with transition models, but only due to their transonic behavior. Using these airfoils as can be seen in Figure 46, caused the shockwave to appear on a reduced portion of the swept wing section, compared to the NACA 64 case which, as can be seen in Table 24, lead to a higher L/D values. This is because of the following reasons: first the NACA 65 airfoils have a lower leading edge radius and thus accelerate the flow in a more abrupt way when at a certain angle of attack, causing the second shock to be anticipated, and so a higher portion of the wing is affected by a subsonic flow. This has been verified by an intermediate airfoil configuration, which hasn't been reported, consisting of the curvature and t/c of the Case 1, which resulted in an overall higher L/D . Furthermore, reducing the thickness in the mid-section further reduces the shockwave intensity and further increases the L/D . This configuration, named Case 3, has been finally selected and it is reported in Table 23.

Wing Section	Case 3
Root	NACA 65A008
Mid	NACA 65A206
Pre-Tip	NACA 65A206
Tip	NACA 65A204

Table 23 – NACA 65 airfoil configuration over the wing.

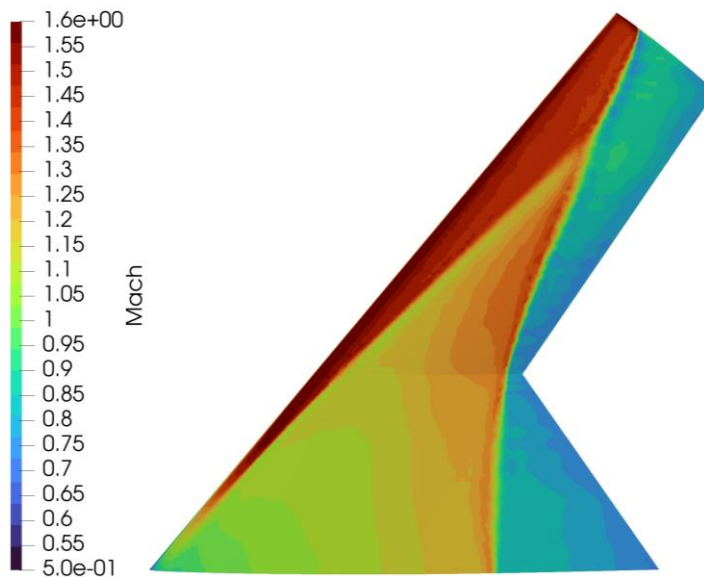


Figure 46 – NACA 65 Euler CFD analysis at $M_a = 0.85$ and 15,000 ft.

Adding also a properly designed wing cap allows to further improve the flow characteristics. Some tentative have been made resulting in the geometry shown in Figure 47. The new wing cap avoids the very high accelerations of the flow over the wing flat face, thus changing the shock behavior at the wing tip as can be seen in Figure 48. For such reason, as it can also be seen in Table 24 and Table 25, the wing cap improves the L/D at both flying conditions and so it will be included in the final design.

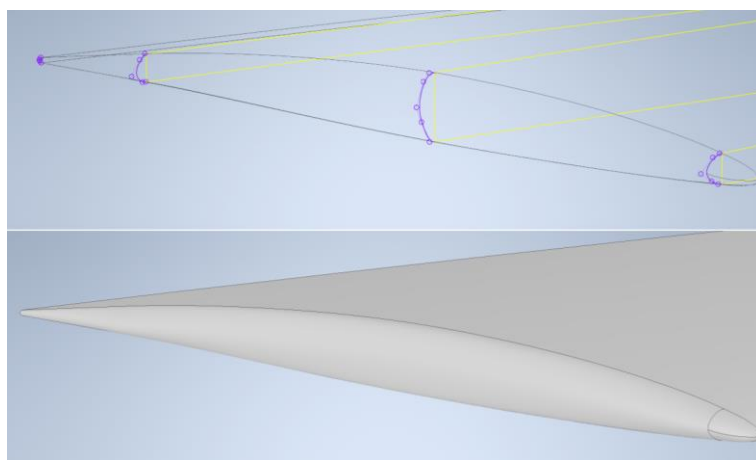


Figure 47 - Wing tip cap construction section and geometry.

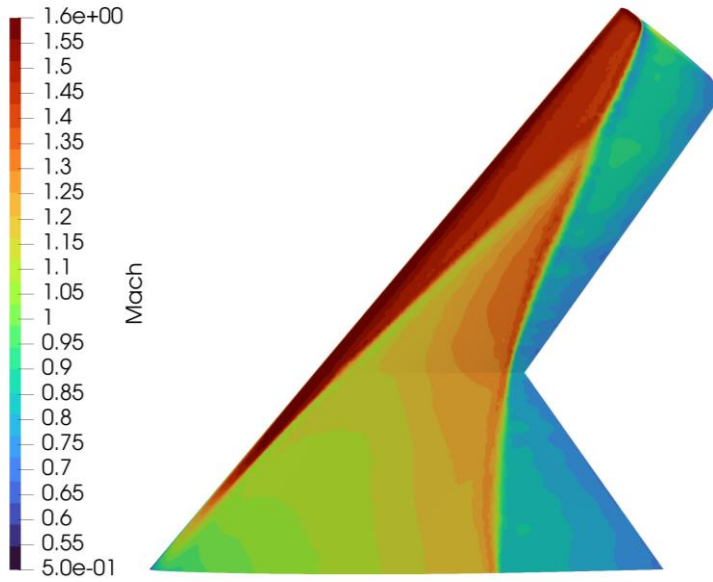


Figure 48 - NACA 65 with tip cap Euler CFD analysis at $M_a = 0.85$ and 15,000 ft.

	Without Tip Cap	With Tip Cap
C_L	0.342	0.341
C_D	0.01996	0.01946
L/D	17.12	17.52

Table 24 - NACA 65 Results at $M_a = 0.85$ and 15,000 ft.

	Without Tip Cap	With Tip Cap
C_L	0.179	0.174
C_D	0.00512	0.00480
L/D	34.94	36.18

Table 25 - NACA 65 Results at $M_a = 0.50$ and 15,000 ft.

It must be said that supercritical airfoils have also been tested in this phase (both Whitcomb and other custom airfoils), but the problem is that the database availability of this kind of airfoil is greatly reduced compared to NACA ones, thus not allowing to test every thickness ratio or curvature combination.

As previously shown, the Korn equation allows a higher thickness ratio for supercritical airfoils because they have a large leading edge radius and accelerate the flow in a smooth way, causing the shockwave to be delayed. So, for this reason, thicker airfoils were chosen at first: Table 26 illustrates the first case with supercritical airfoils, denoted as Case 4.

Wing Section	Case 4
Root	NACA SC(2)-0012
Mid	NACA SC(2)-0010
Pre-Tip	NACA SC(2)-0010
Tip	NACA SC(2)-0706

Table 26 - Case 4 airfoils configuration.

Knowing that the Korn equation is not necessarily respected for the wing in analysis, case 5 has been created with the aim of understanding if the behavior improves with a lower thickness ratio. Table 27 illustrates the airfoils used for this case.

Wing Section	Case 5
Root	KC-125-08
Mid	NASA SC(2)-0706
Pre-Tip	NASA SC(2)-0706
Tip	NASA SC(2)-0404

Table 27 - Case 5 airfoils configuration.

Finally, Ing. Giorgio Travostino from Piaggio Aerospace also provided a set of supercritical airfoils designed for a wing with a $M_{a_{DD}} = 0.92$. The wing designed with these airfoils is denoted as Case 6. But these airfoils have been designed for a very different aircraft class, thus they do not work well at high angles of attack. Nevertheless, they have been analyzed.

One more airfoil configuration was tested at last, whose idea is to try a mix between NACA airfoils and supercritical airfoils, hoping it could bring an improved flow behavior as supercritical airfoils do not provide a good one as shown in Table 29.

Wing Section	Case 7
Root	NACA SC(2)-0012
Mid	NACA SC(2)-0010
Pre-Tip	NACA SC(2)-0010
Tip	NACA 65A206

Table 28 - Case 7 airfoils configuration.

	Case 4	Case 5	Case 6	Case 7
C_L	0.319	0.433	0.490	0.323
C_D	0.0271	0.0391	0.0505	0.0266
L/D	11.77	11.08	9.70	9.73

Table 29 - Results for supercritical airfoils at $M_a = 0.85$.

Case 4 and Case 7 have been discarded right away as they provide a lower C_L than the NACA cases and a lower L/D . Case 5 and Case 6, instead, both provide a high lift, and they have both been analyzed at a lower angle of attack. Even at an angle of attack of 3°, the L/D is 14.3 for Case 5 and 16.1 for Case 6, which are both lower than case 3, thus the case with NACA 65 series is chosen as the final configuration.

7.2. RANS Analyses

It is now possible to compare the results obtained for the viscous simulations with the inviscid ones. Table 30 provides the aerodynamic results for the same baseline wing at $M_a = 0.85$ with Euler and RANS simulations. It is important to note that these simulations were done with an angle of attack of 5°, which is the benchmark angle of attack after the complete aircraft analysis explained in paragraph 7.1. Also, the number of cells chosen for this analysis is 4.5 million, as discussed in the RANS grid convergence presented in Appendix A.4.

	Inviscid	With Viscous Effects
C_L	0.278	0.247
C_D	0.0121	0.0140
L/D	22.98	17.64

Table 30 - Comparison between inviscid and viscous simulations for the wing at $M_a = 0.85$.

Viscous simulations provide a lower C_L and a higher C_D with respect to their inviscid counterpart, leading to a lower L/D . The cause of the higher C_D is mostly due to the introduction of shear stress given by viscosity, but the increase is limited because the viscous effects seem to decrease the pressure jump on the shockwaves (as it is possible to see from Figure 49). As for the reduction in C_L , Figure 49 clearly shows that the shockwave is slightly moved forward because of the viscous effects, as well as changing the behavior noticeably in the swept part of the wing; this subsequently leads to a reduction in the area with lower pressure, thus reducing C_L . The result is caused by the influence of the boundary layer; more precisely the boundary layer can be seen as an increase in airfoil thickness, and so it causes higher acceleration on the flow and an anticipated shockwave.

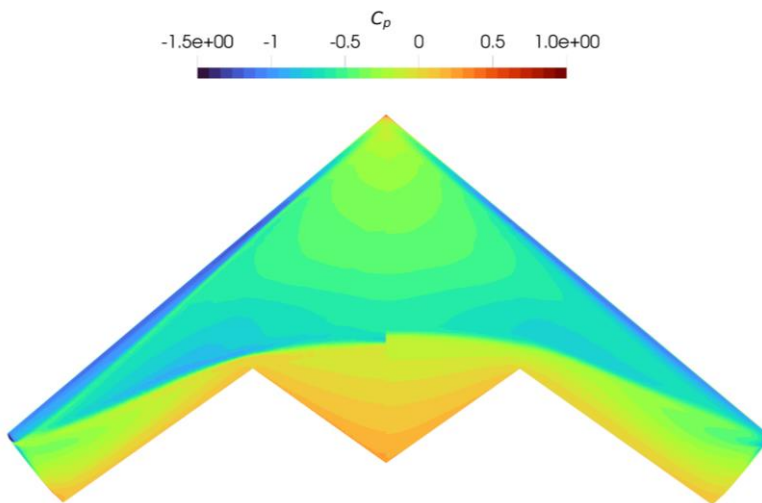


Figure 49 - C_p comparison between inviscid (left) and viscous (right) simulations.

8. Complete Aircraft Euler Analyses

Setup and results of Euler analyses on the complete aircraft is presented in this chapter as well as the related design iterations.

After having selected the airfoil and having done many considerations on higher order analyses on wings, Euler analyses of the entire full body have been performed as well, in order to understand the interactions between wing, fuselage and tail. This allows to verify if the fuselage design is satisfactory and leads to a generation of lift, as well as considering transonic effects on the tail and fuselage and looking at the difference in flow behavior on the wing. This is not extremely costly as many of the setup considerations made for the wing can be directly applied to the full aircraft.

For the complete aircraft, it was necessary to find a common angle of attack closer to the sustained turn requirement $C_L^{SUS} = 0.40$. Doing so required to reduce the angle of attack compared to the isolated wing case. For the loitering condition, the same angle of attack of the isolated wing has been considered. Furthermore, those angles have been fixed for every trial in order to still achieve a common reference between the configurations.

The selected reference conditions of the flow are reported in Table 19.

Flow Conditions	$M_a = 0.50$	$M_a = 0.85$
Pressure [Pa]	57182	57182
Temperature [K]	258.65	258.65
Density [kg/m^3]	0.7708	0.7708
Angle of Attack [°]	4.5	5.0

Table 31 – Complete Aircraft Flow Conditions.

A grid convergence analysis has also been done and it is shown in Appendix A.2. Due to the less streamlined body, the convergence resulted trickier but has been eventually reached. The number of cells used herein is 5.7 million cells.

8.1. Tail Fuselage Section Design

The greatest problems encountered in the Euler analyses of the full body are related to the tail section of the fuselage, more specifically by its connection with the main body and the engine. The initial tail geometry tested suffered from convergence problems as shown in Figure 50 (note the boundary condition at the nozzle was not respected). To try to overcome those problems, a modified geometry has been considered. This geometry consists in altering the fuselage around the nozzle in order to avoid convergence problems caused by extremely small volume elements and “wall” elements (so regions with the “wall” boundary condition) extremely close to the nozzle boundary. The geometry improved the convergence (which managed to reach a -5.5 *rms* value) but the results were not encouraging. The C_L and C_D still exhibit excessive oscillation, and their results were disappointing. The cause of this is related to the excessive region on which separation occurred.

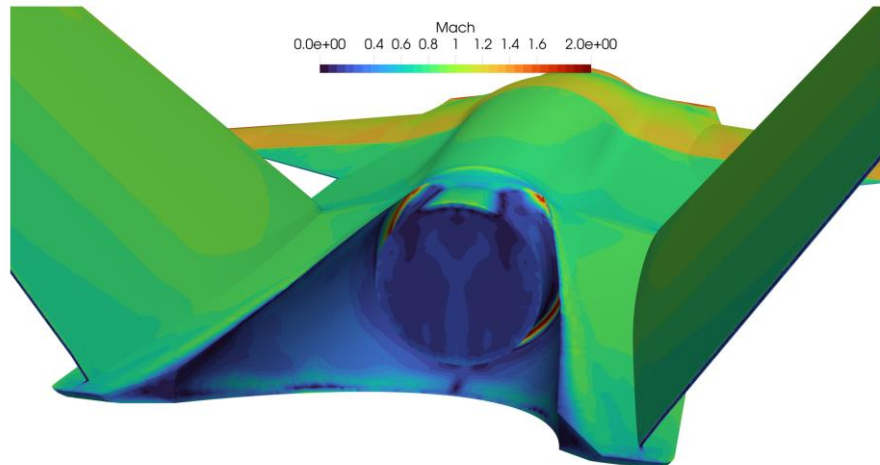


Figure 50 – Initial Tail Section Geometry

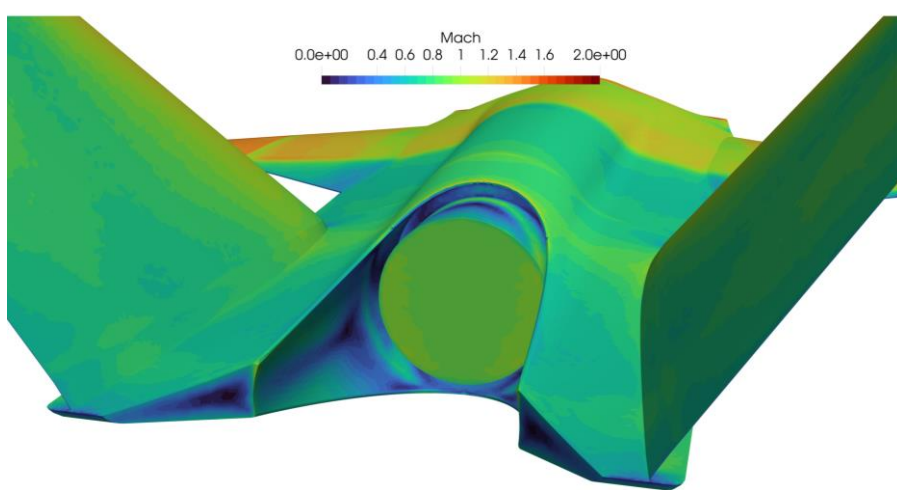


Figure 51 - Modified Tail Section Geometry.

With these results it has been decided to revise the tail section geometry. Many iterations were analyzed. The final configuration shown in Figure 52 was chosen since it was the solution less subjected to separation problems (as it can be seen by the number of regions with very small M_a values) and has less wetted area. Better solutions do exist, as discussed with Ing. Giorgio Travostino, but they are very complex to implement in a CAD model. Furthermore, to improve convergence the nozzle geometry and fuselage sections have been revised which allowed to realize a thinner overall section.

Lastly a slightly conical extrusion of 0.3 m was added to the nozzle as suggested by Prof. Barbara Re of Politecnico di Milano. This allow to place the boundary condition with enough distance to avoid numerical issues with the surrounding separated regions, as the boundary condition imposition in SU2 is not strong and is influenced by the near flow; so having a conical extrusion instead of a cylindrical one also allows the flow to expand “slightly” and not have numerical shockwaves (i.e. discontinuities).

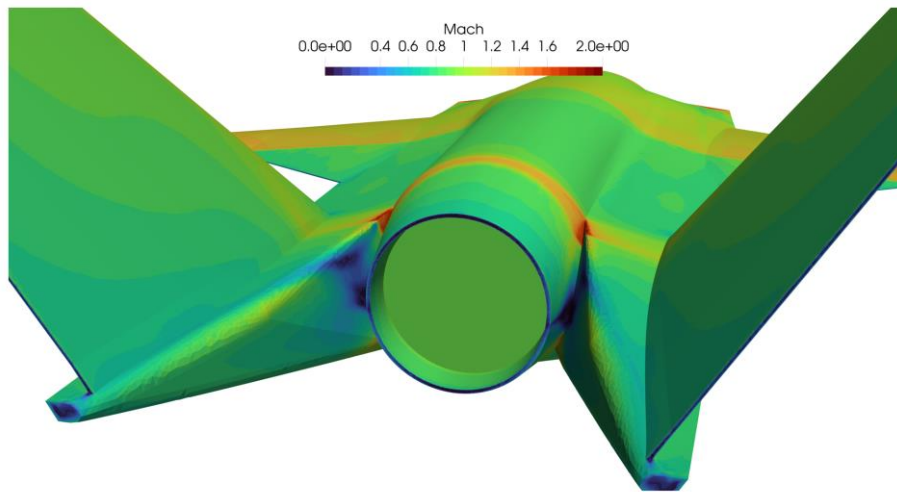


Figure 52 - Final Tail Section Geometry.

8.2. Tail Airfoil Selection

The full body analyses have been used also to select the final airfoil of the V-tail. Starting from the NACA 65A008 as shown in Chapter 4, some airfoils have been tested in order to avoid the formation shockwaves on the tail at the sustained turn condition ($M_a = 0.85$ at 15,000 ft). The solution has been found by lowering the overall thickness ratio of the tail by selecting a NACA 65A006 (Since as previously explained lowering the thickness improve the transonic behavior) and including a tip cap as it has been done for the wing in Chapter 7. In Figure 53 it is possible to see the results. The shockwave almost entirely vanishes with the new airfoils, leaving only a small supersonic region close to the tail tip.

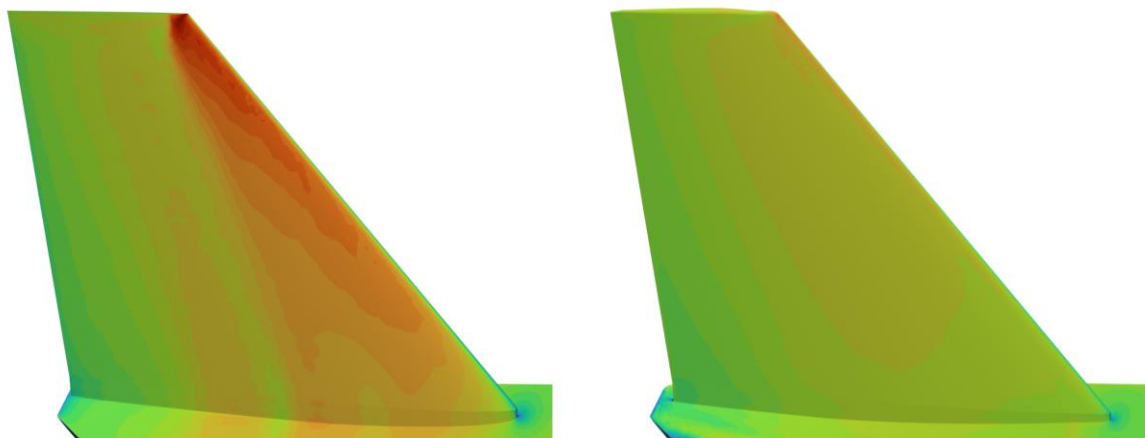
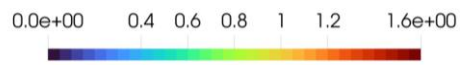
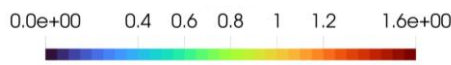


Figure 53 – V-tail initial (left) and final (right) tail configuration with Euler CFD.

9. LEX Design

The design of the leading edge extensions of the aircraft is presented here, with all the different considerations needed for higher order methods, as well as full body analyses.

The design of a leading edge extension is a very complex task that requires high incidence CFD analyses in order to correctly capture the vortex behavior. LEX are considered to improve the behavior of the aircraft at high angle of attack due to the formation of a vortex that interacts with the wing leading-edge vortex. The analysis on the LEX requires tools able to capture vortices: thus, the design and implementation is done using higher order methods with respect to a VLM.

It is possible to obtain a very approximate effect on the C_L by considering Figure 54. The figure shows an increment of lift coefficient ΔC_L^{LEX} about 0.4 (value also suggested by [1]). Since the trapezoidal wing is expected to behave as a typical fighter wing, $\Delta C_L^{LEX} = 0.40$ has been considered; instead, for a lambda wing configuration only 80% of the increase has been considered, obtaining $\Delta C_L^{LEX} = 0.32$ since said wing planform is not conventional and conservativeness is preferable.

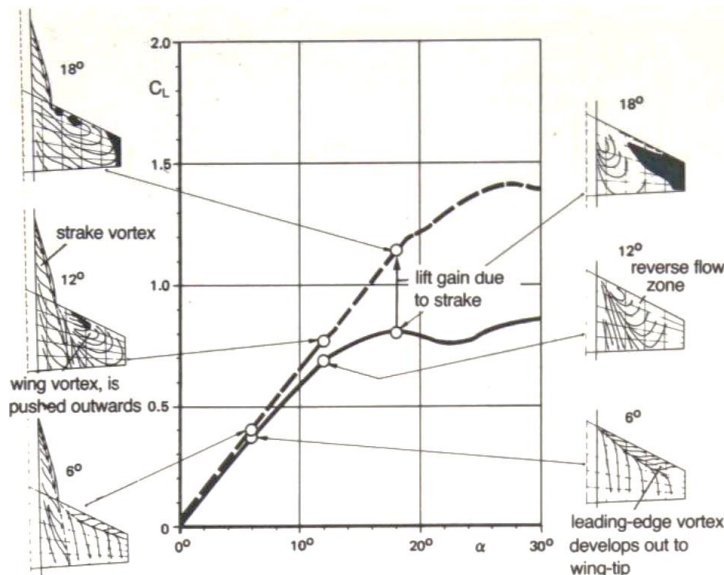


Figure 54 - LEX influence on the $C_{L_{max}}$ [4].

The LEX also has significant destabilizing effects on the pitch moment and influence on the wing vortices: these effects need to be considered in stability analyses with significantly more complex aerodynamic methods.

To try to size these surfaces at a preliminary level the problem has been studied at first with mid-fidelity method: DUST. After selecting some promising LEX configurations, these have been studied with higher order methods like Euler analyses of the entire body in sustained turn condition ($M_a = 0.85$ at 15,000 ft and $\alpha = 5^\circ$) and RANS analyses of only an isolated part of the wing at higher incidence. After these verifications, the final LEX configuration has been chosen.

9.1. LEX First Sizing

Exploiting the quickness and good reliability of DUST in subsonic regime, a first sizing of the LEX surface has been done to define which is the best shape in terms of root chord and LE sweep. Each geometry iteration has been tested at 4 different angles of attack ($0^\circ, 5^\circ, 10^\circ, 15^\circ$) in the same free stream condition ($M_a = 0.85$, $h = 15,000$ ft). Each simulation has been run until the integral loads of the aerodynamic surfaces converge to a constant value utilizing the time step,

mesh refinement, gap between bodies and domain length retrieved during the sensitivity analysis previously executed in section 6.7.

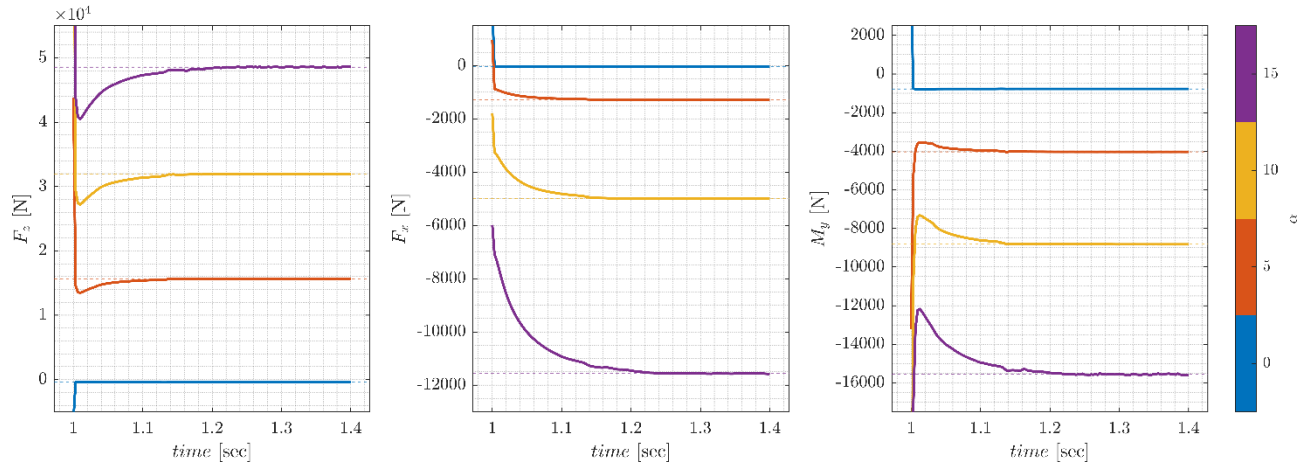


Figure 55 – Example of integral loads convergence for LEX configuration

As can be seen from the Figure 55, the integral loads don't perfectly converge at 15° , instead they have an oscillatory behavior. This is because at high angles of attack the wake shedded by the wing and the LEX has a hard interaction with the tail surface. As may be seen from the animated 3D visualization obtained by DUST_post, the generation of an oscillatory behavior of the aircraft wake isn't present at lower angle of attack, explaining the behavior of the integral loads.

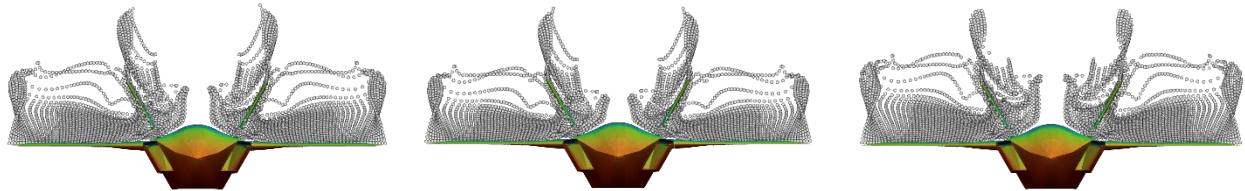


Figure 56 – wake envelope at $M_a = 0.30$, $h = 15,000\text{ft}$ and $\alpha = 15^\circ$

The two variables considered for the first sizing have been analyzed separately with two different sets of runs. In the first set the effect of different length of the root chord has been tested by keeping the LE sweep angle fixed at 70° while in the second set the effect of the LE sweep angle has been studied by keeping the root chord fixed at the best length found during the previous runs.

It's important to keep in mind that all the numerical results obtained in the LEX design will underestimate the real lift, drag and momentum generated. This is because over $\alpha = 10^\circ$ the total lift of high LE-sweep aerodynamic surface is the result of the sum of two contributes: the potential lift, well modelled by DUST, and the vortex lift, not considered by DUST. By increasing even more, the AOA the vortex lift drastically change the total lift value becoming the predominant component as can be seen in Figure 57.

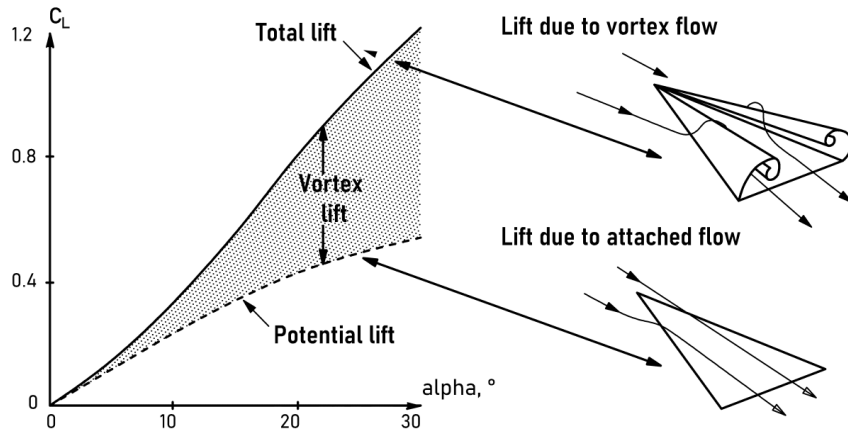


Figure 57 -Vortex lift of a slender delta wing [24].

The vortex lift is the physical phenomenon on which LEX and Delta wings mainly rely on and is well explained in [25].

9.2. Root Chord Analysis

As explained before the first set of run consists in analyzing the effects of different root chord length on the LEX. To easily find the input data for the parametric builder of DUST_pre a 2D sketch on FreeCAD has been created. In this model all the constraints that the LEX surface geometry must have with the fuselage and the wing (parallel root chord and TE sweep equal to LE sweep of the wing) are fixed and just by changing the root chord length value all the other quotes on the part updates automatically and can be written in the ".in" file used by DUST.

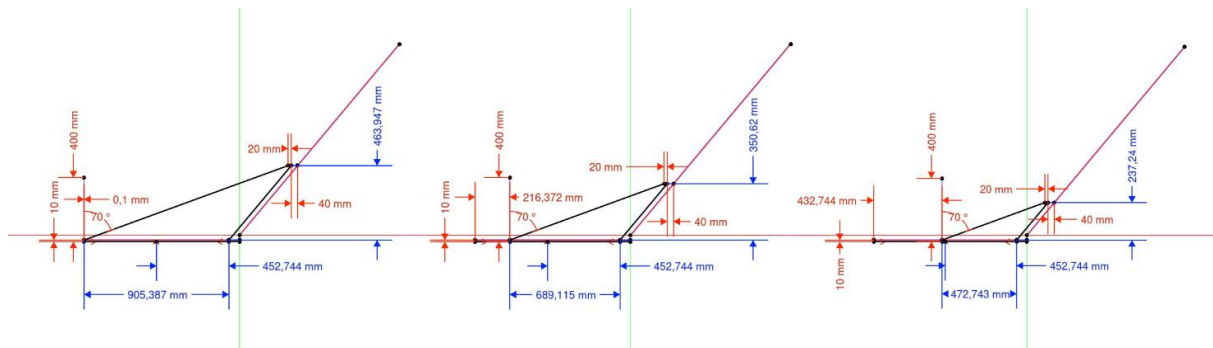


Figure 58 – LEX 2D sketch on FreeCAD for chord analysis

Once all the three models have been correctly modelled, a parametric run has been executed to verify how the three different geometries perform at different angles of attack. The result in terms of integral loads have been reported in Figure 59. The data retrieved from the simulations has been post-processed to understand better the impact in terms of C_L , C_D and C_M that the presence of the LEX have. For this reason, the plots report a value of ΔC_i which has been computed by doing a difference between C_i^{LEX} and $C_i^{NO\ LEX}$.

Since DUST compute only the induced drag an estimation of friction drag of the different geometries has been done by means of a semi-empirical approach taken from [1], and added to the drag induced component.

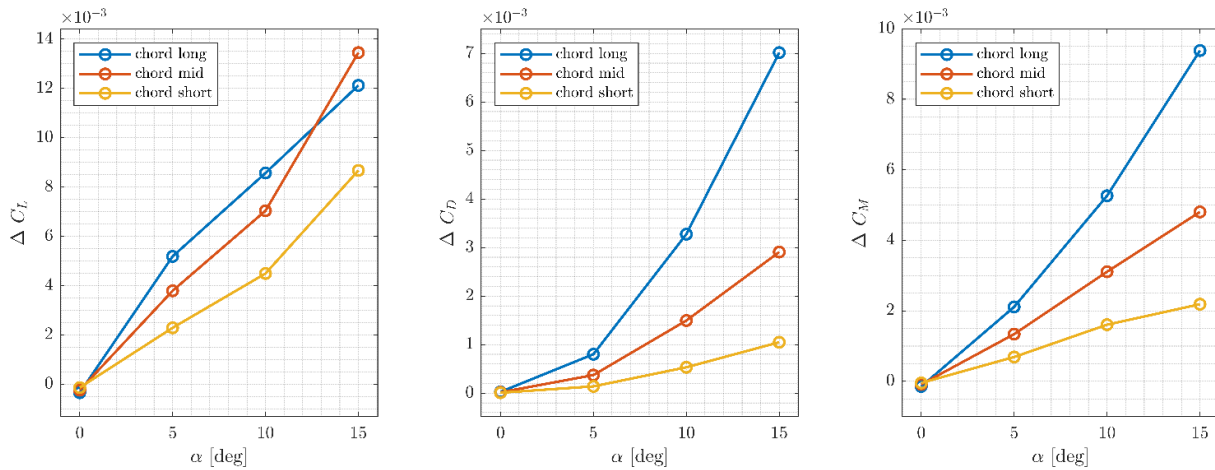


Figure 59 – Effect of different LEX root chord length on aerodynamic coefficients

As expected, the best geometry is the one with the longest chord length. This solution allows a good increase in C_L and C_M . The price to pay is an increase in C_D as well, caused by the additional lift and the friction drag bigger than the other geometry because of the bigger wet surface.

Must be noticed that the mid chord solution (middle picture in Figure 59) seems to perform better than the long chord one at high angle of attack. Anyway, as has been proven before, in section 6.6, DUST can't give good and precise results at $\alpha > 10^\circ$.

9.3. Leading Edge Sweep Analysis

Once the root chord has been decided the focus has shifted to the LE sweep angle of the LEX. Three different configurations have been tested using the same procedure as before.

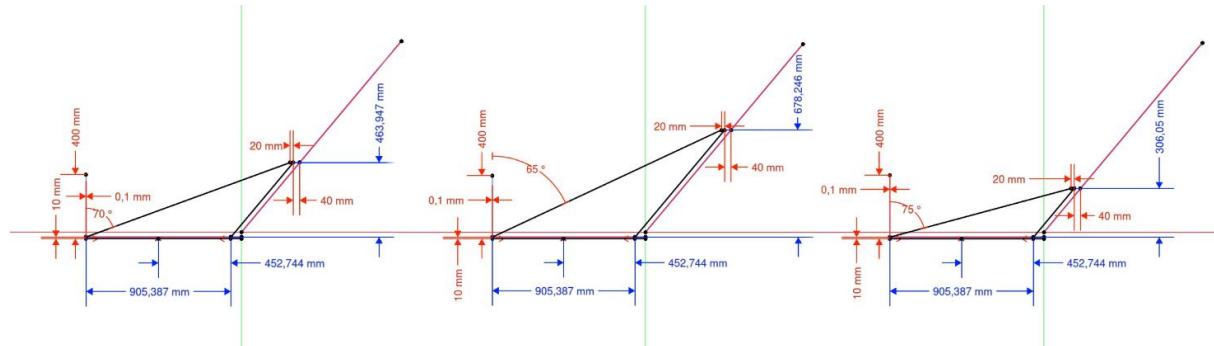


Figure 60 – LEX 2D sketch on FreeCAD for sweep analysis.

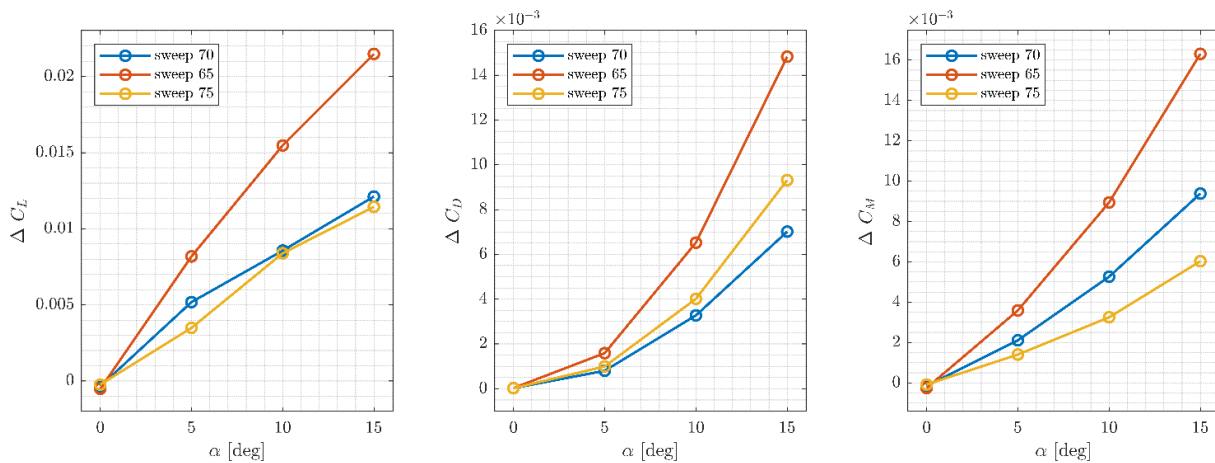


Figure 61 – Effect of different LEX LE sweep on aerodynamic coefficients.

As expected, the best geometry is the one with the smallest LE sweep. This solution allows a good increase in C_L and C_m . The price to pay is an increase in C_D as well, caused by the additional lift and the friction drag bigger than the other geometry because of the bigger wet surface.

Must be noticed that the LEX geometry with LE sweep equal to 70° seems to perform pretty good too. It has the big advantage of generating a reasonable amount of additional lift and momentum with a very small impact on the drag (once again considered as the sum of induced drag and friction drag computed with semi-empirical formulas).

By considering these two parametric analyses the two best LEX designs are both with the longest root chord length. The two best LE sweep angle are 70° and 65°. In the following phase of LEX design these two solutions will be drawn in the 3D cad model and using SU2 will be done a more in-depth analysis. In particular will be important to verify that even in transonic condition these designs will perform well as explained before in section 6.6, these preliminary analyses have been executed in subsonic regime due to the fact that DUST can't model complex compressibility effects.

9.4. LEX Interaction with Air Intake.

During the development of the geometry, challenges were faced in designing the air intake to ensure it compatibility with a LEX. Starting from a simple geometry used in previous phases, two main configurations were developed. The 'indented' geometry was discarded upon discovering that it would need to handle a significant shockwave at the entrance. This particular condition would necessitate a dedicated and advanced design phase beyond the current project's scope, as it documented in [26] where a complete air intake study is carried out. The correct geometry for these kind of analyses on a fighter aircraft requires the entire internal modelling from the intake to the compressor and from the turbine to the nozzle exit, as it is shown in the following figure:

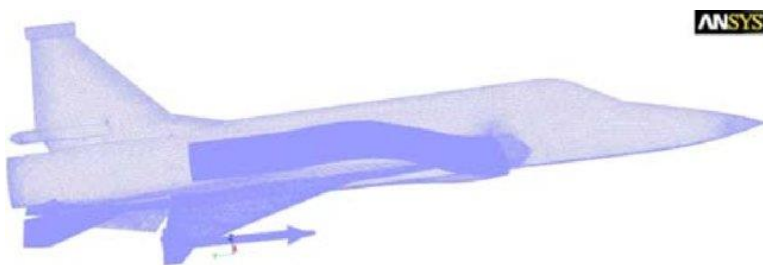


Figure 62 - Fighter intake modeling from [26].

Consequently, the 'closed' configuration was preferred at this preliminary level mainly due to computational limitations. By positioning a plane at the entrance of the air intake, the outlet condition can be imposed on the surface, allowing us to proceed with investigating the effects of the LEX on the aircraft without the complexities of shockwave management.

Retaining significant a visual comparison between the two possible designs, some images that offer interesting insights are presented. Those analyses, shown in Figure 63 have been performed with the 70° LEX configuration but the same conclusions are applicable to the 65° configuration here not presented.

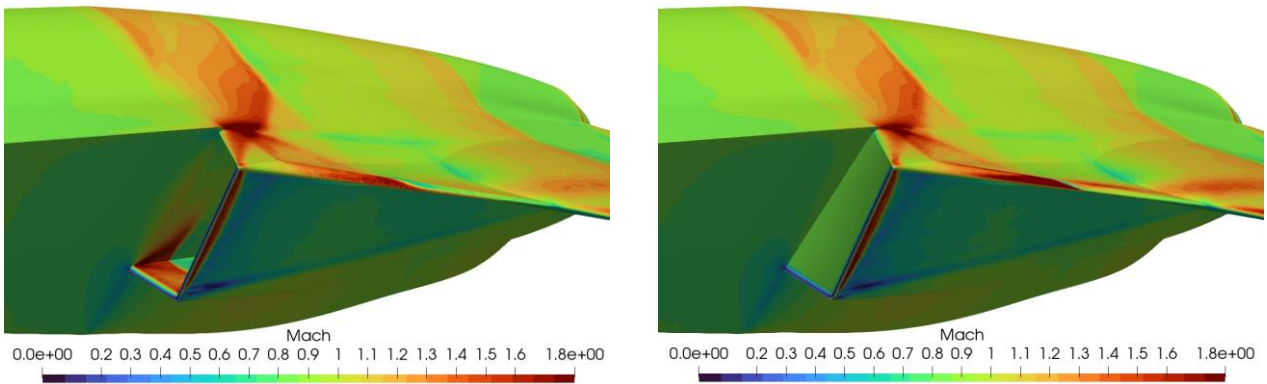


Figure 63 - Comparison between the air intake designs.

No significant differences are observed in the visual outputs from the two simulations. It must be specified that the left simulation fails to achieve a solid RMS convergence, which is the explanation of minor differences in the flow field. The real trade-off with the right configuration is the loss of the full effect of the vortex generated from the upper part of the air intake and its associated effects. Nevertheless, this option is less problematic than managing the shockwave, as mentioned earlier.

9.5. LEX Design Verification and Comparison

The outcomes obtained from the analysis of several LEX designs using *DUST*, as mentioned before, provides sufficient information to choose the two best solutions considered and analyse them further using Euler and RANS CFD analyses. The two candidates are the ones with a sweep angle of 65° and 70° . Once the CAD models have been upgraded with the implementation of the LEX between the air intake and the wing leading edge, they can be meshed and used to perform two runs at Mach 0.85 and 5° angle of attack. This flight configuration ensures the right conditions for vortices to develop over the surfaces of the new wings and furthermore it represents a standard one used in other phases of the study. It is expected that the LEX effects are more significant over the wing, leading to an increase in the lift produced. Nevertheless, since the main interests are the overall consequences on the aircraft, the considerations on the C_L and C_D of the full aircraft still stand. The following table reports the resultant lift and drag coefficients so that they can be compared in order to choose the most suitable one for our project needs:

	LEX 65°	LEX 70°
C_L	0.381	0.389
C_D	0.02570	0.02702
L/D	14.82	14.40

Table 32 - Comparison between the two designs.

The LEX at 70° is chosen to continue with the following phases of the project since it is able to provide more lift (by giving a 5.13% increase) while providing a small contribution of drag (with a 2.18%). Note that the values obtained are just to give a reference of the order of magnitude in change of the coefficients.

During the post process phase, looking at the flow streamlines, it may be confirmed that vortices are really generated from the LEX. Their behavior will be deeply investigated in a succeeding section where a 3D visualization will allow us to make more in-depth considerations.

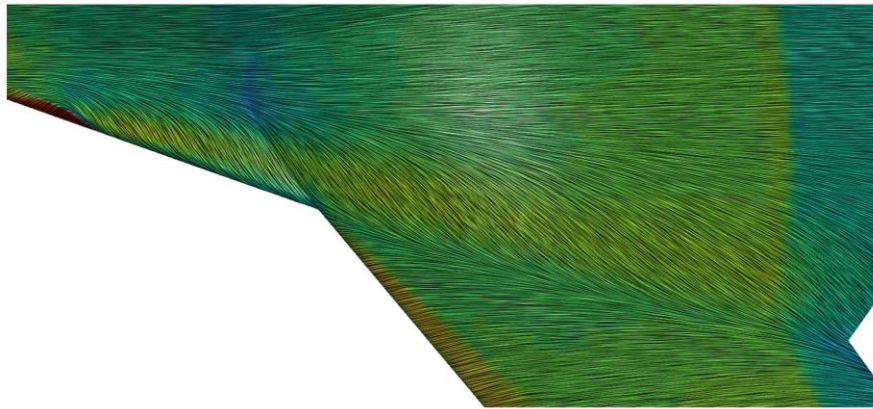


Figure 64 - Zoom in on the vortex's streamlines.

Despite the choice of the lex at 70° being based on coefficients values, some qualitative considerations can still be taken into account. Passing to the visualization of the *Mach* over the surface, vortices can still be detected as a localized increment of velocity. The most significant difference between the two configurations is the direction of the vortices: as expected they tend to align to the sweep angle of the LEX and for this reason they reach the trailing edge of the wing at two different spans.

In addition, from the following images, the reason behind the increments of the lift and drag coefficients can be explained. The speed seems to be greater at different points, which results in an increased C_L , but also causes the shockwaves to be slightly stronger, producing a higher C_D .

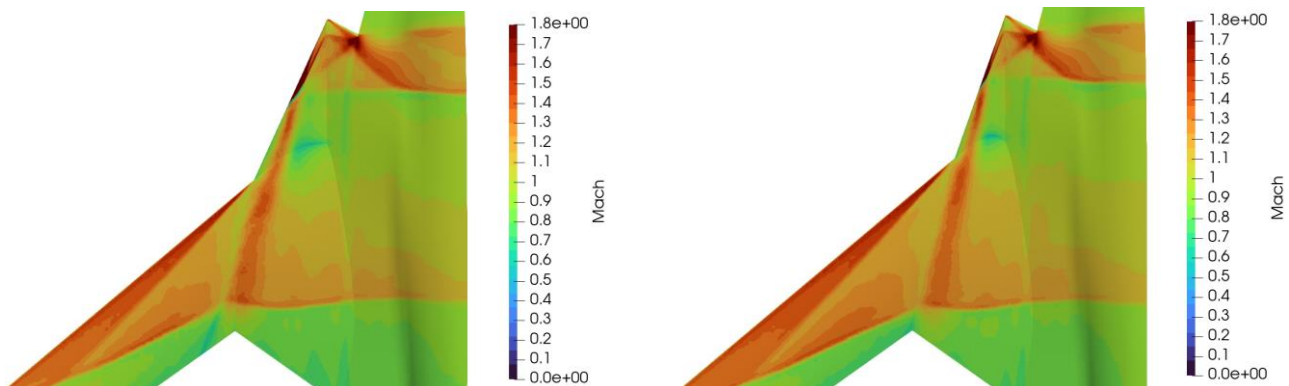


Figure 65 - On the left LEX 65°, on the right LEX 70°.

The final consideration that makes the LEX with 70° of sweep more effective is the fact that by directing the vortex at the intersection between the trapezoidal and swept parts of the wing, it minimizes the negative effects caused by the vortex disturbing the aerodynamics of the swept part, as it occurs with the LEX at 65° .

It is possible to visualize the streamline's behavior in certain zones of the aircraft to better understand, in an approximate way, how the flow behaves. The following figures provide the streamlines for the LEX geometry with 70° of sweep at three angles of attack: 5° , 7° , and 10° .

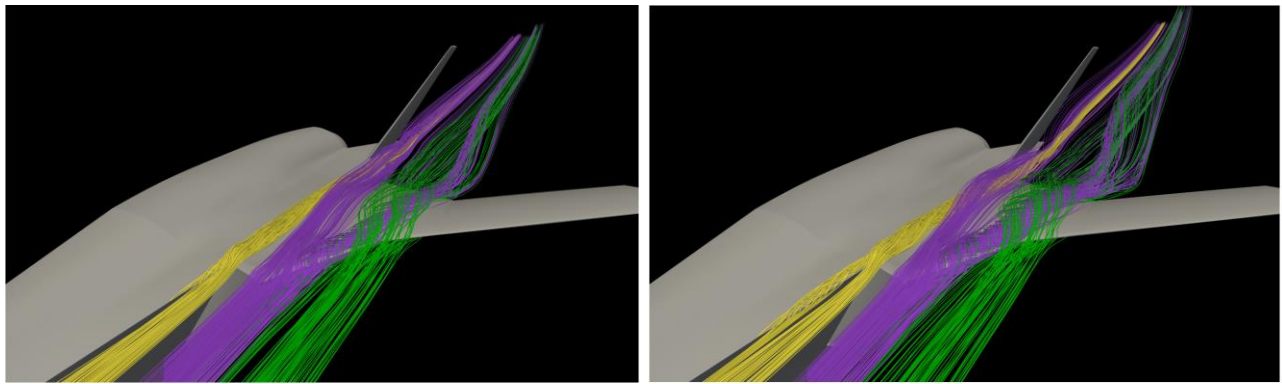


Figure 66 - Flow streamlines close to the LEX for $\alpha = 5^\circ$ (left) and $\alpha = 7^\circ$ (right).

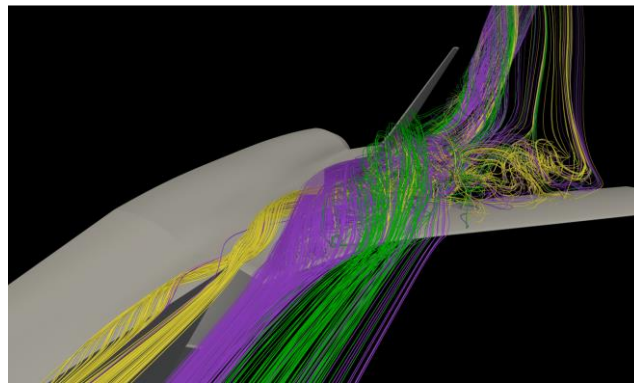


Figure 67 - Flow streamlines close to the LEX for $\alpha = 10^\circ$

Although said streamlines are not precisely computed and are not exempt from approximations, they are able to provide an idea of the flow's behavior. As Figure 66 shows, the flow is characterized by three "Eulerian" vortices, which are vortices that are a good approximate of viscous vortices but computed with Euler equation. The three vortices are: a vortex that is generated partially by the nose acting as a strake as well as the air intake, a second vortex that is generated by the LEX itself (which is the most intense one), and a third vortex generated by the meeting point between the LEX and the wing. The vortices seem to pass "externally" with respect to the tail, which is positive for the tail's aerodynamics. Also, the two vortices on the right interact with each other to create a more intense single vortex. It is possible to see how the global effect is more intense when a higher angle of attack is considered, but up to a limitation. In Figure 67 is shown the flow over the aircraft at 10° of angle of attack, this behavior is not meant to show any precise physical phenomena, but it is meant to show that a non-viscous method doesn't allow to analyze the high angle of attack effect of the LEX. For this reason, the analysis is followed by a viscous simulation, presented in 9.6.

Finally, Figure 68, Figure 69 and Figure 70 show the distribution of the shockwaves at the sustained turn flying condition, showing the global mutual interaction of the different parts of the aircraft.

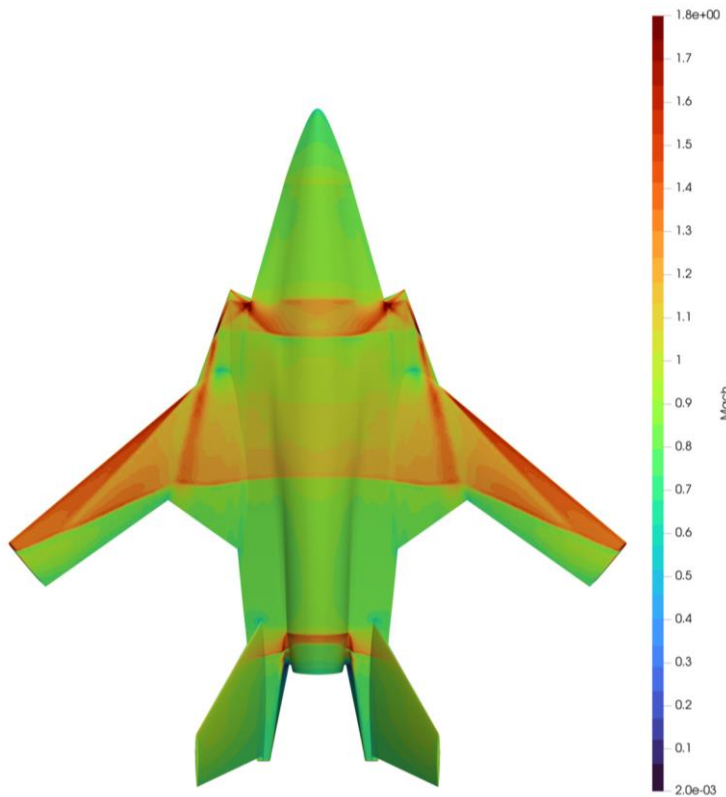


Figure 68 - Final Configuration Euler Results Top View ($M_a = 0.85$ at 15,000 ft).

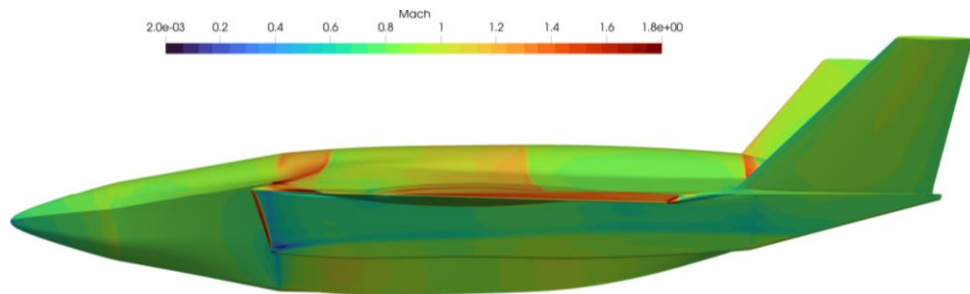


Figure 69 - Final Configuration Euler Results Side View ($M_a = 0.85$ at 15,000 ft).

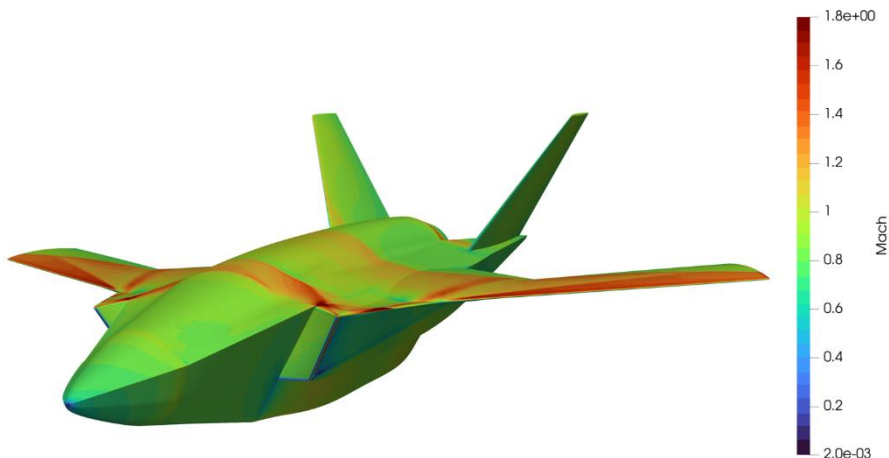


Figure 70 - Final Configuration Euler Results Iso View ($M_a = 0.85$ at 15,000 ft).

The results in terms of coefficients are presented in the following table:

$M_a = 0.85$	
C_L	0.389
C_D	0.02702
L/D	14.39

Table 33 - Final Configuration Results for the Design Condition.

9.6. Rans Problem Setup

For a deeper aerodynamic analysis of the LEX design, a Reynolds-Averaged Navier-Stokes (RANS) simulation setup was employed. The RANS method, which has already been extensively shown in section 6.4, was set up in a similar way. The strong flow interaction of the intake with the wing must be considered, reason why it was included a section of the fuselage in the model to be meshed: this inclusion is crucial as the fuselage significantly influences the flow characteristics near the wing root, where the LEX is most effective in this way. Nevertheless, the physics of the problem is not completely correct, being the symmetry constraint an artificial one, the simulation domain stays within the limit of a laptop computational power; on the other hand, this simplification does not properly affect the LEX studies.

The primary motivation for the chosen geometry was to maximize the aerodynamic benefits. The geometry of the LEX was optimized through iterative DUST simulations, ensuring that the wake released by the LEX does not disrupt the performance of the aircraft. Additionally, the presence of the fuselage helps to realistically simulate the aircraft's operational environment, providing more accurate predictions of aerodynamic performance.

The effectiveness of the LEX is demonstrated by comparing the flow characteristics over different regions of the wing. In the outer region of the wing, where the vortices produced by the LEX do not act, flow separation and stall were observed in Figure 71. This region exhibited high angles of attack beyond the stall angle, resulting in a loss of lift and increased drag. Conversely, in the region where the LEX operates, the vortices generated by the LEX were effective in delaying flow separation as shown in Figure 72. This resulted in sustained lift and prevented stall, indicating that the LEX performs its intended function. The comparison of these two regions clearly shows the LEX's role in enhancing the aerodynamic performance of the wing by maintaining flow attachment in critical areas.

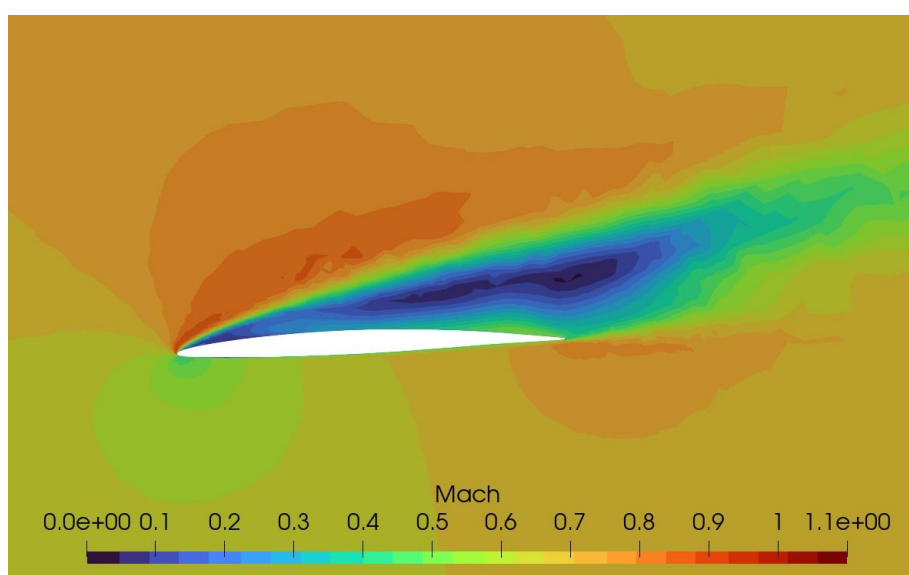


Figure 71 - Section of the wing near the tip.

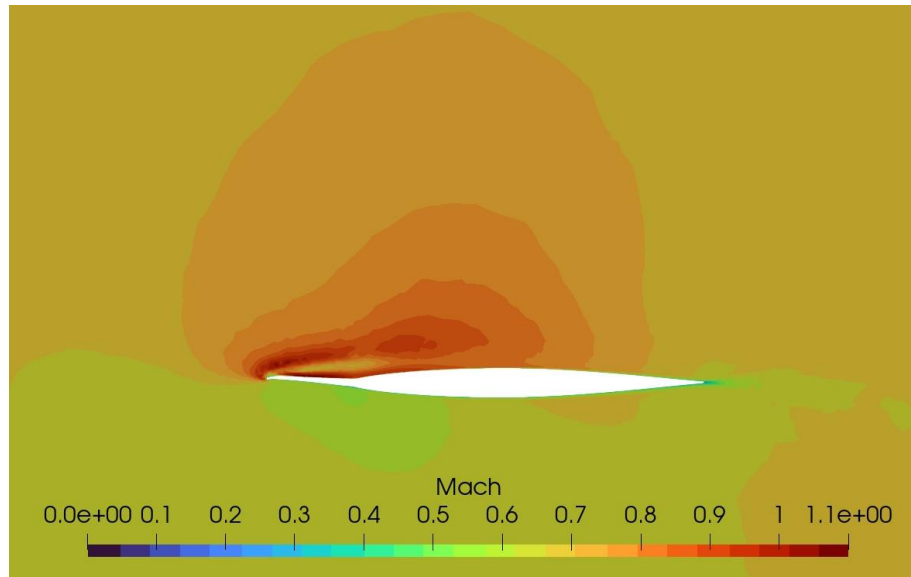


Figure 72 - Section of the lex and the wing.

Concluding the part of the RANS analyses, it is noteworthy to make a disclaimer. At 10° of incidence, most of the model is stalled, so during meshing, elements should be concentrated in the volume from the trailing edge till a distance where the wake effects want to be captured.

With the objective of capturing if the LEX behaves as expected, not much importance has been actually paid in capturing the behaviour of the wake. This approach is necessary due to the high cell limitation, explained in the RANS grid convergence analysis (presented in Appendix A.4) for the isolated wing. Obviously, with the addition of a body, the situation becomes even worse. Considering this trade off, the wake is not properly caught but we retain that Figure 71 and Figure 72 have highlighted in any case what was important for this phase of the study.

Despite its advantages, the LEX design is not without challenges and limitations. One of the primary concerns is the potential for increased drag under certain flight conditions, particularly at lower angles of attack where the vortices may not contribute positively to aerodynamic performance. This effect must be evaluated during the detailed engineering phase, always keeping in mind the main reason of their deployment, thus the compromises that could be made to reach the goal.

10. Adjoint Optimization

Finally, the process of the optimization of the wing through an adjoint method is proposed, as well as more results deriving from the optimization.

In the field of computational fluid dynamics (CFD), the optimization process is a powerful tool to improve the aerodynamic performance of a lifting surface, because of the high sensitivity of the aerodynamic coefficients with the shape of the body. One of the most powerful and efficient techniques for achieving optimization goals is the adjoint method. This method is particularly valuable due to its ability to handle high-dimensional design spaces, making it ideal for complex fluid dynamics problems. The adjoint method is particularly useful in CFD problems because of the efficiency in computing the gradients: during the optimization process of a design, it is often necessary to understand how small variations of the design variables (DVs) are affecting an objective function (e.g. drag or lift). The DVs are the control parameters of the functions that determine the shape of the body. Originally, the gradients of interest were calculated using the finite difference method, which is the simplest, but the computational cost was prohibitive. With the continuous adjoint method, which was introduced by Jameson in the 1980s [27], shape optimization becomes computationally affordable and attractive also for complex fluid dynamics problems.

Later on, the implicit gradient approach, also called the discrete adjoint method, has been developed from the discrete formulation of the flow equations [28].

10.1. Adjoint Optimization Method on SU2

SU2 contains multiple implementations of the adjoint methodology with supporting tools for design all within the same codebase, including a continuous adjoint and a discrete adjoint constructed via algorithmic differentiation of the code, the latter is the one used for this work, since it ensures numerical consistency with the discretized problem, providing also more accurate results in the gradient calculations.

The optimization chain is performed by separated C++ modules driven by the Python script `shape_optimization.py`. Each C++ module reads its part of interest of the configuration file and gives certain outputs, including `.dat` files where the state is written and `.vtu` files, allowing to visualize the results. The inputs of the optimization chain are the baseline initial mesh, the design variables, the objective function, and the constraint functions. In SU2 a Free-Form-Deformation (FFD) strategy has been used. The FFD can be approximated as a deformable plastic box, which is built around the model of interest. The DVs are defined in this box.

The main C++ modules used are listed below:

- **SU2_DEF (Mesh Deformation Code):** Computes the geometrical deformation of an aerodynamic surface and the surrounding volumetric grid, given the displacement of the design variables.
- **SU2_GEO (Geometry Definition Code):** Computes the geometric characteristics of the aerodynamic surfaces to use them as constraints during the optimization process.
- **SU2_CFD (Computational Fluid Dynamics Code):** Performs direct and adjoint simulations, by using Finite Volume Method and an edge-based structure.
- **SU2_DOT (Gradient Projection Analysis):** Computes the partial derivates of a function with respect to variations of the aerodynamic surface. This can be done by projecting the surface sensitivity into the design space through a dot product.

Lastly, the goal of the optimization process is to find a solution of the minimization problem of the objective function. A relevant problem for the algorithm is to understand if the solution found is a local or global minimum. In SU2 the optimization is handled by the SciPy's SLSQP (Sequential Least SQuare Programming) algorithm, which belongs to the family of algorithms called

Sequential Quadratic Programming (SQP). The SQP method has shown good performance when dealing with nonlinear programs, especially when a high level of nonlinearity is present, which is typical of aeronautical shape optimization problems.

10.2. Isolated Wing Optimization

The discrete adjoint method has been applied for the drag minimization problem of the isolated wing at $M_a = 0.85$, $h = 15,000 \text{ ft}$, lift coefficient fixed at 0.346. The angle of attack is set as a design variable; hence it can be changed during the iterations, in order to satisfy the requirement on the lift coefficient. Due to the high computational cost of the optimization design process, it was not possible to consider the wing-body configuration, which would have yielded more significant results, allowing for considerations about the interaction between the two structures and the attachment of the wing to the fuselage, which is a particularly critical region.

The mesh generated for this problem has 1.3×10^6 cells, due to the computational cost of the adjoint optimization process the mesh has not been refined more. Because of the unique shape of the STAD-1 lambda wing, two FFD boxes are required to capture correctly its geometry and impose the constraints. The wing is parametrized with 216 control points, with the request of continuity in the 1st derivative of the surface, impeding jumps or kinks in the deformed geometry. The design variables are all the control points, distributed on the upper and lower surfaces. The position of the control points and the FFD boxes are shown in Figure 73.

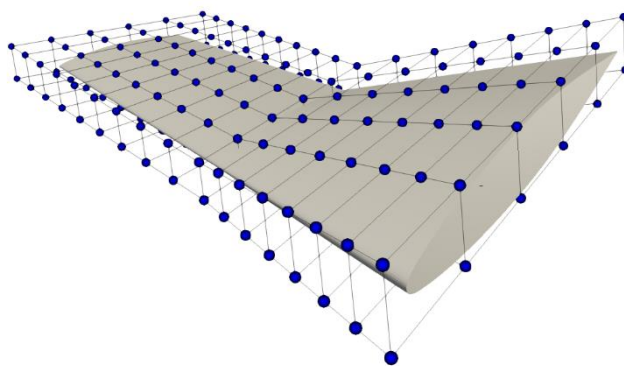


Figure 73 – FFD boxes and control points.

A feasible and reasonable surface can be obtained by imposing a sufficient number of constraints. First, the displacement of the design variables is allowed only in the z direction; it is also necessary to enforce constraints on the thickness, which are imposed on 5 sections along the span. The constraint based on the twist angle can't be applied directly, since SU2 does not consider the effect of the sweep angle when computing the geometrical characteristics of the wing. To restrict the variation of the twist angle of the wing, the position of the design variables associated with both the leading edge and the trailing edge has been fixed. However, it is important to remember that in the context of adjoint optimization, constraints are often treated as soft constraints rather than hard constraints. A hard constraint imposes a strict boundary that the solution must adhere to, whereas a soft constraint allows for some flexibility. The utilization of soft constraints balances the need for computational efficiency, smooth convergence, and the ability to explore innovative design solutions, ultimately leading to optimized aerodynamic performance while maintaining feasible design parameters. Hence a small variation of the twist angle can be expected. The optimization problem is summarized in Table 11.

Objective Function	Number of variables	Bounds
$C_D [-]$	1	-
Design variables	Number of variables	Bounds
shape	214	-
$\alpha [^\circ]$	1	[2 : 9]
Constraints	Number of variables	Bounds
$TOC_{trapezoidal}$	2	0.06
TOC_{swept}	3	0.04
Leading Edge	36	= 0 m
Trailing Edge	36	= 0 m

Table 34 - Summary of the STAD-1 wing optimization problem.

10.3. Results

The convergence history of the drag coefficient, hence the objective function, is shown below in Figure 74.

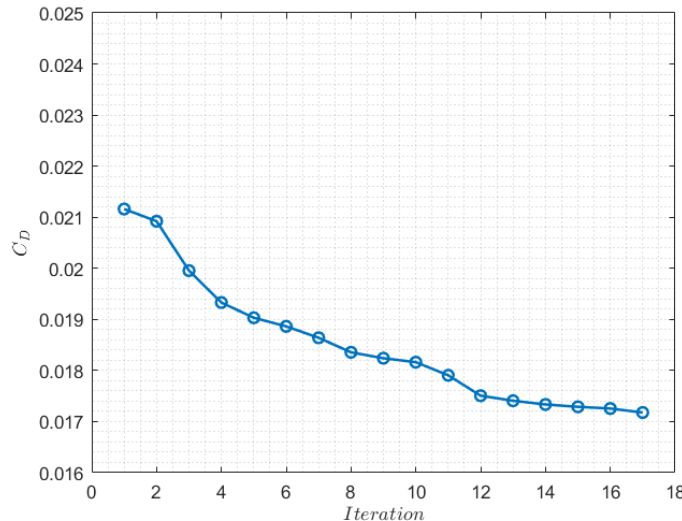


Figure 74 - Convergence history of the objective function.

	$C_L [-]$	C_D (counts)	AOA [°]
Baseline	0.346	211	6.00
Optimized	0.346	173	5.74

Table 35 - Results of the optimization process.

The simulation reached convergence after 17 iterations. At the last design iteration, the drag coefficient is 18.87% lower than the original one, passing from 212 to 173 drag counts. The angle of attack ranges from 6° to 5.734°, to comply with the requirement on the lift coefficient. The Mach number and pressure coefficient contours over the initial wing configuration (left) and over the optimal one (right) are shown in Figure 75. The Mach number distribution provides an insight into the flow characteristics and regions of potential shock formation. In the pre-optimization Mach contours (figure on the left) regions with higher Mach numbers (up to 1.4) near the leading edge and wingtips indicate the presence of transonic flow and potential shock waves that

contribute to the increase in drag. On the optimal wing the Mach contours show a more uniform distribution with a lower value of the peak Mach number. The areas of high Mach numbers are reduced, and the shock wave is less pronounced. Moreover, also the shape of the shock changed, after the optimization the shock wave is almost normal to the flow direction over the wing. From the C_p contours, the baseline solution exhibits clearly the well-known lambda shock pattern. After the optimization, it is possible to notice a significant reduction in the peaks of the pressure coefficient, indicating a decrease in the strength and extent of the shock wave.

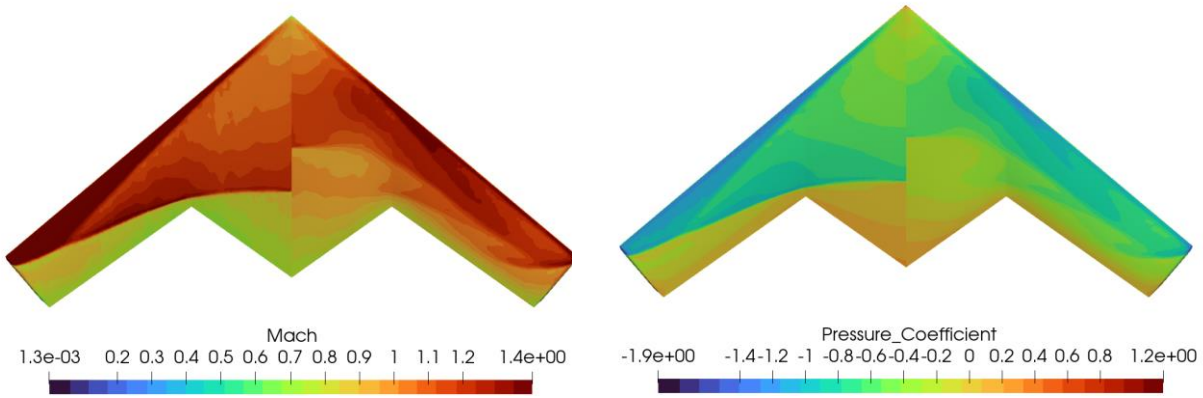


Figure 75 - Mach number (left picture) and pressure coefficient over the wing (right picture) before and after the optimization process.

Note: the left side of the picture is before the optimization while the right side is after the optimization.

The optimization process reduced the thickness of the wing, the radius of the leading edge has been reduced and this led to a decrease in the peak of the C_p . A small variation of the twist has been included as well. At the wing root position, shown in Figure 76, the airfoil shape did not change, because of the constraints applied, but the shock wave is clearly reduced in the extent over the chord. In Figure 77, Figure 78 and Figure 79, the sectional airfoil shape and pressure distribution are presented at different spanwise locations. In the baseline configuration at $y/b = 0.6$ (Figure 78), the formation of the lambda shock is visible from the pressure coefficient plot, where a second peak can be identified, and which is associated with a second compression in the flow. In the optimized configuration, the sharp jumps in the C_p plot have been smoothed out, indicating a significant alteration in the flow behavior. The absence of two distinct peaks suggests that the lambda shock has been effectively mitigated through the optimization process.

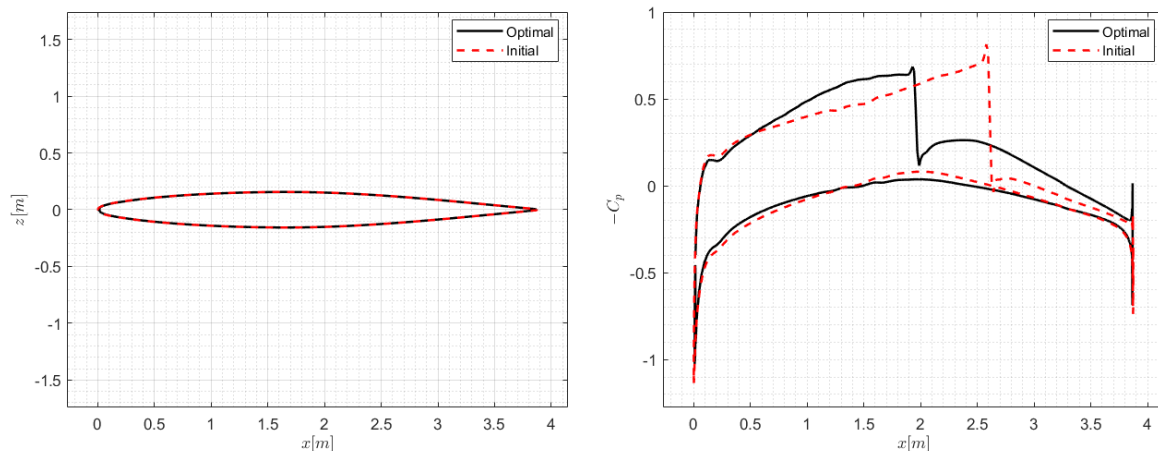


Figure 76 – Sectional airfoil shape and pressure coefficient extracted at $y/b = 0$.

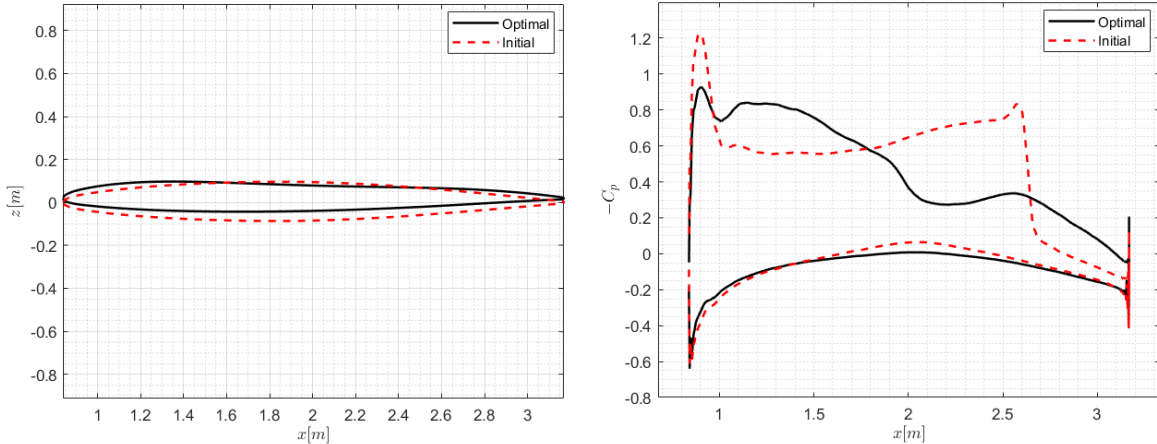


Figure 77 - Sectional airfoil shape and pressure coefficient extracted at $y/b = 0.23$.

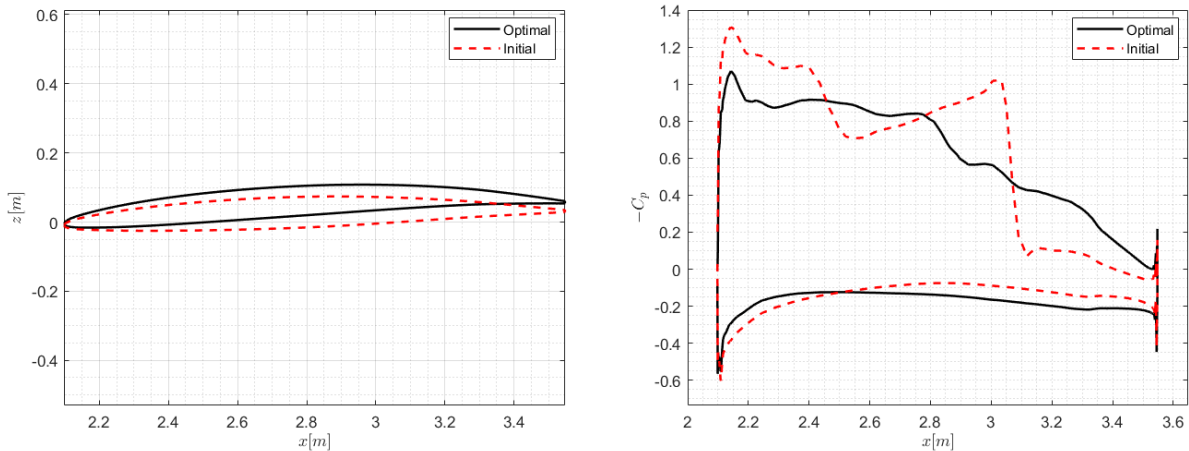


Figure 78 - Sectional airfoil shape and pressure coefficient extracted at $y/b = 0.6$.

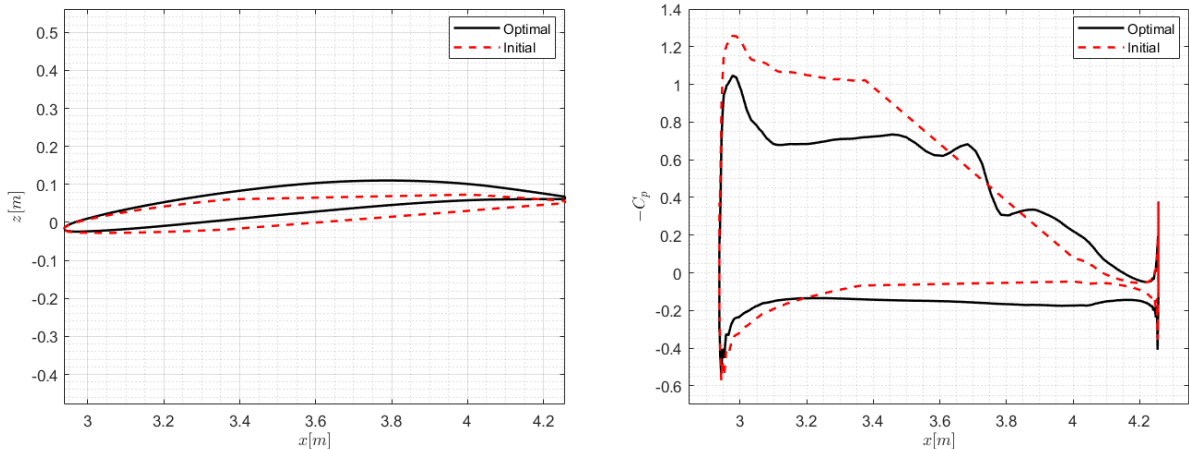


Figure 79 - Sectional airfoil shape and pressure coefficient extracted at $y/b = 0.83$.

The polar of the wing has been computed both on the original wing and on the optimized one. The results, presented in Figure 80 on the left, show an unexpected improvement of the performance of the wing also far from the design point selected for the optimization process. The lift-to-drag ratio is increased for almost all the range presented in Figure 81. Looking at the C_L at different values of the angle of attack, shown in Figure 80 on the right, the optimized wing

exhibits an increase in the lift coefficient for all the range analyzed between 0° and 6° . The significant improvement over a wide range of conditions can be explained if the initial wing was far from the optimal configuration, hence the single point optimization design has decreased the intensity of the shock wave at different AOA.

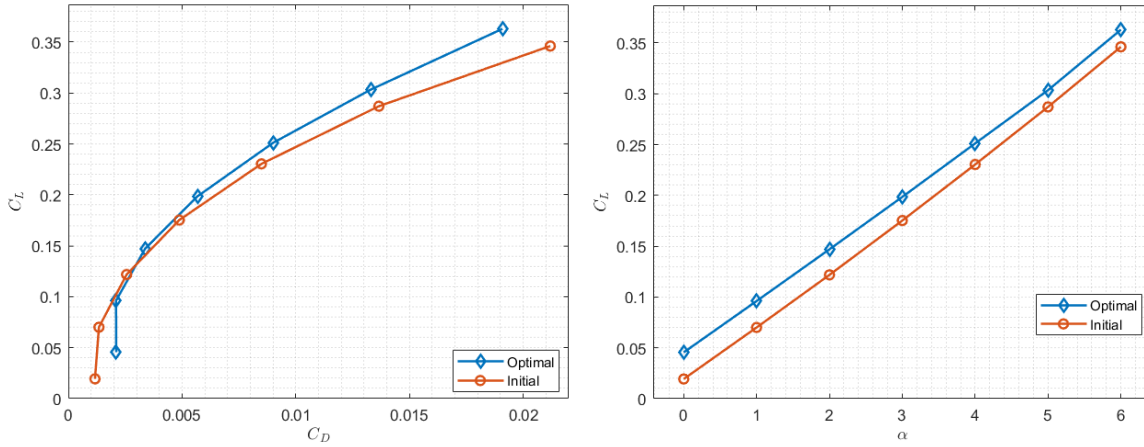


Figure 80 - Initial and optimal polar curve (left), $C_L - \alpha$ curve (right).

Lastly, another interesting condition to analyze is the behavior of the optimized wing at $M_a = 0.5$ and $\alpha = 4.5^\circ$. In this configuration the lift coefficient is increased of the 12.82%, but the C_D increased as well, passing from 57 counts of the initial wing to 66 counts for the optimized wing. The lift-to-drag ratio is slightly decreased from 33.6 to 32.5.

In conclusion, even though the only design condition considered was the one at $M_a = 0.85$, the new wing configuration shows only a slight decrease in the performance at $M_a = 0.50$. For further analysis, multiple Mach conditions can be taken into account, with the aim of obtaining the optimal configuration for a wide range of flight conditions. Moreover, for a more in-depth analysis, it is recommended to use a RANS solver for the optimization process, which would guarantee more accurate results, taking into account the effects of viscosity and turbulence modelling, giving higher fidelity results compared to the Euler solver. It will be also interesting to test with a RANS simulation the optimized wing obtained in this work. However, given the high computational demand of RANS simulations, access to a greater computational power would be necessary.

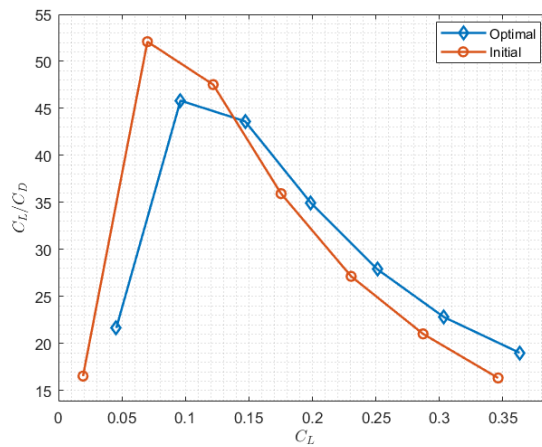


Figure 81 - Initial and optimal lift-to-drag ratio.

11. Conclusions and Open Points

The conclusions of the aerodynamic design of the STAD-1 are here reported. Open points left at the end of the design are here reported as well.

In this report, the preliminary aerodynamic design for the STAD-1 aircraft has been presented. Starting from data and objectives set in the design done in both the courses of Aircraft Design, the wing has been designed starting from its planform. Subsequently, considerations made on the wing and complete aircraft results with a VLM are explained, as well as the design of control surfaces that act as high-lift devices. Due to the tridimensional and transonic nature of the problem, the airfoil choice is done using Euler simulations with subsequent verifications using viscous simulations. The design of Leading Edge Extensions is proposed with the use of the mid fidelity tool DUST and the subsequent verification with Euler and RANS analyses.

Finally, the optimization of the wing with the use of an adjoint method coupled with Euler equations is carried out and its results are presented. Sadly, it is not possible to extrapolate the wing geometry and implement it on the complete aircraft, so the optimization's results are limited to the isolated wing.

The global process presented here shows how the best approach for a faster preliminary aerodynamic design of an aircraft with a medium aspect ratio, high sweep and transonic requirements is to base the design a lot on similarities with existing aircraft, as well as using different type of tools depending on the complexity of the geometry designed and the flight conditions.

It is possible to say that VLM methods allow for a quick iteration of the design when good but not extremely accurate results are needed, thus proving to be still an extremely valuable tool even in a modern aircraft design. Obviously, VLM methods come with their limitations, so to account for what VLM cannot consider mid and high-fidelity tools are a necessity. DUST proves to be an optimal medium fidelity tool, having results aligned even with high order methods in certain conditions, while Euler simulations prove to be the best trade-off between shockwaves capturing and computational cost. RANS simulations do still provide different results, and they consider viscosity which is extremely fundamental at higher angles of attack and for streamlined bodies, but does not change the results in terms of lift and drag substantially.

Obviously, the design presented here is not exempt from simplifications and open points. The limited computational power does not allow complete and extremely accurate viscous results and does not even allow to analyze the complete aircraft with even the lowest order viscous model, thus limiting the flow conditions that may be analyzed and the results of the viscous contribution. In conclusion, with the intention of considering the study completed, some analyses should be made taking into account:

- More precise viscous simulations with more flight conditions, especially higher angles of attack and/or sideslip conditions.
- Improved geometry design for the tail of the fuselage.
- More detailed design on the shape of the LEX.
- Full aircraft with the modelling of the internal ducts and deflected surfaces.

Acknowledgements

The team wants to express its deepest gratitude to people who significantly contributed to this project.

Firstly, the team acknowledge engineer Andrea Maccapani (Leonardo Helicopters S.p.A.) for its availability, constant support, and precious advice. Moreover, the team is thankful to Carlo Cassinelli (Leonardo Helicopters S.p.A.), Marco Stoppelli (Leonardo Aircraft S.p.A.) and Viola Rossano (Leonardo Aircraft S.p.A.) for their consultation in the aerodynamics field, Francesco Acerra (Leonardo Aircraft S.p.A.) for his consultation in the materials and RCS reduction field and Giorgio Travostino (Piaggio Aerospace) for its consultation over the aerodynamic optimization and CFD results.

In addition, the team is grateful to Professor Maurizio Boffadossi of Politecnico di Milano (DAER) for supporting the aerodynamics optimization process, to Professor Roberto Andriani of Politecnico di Milano (DAER) for his precious insights in the propulsion field, Professor Barbara Re of Politecnico di Milano (DAER) for support with the CFD analyses in SU2 and Postdoctoral Researcher Alberto Savino of Politecnico di Milano (DAER) for support with the DUST analyses.

Also, the team expresses its gratitude to Joana Da Silveira, Design student at Politecnico di Milano for creating the logo of the STAD-1 and helping with the design of the report. The team would like to thank Giacomo Moroni as well for the help in generating the renderings of the aircraft.

Lastly, the team would like to thank Professor Lorenzo Trainelli of Politecnico di Milano (DAER), Professor Carlo Emanuele Dionigi Riboldi of Politecnico di Milano (DAER), and Ph.D. candidate at Politecnico di Milano (DAER) Raffaello Terenzi for initiating and supporting the development of this project.

References

All the references considered for the team studies are reported below.

- [1] D. Raymer, "Aircraft Design - A Conceptual Approach", 2012.
- [2] D. C. Jenn, "RCS Reduction," 2008.
- [3] M. H. Sadraey, "Aircraft Design - A Systems Engineering Approach", 2013.
- [4] K. Huenecke, "Modern Combat Aircraft Design", 1987.
- [5] Wikipedia, ""Lockheed Martin F-22 Raptor", 2024.
- [6] J. Bridgewater, K. H. Wilson, ""Influence of Swept-Wing Wing Root Shaping on the Pressure Distribution Body Configurations", 1970.
- [7] M. B. Sol, ""Conceptual Design of Swept Wing Root Aerofoils", 2015.
- [8] Wikipedia, "Lockheed Martin F-35 Lightning II", 2024.
- [9] R. G. Carlson, R. H. Blackwell, G. L. Commerford, P. H. Mirick, "Dynamic Stall Modeling and Correlation With Experimental Data on Airfoils and Rotors".
- [10] S. Gudmundsson, "General Aviation Aircraft Design - Applied Methods and Procedures", 2022.
- [11] P. M. Sforza, "Commercial Airplane Design Principles", 2014.
- [12] P. Iannelli, J. Wild, M. Minervino, H. Struber, F. Moens, A. Vervliet, "Design of a High-Lift System for a Laminar Wing", 2013.
- [13] L. Morino, C. C. Kuot, "Subsonic Potential Aerodynamics For Complex Configurations: A General Theory", 1974.
- [14] M. Tugnoli, D. Montagnani, M. Syal, ""Mid-fidelity Approach to Aerodynamic Simulations of Unconventional VTOL Aircraft Configurations"".
- [15] O.C. Zienkiewicz, R.L. Taylor, P. Nithiarasu, "The Finite Element Method for Fluid Dynamics", 2014.
- [16] SU2, ""Turbulent ONERA M6", 2023. [Online].
- [17] Cadence, ""Accuracy, Convergence, and Mesh Quality", 2023. [Online].
- [18] D. Granata, A. Savino, A. Zanotti, ""Numerical Evaluation of Aircraft Aerodynamic Static and Dynamic Stability Derivatives by a Mid-Fidelity Approach", 2024.
- [19] NATO, ""AGARD AR-256 - Drag Prediction and Analysis from Computational Fluid Dynamics: State of the Art", 1988.
- [20] D. Lednicer, ""The Incomplete Guide to Airfoil Usage", 2023. [Online].
- [21] E. Torenbeek, "Synthesis of Subsonic Airplane Design", 1976.
- [22] W.H. Mason, ""Transonic Aerodynamics of Airfoils and Wings", 2006.
- [23] A. Kuzmin, ""On the lambda-shock formation on ONERA M6 wing", 2014.
- [24] R. Whitford, ""Design for Air Combat", 1987.

- [25] L. Malicki, Z. Malecha, K. Tomczuk, ""Influence on the Aerodynamic Characteristics of a Modern Fighter Jet", 2023.
- [26] J. Masud, O. Khan, S. M. Hassan, ""Intake and Airframe Characterization through Composite CFD", 2015.
- [27] A. Jameson, "Computational Aerodynamics for Aircraft Design", 1989.
- [28] A. Jameson, "Studies Of The Continuous And Discrete Adjoint Approaches To Viscous Automatic Aerodynamic Shape Optimization", 2001.
- [29] A. Savino, ""Dust User Manual", 2024. [Online].
- [30] D. A. Murray, An Elementary Course in the Integral Calculus, 1898.
- [31] R. L. Panton, Incompressible Flow, 2013.
- [32] V. Schmitt, F. Charpin, ""Pressure Distributions on the ONERA-M6-Wing at Transonic Mach Numbers", 1979. [Online].
- [33] J. Roskam, "Airplane Design", 1985.
- [34] Airfoil Tools, ""Airfoil Tools", 2024. [Online].

A. Appendix

The appendices related to the aerodynamic optimization chapter are here reported.

A.1. Wing Position

To fix the wing position, it is necessary to first evaluate if it is possible to obtain a suitable static margin in the whole center of gravity's position envelope. As suggested by Raymer [4], a static margin of -15% is typically adopted for unstable fighters, which can be subsequently artificially stabilized by the control action.

The CG excursion makes it impossible to obtain an adequate static margin for every wing position. Furthermore, the aircraft will suffer from trim problems on the longitudinal plane (beside the flying wings typical difficulties on yaw control). For these reasons, and to avoid excessively iterating the design, it has been chosen to include a V-tail.

A.2. Ruddervator

To size the ruddervator some suggestions taken from [1] have been at first considered, giving a control surface chord of 40% of the tail chord and a ruddervator that spans from 30% to 90% of the tail span.

Afterwards, together with the tail airfoil, it has been iterated in order to reduce the C_{D_0} and the trim drag, especially the latter needs to be minimized in order to achieve enough L/D . The final geometrical configuration is reported in Table 36 together with the used airfoil. In Figure 82 it is possible to see the configuration of the first to the last iteration.

	Initial Sizing	Final Design
Initial and Final C_f/C_{Tail} [%]	30 to 30	55 to 35
Initial and Final Span Location [m]	0.58 to 1.93	0.19 to 1.93
$\Lambda_{c/4}$ [°]	5.26	5.26
Λ_{LE} [°]	40°	40°
Tail Airfoil	NACA 0008	NACA 65A006

Table 36 - Ruddervator geometrical parameters and airfoils.

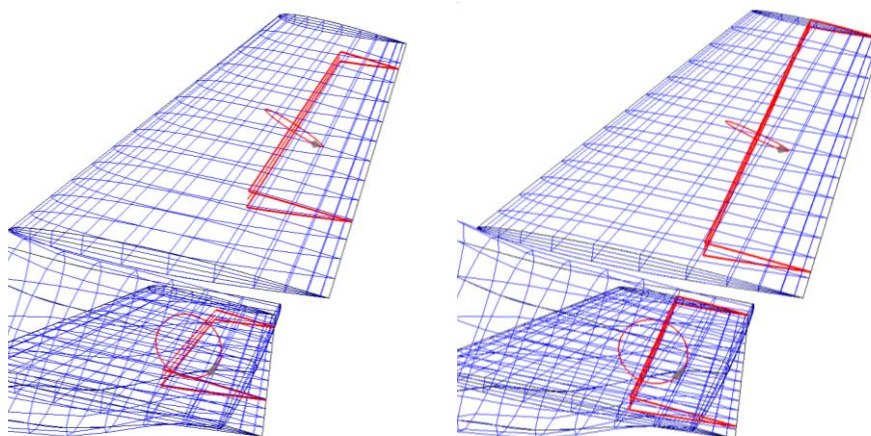


Figure 82 – Initial and final V-tail OpenVSP geometry.

A.3. Planform Design Validation

The results provided by OpenVSP have been compared to the results obtained by some semi-empirical formulas in order to validate the polar plots.

The $C_{L\alpha}$ can be computed with equation (A.1) and equation (A.2) taken from Raymer [1]:

$$C_{L\alpha} = \frac{2\pi AR}{2 + \sqrt{4 + \frac{AR^2\beta^2}{\eta^2} \left(1 + \frac{\tan^2 \Lambda_{max t/c}}{\beta^2}\right)}} \frac{S_{exposed}}{S_{ref}} F \quad (A.1)$$

Where:

$$\beta^2 = 1 - M^2 \text{ and } \eta = \frac{C_{l\alpha}}{2\pi/\beta} \quad (A.2)$$

And the F parameter is obtained by:

$$F = 1.07(1 + d/b)^2 \quad (A.3)$$

Where d is the fuselage maximum diameter and b the wingspan.

To obtain the sweep at maximum t/c ($\Lambda_{max t/c}$), the following equation has been used:

$$\tan(\Lambda_n) = \tan(\Lambda_m) - 4 \frac{(n-m)}{AR} \frac{1-\lambda}{1+\lambda} \quad (A.4)$$

where n and m are chord percentages position. In this case m = 0% (Leading edge) and n = 40% have been considered (NACA 64 series max t/c position).

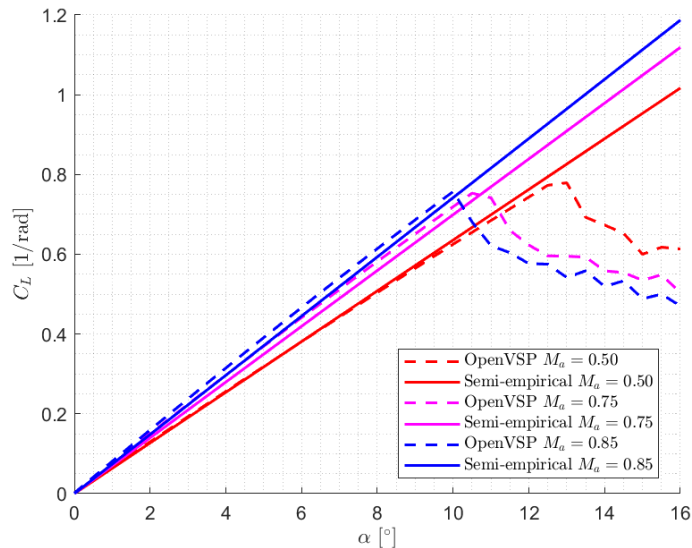


Figure 83 - C_L curve OpenVSP and semi-empirical formula comparison.

As it is possible to see in Figure 83, the values of OpenVSP are very close to the semiempirical results far from the stall region. Furthermore, at lower Mach number, the two values are almost the same, while at higher Mach values the two models exhibit a higher difference, this difference is most likely caused by the more precise compressibility corrections used in OpenVSP.

A.4. RANS Grid Convergence

Just like the isolated wing analyses done with the Euler solver, a grid convergence study must be performed for the RANS cases as well: this is not optional because a viscous solver requires a different mesh, which is extremely fine close to the body, and it is relaxed subsequently due to computational cost limitations. This allows to solve the flow conditions correctly in the near wall regions. To do this, the first cell height was kept small enough to obtain y^+ between 30 and 300, and the surface refinement is changed to obtain different mesh densities. This leads to the behavior shown in the following figures:

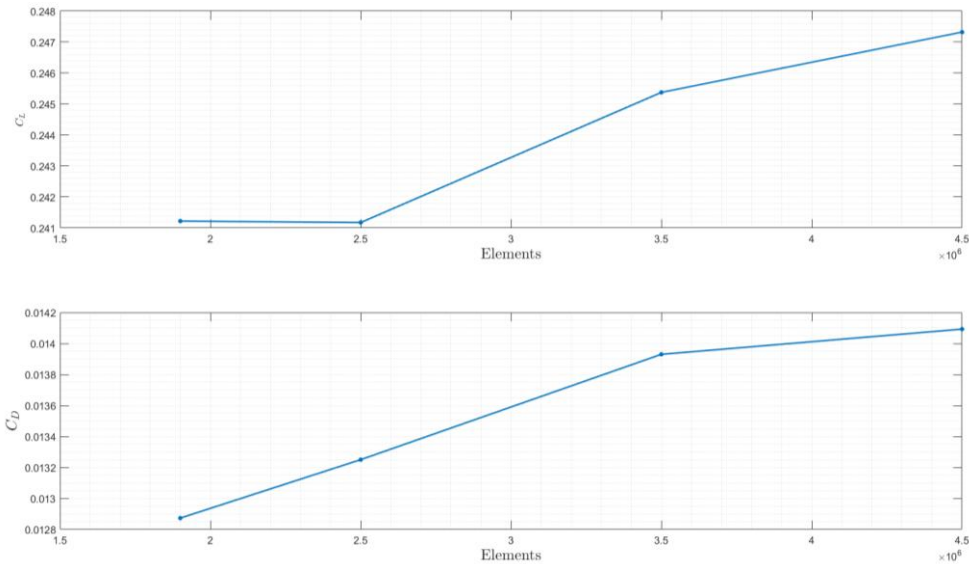


Figure 84 - Grid convergence results for the isolated wing for RANS.

It is easy to notice that an effective grid convergence is not met in this case, although the trend seems to signal a near-convergence. It is not possible to analyze a case with a higher cell count because of the computational limitations: 4.8 million cells are the estimate of maximum cell count for a compressible RANS simulation with SU2 and 16 GB of RAM memory. The RANS simulations have a lower maximum cell count due to the higher number of equations needed to solve the viscous contribution.

Nevertheless, the difference between 3.5 and 4.5 million cells in terms of drag coefficient is 0.79%, while the difference in terms of lift coefficient is 1.12%. With these results, it is expected that using a cell count between 3.5 and 4.5 million cells provides results that are overall accurate within less than 3% of error.

A.5. Full Body Grid Convergence

Firstly, it is important to note that this process will focus solely on the surface mesh due to a specific aspect of the project hypotheses: the use of a Euler method. Furthermore, the considerations will be mostly based on the outcomes obtained from the aircraft's surface.

Even though it has been stressed in other sections, it is significant to highlight that the analyses have been made for a very complex flow field around a body that can be considered bluff in many zones, using the Euler equations, which is quite a strong approximation. For this very reason, analysing the mesh convergence is not expected to be simple and intuitive.

Due to these particular conditions, a first-order convective scheme has been used for a provisional result, which has been used as a restart solution for a more accurate and precise second-order convective scheme. Even when adopting this precaution, for most simulations of the full body of the aircraft, the lift and drag coefficients values were not yet stable, even if convergence was reached with a residual of the density in the order of 10^{-6} . It is worth to note that since the main body it is close to a blunt body this is expected for a Euler analysis.

Nevertheless, the oscillations for the coefficients are of low magnitude and do not increase the residuals substantially, so an average of the last iterations may be made.

Additionally, to overcome the unsteady nature of the problem, a mean over the last 100 C_L and C_D values was performed for simulations that failed to achieve the desired convergence.

The parameters used for the grid generation are manually tuned to obtain five different mesh with five different refinements. It is essential to maintain coherency when changing refinements between one mesh and another, so basically the idea is to increase proportionally the elements in each part of the model.

	Mesh 1	Mesh 2	Mesh 3	Mesh 4	Mesh 5
Number of cells on the surface	60k	200k	360k	470k	630k
Number of cells in the volume	1.1mln	2.9mln	4.3mln	5.7mln	7mln

Table 37 - Different meshes prepared to investigate the convergence.

As illustrated by the results, a smooth variation of the coefficients has not been obtained when increasing the elements of the mesh.

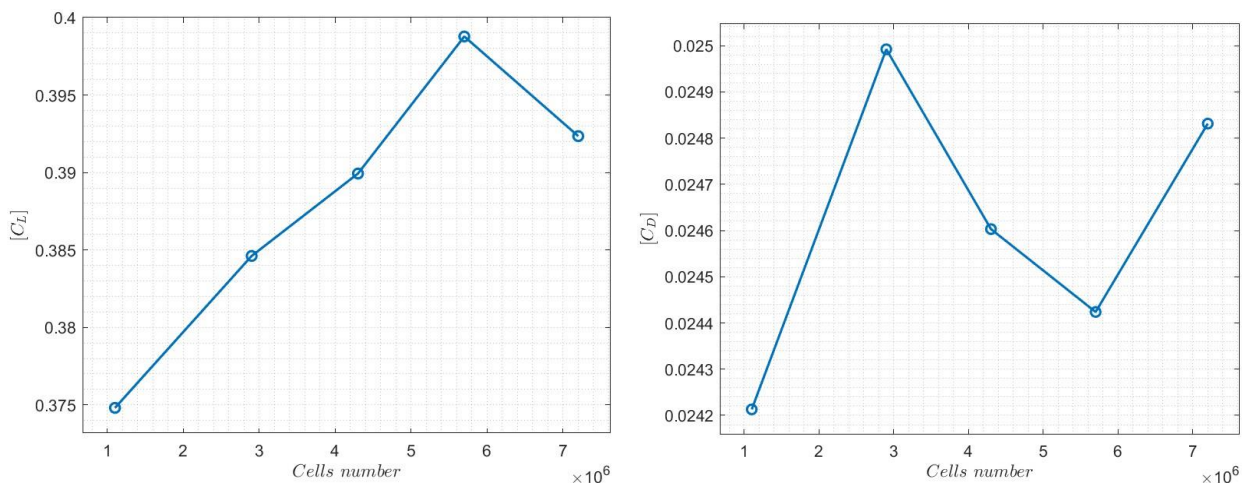


Figure 85 - Full body grid convergence.

The explanation of this behaviour can be found in the huge zone of instability placed in the rear part of the model where the steady and inviscid Euler method cannot capture the physics of the phenomena, which effects can majorly be seen in the drag coefficients.

The situation is far more different taking into account a restricted domain of interest, avoiding in this way the whole part that is creating this kind of problem hoping for a clearer and more evident trend convergence. By considering the coefficient computed over wing only as it can be seen from the plots in Figure 86, the situation greatly improves.

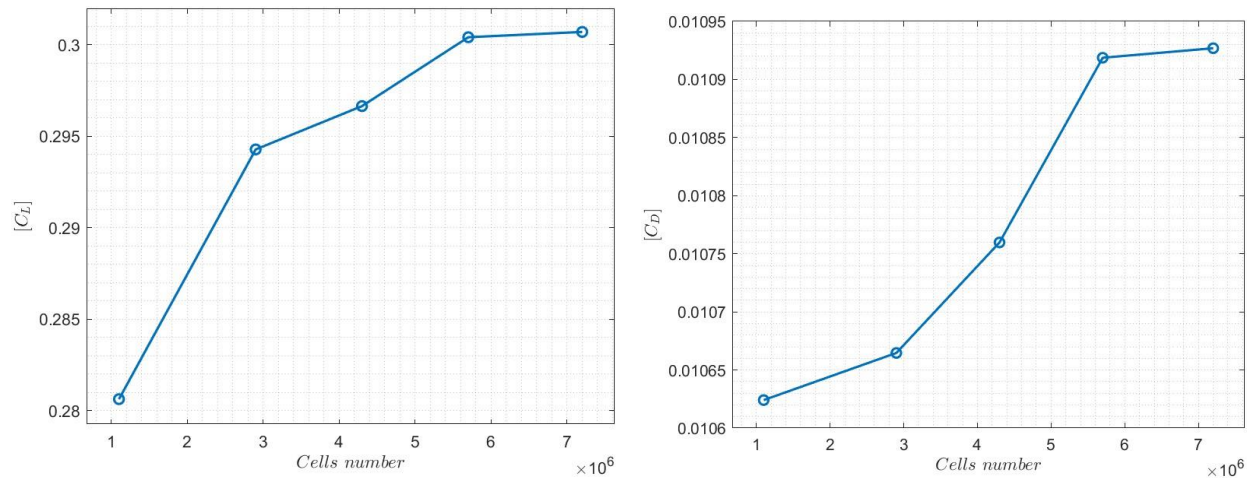


Figure 86 – Full body grid convergence with coefficients obtained considering only the wing.

In conclusion, all these considerations allow us to affirm that the Mesh 4, with nearly 5.7 million of elements provides the right compromise between correctly refining the critical zones of the aircraft and achieving a simulation that converges without taking too much time. This allows for continuous trial-and-error adjustments during the design phase of the aircraft.

Regarding the following project design changes, such as adding the LEX, we have decided not to conduct another grid convergence study for two main reasons. Firstly, it would require much more additional time, and secondly, we believe the current results are robust enough that minor changes to the aircraft will not significantly affect the overall cell count.

A.6. DUST Mathematical Model

In the following section the mathematical model and the hypotheses behind the DUST formulation are presented. The explanation is derived from the work of different papers and books, namely [18], [29], and [14].

A.6.1. Hypothesis and Governing Equation

The code is based on the vorticity-velocity formulation founded on Helmholtz's decomposition of the velocity applied to an incompressible Newtonian fluid. These two cornerstones of the method states that:

"Helmholtz decomposition theorem or the fundamental theorem of vector calculus states that any sufficiently smooth, rapidly decaying vector field in three dimensions can be resolved into the sum of an irrotational (curl-free) vector field and a solenoidal (divergence-free) vector field." [30]

"A Newtonian fluid is a fluid in which the viscous stresses arising from its flow are at every point linearly correlated to the local strain rate, the rate of change of its deformation over time." [31]

By applying these hypotheses to the Navier-Stokes equation:

$$\begin{cases} \nabla \cdot \mathbf{u} = 0 \\ \frac{\partial \mathbf{u}}{\partial t} + \mathbf{u} \cdot \nabla \mathbf{u} = -\frac{1}{\rho} \nabla p + \nu \nabla^2 \mathbf{u} \end{cases} \quad (A.5)$$

The velocity field can then be rewritten as a sum of a potential velocity \mathbf{u}_ϕ , linked to the panel elements, and a rotational velocity \mathbf{u}_ψ , linked to the wake particles.

$$\mathbf{u}(\mathbf{r}, t) = \mathbf{u}_\phi(\mathbf{r}, t) + \mathbf{u}_\psi(\mathbf{r}, t) \quad (A.6)$$

Once the velocity field is known the direct aerodynamic problem is solved and so the loads can be easily retrieved. Now the two velocity components will be analyzed more in detail.

Potential Velocity

The potential velocity is defined through the scalar potential of incompressible flow as:

$$\nabla \cdot \mathbf{u}_\phi = 0 \rightarrow \mathbf{u}_\phi = \nabla \phi \quad (A.7)$$

The potential part of velocity field follows the classical hypothesis of potential flow and so it is incompressible and irrotational. For such reason the scalar potential is a harmonic function and so it can be defined as a solution of a Laplace equation:

$$\nabla \cdot \mathbf{u}_\phi = \nabla \cdot \nabla \phi = \nabla^2 \phi = 0 \quad (A.8)$$

Rotational Velocity

Starting once again from the incompressibility condition applied to the velocity field even the rotation velocity can be defined:

$$\nabla \cdot \mathbf{u}_\psi = 0 \rightarrow \mathbf{u}_\psi = \nabla \times \psi \quad (A.9)$$

To retrieve this definition, the vector potential ψ has been considered solenoidal. So, by considering the definition of vorticity and the solenoidality of ψ , the rotatory part of the velocity field can be expressed as a solution of a Poisson equation:

$$\nabla \times \mathbf{u} = \nabla \times \mathbf{u}_\psi = \nabla(\nabla \cdot \psi) - \nabla^2 \psi = \mathbf{0} - \nabla^2 \psi = \boldsymbol{\omega} \quad (A.10)$$

Finally, the vorticity is described by the vorticity equation:

$$\frac{D\boldsymbol{\omega}}{Dt} = (\boldsymbol{\omega} \cdot \nabla) \mathbf{u} + \nu \nabla^2 \boldsymbol{\omega} \quad (A.11)$$

The two differential problems just described are both in the fluid domain Ω_f and will be both manipulated using Green's function method to obtain the solution of the aerodynamic problem.

A.6.2. Solution of Lagrange Equation

First, the problem is reformulated using a perturbative approach:

$$\varphi = \phi - \phi_\infty \quad (A.12)$$

$$\mathbf{u}_\varphi = \mathbf{u}_\phi - \mathbf{U}_\infty \quad (A.13)$$

The potential problem can so be rewritten as:

$$\nabla^2 \varphi = 0, \quad \text{in } \Omega_\varphi \quad (A.14)$$

The solution of the problem relies on superimposition of surface element singularities. The fluid domain Ω_φ is limited by:

$$\partial \Omega_\varphi = S_s \cup S_v \cup S_l \cup S_w \quad (A.15)$$

Where S_s stands for surface panel, S_v for vortex lattice elements, S_l for lifting lines and S_w for wake panels. Following a classical Morino formulation the differential problem is rewritten as a boundary element problem using Green's function method:

$$\begin{aligned} E(\mathbf{r})\varphi(\mathbf{r}, t) &= \oint_{S_s} \hat{\mathbf{n}}(\mathbf{r}_0, t) \cdot \nabla_0 G(\mathbf{r}_0, \mathbf{r}) \varphi(\mathbf{r}_0, t) dS(\mathbf{r}_0) \\ &+ \oint_{S_v \cup S_l \cup S_w} \hat{\mathbf{n}}(\mathbf{r}_0, t) \cdot \nabla_0 G(\mathbf{r}_0, \mathbf{r}) \Delta\varphi(\mathbf{r}_0, t) dS(\mathbf{r}_0) \\ &- \oint_{S_s} G(\mathbf{r}_0, \mathbf{r}) \hat{\mathbf{n}}(\mathbf{r}_0, t) \cdot \nabla_0 \varphi(\mathbf{r}_0, t) dS(\mathbf{r}_0) \end{aligned} \quad (A.16)$$

The formulation can be completed by the boundary conditions. The different aerodynamic models will be analyzed separately since are defined by different boundary conditions, singularity distribution and load computation.

Surface panels (S_s and S_w)

The boundary integral is solved by the collocation method. The surface is divided into panels defined by the intensity of the doublets and sources on the thick surfaces and by only doublets on the thin surfaces (as the wake). The discrete counterpart of the problem can be written as follows:

$$\sum_{k_s=1}^{N_s} A_{i_s k_s} \mu_{k_s} + \sum_{k_v=1}^{N_v} A_{i_s k_v} \mu_{k_v} + \sum_{k_l=1}^{N_l} A_{i_s k_l} \mu_{k_l} + \sum_{k_s=1}^{N_s} B_{i_s k_s} \sigma_{k_s} + \sum_{k_w=1}^{N_w} A_{i_s k_w} \mu_{k_w} = 0, \quad \forall i_s = 1, \dots N_s \quad (A.17)$$

Where A_{ik} and B_{ik} are the induced potential of the k^{th} doublet and sources panels, μ_{i_s} is the intensity of the doublet of each surface panel, σ_{i_s} is the intensity of the sources of each surface panel, μ_{i_w} is the intensity of the doublet on the wake and μ_{k_l} is the intensity of the vortex ring that models the lifting line elements.

At each time step μ_{i_w} is known from the previous time step, μ_{i_s} is obtained by solving the linear system in Equation (A.17) and σ_{i_s} is obtained from the following boundary condition:

$$\hat{\mathbf{n}} \cdot \mathbf{u}_\varphi = \hat{\mathbf{n}} \cdot \nabla \varphi = \hat{\mathbf{n}} \cdot (\mathbf{u}_b - \mathbf{U}_\infty - \mathbf{u}_\psi) = \sigma_{i_s} \quad (A.18)$$

Where \mathbf{u}_b represents the motion of the surface S_s relative to a reference frame subjected to free stream velocity \mathbf{U}_∞ .

Vortex Lattice (S_v)

This model is used to model lifting bodies as a zero-thickness vortex sheet defined by a piecewise-uniform distribution of doublet with the same intensity $\mu_{i_v} = \Gamma_{i_v}$. In complete analogy to what has been done with the surface panels, a linear system that made explicit the contribution to the velocity of every singularity is written:

$$\sum_{k_s=1}^{N_s} C_{i_s k_s} \mu_{k_s} + \sum_{k_v=1}^{N_v} C_{i_s k_v} \mu_{k_v} + \sum_{k_l=1}^{N_l} C_{i_s k_l} \mu_{k_l} + \sum_{k_s=1}^{N_s} D_{i_s k_s} \sigma_{k_s} + \sum_{k_w=1}^{N_w} C_{i_s k_w} \mu_{k_w} = \sigma_{i_v}, \quad (A.19)$$

$\forall i_v = 1, \dots N_v$

The non penetration boundary condition written in the control point of every vortex lattice element complete the linear system by defining the value of σ_{i_v} :

$$\hat{\mathbf{n}} \cdot \mathbf{u}_\varphi = \hat{\mathbf{n}} \cdot (\mathbf{u}_b - \mathbf{U}_\infty - \mathbf{u}_\psi) =: \sigma_{i_v} \quad (A.20)$$

Lifting lines (S_l)

This model represents slender lifting bodies as a lifting line (1D model). In terms of singularity is equivalent, as anticipated, to a vortex ring which intensity is defined through the solution of a fixed-point problem solved by means of tabulated data of its lifting section and intensity of the other singularities.

$$\boldsymbol{\mu}_{k_l} = f_{i_l}(\boldsymbol{\mu}_{k_s}, \boldsymbol{\mu}_{k_v}, \boldsymbol{\mu}_{k_l}, \boldsymbol{\sigma}_{k_s}, \boldsymbol{\mu}_{k_w}) \quad (A.21)$$

A.6.3. Solution of Poisson Equation

In DUST the evolution of wake can be managed in two ways: using wake panel (as seen in 0) or, when is important to study its interaction with other bodies, using vortex particles.

In the second case the rotational part of the velocity is produced by vortex particles used to model free vorticity in the domain. The vorticity field $\boldsymbol{\omega}(\mathbf{r}, t)$ is the curl of rotational velocity and using Green's function method the rotational velocity and the vector potential can be expressed as function of it:

$$\boldsymbol{\psi}(\mathbf{r}, t) = \int_{\Omega_f} G(\mathbf{r}, \mathbf{r}_0) \boldsymbol{\omega}(\mathbf{r}_0, t) dV(\mathbf{r}_0) \quad (A.22)$$

$$\mathbf{u}_\psi(\mathbf{r}, t) = \nabla \times \boldsymbol{\psi} = \int_{\Omega_f} \mathbf{K}(\mathbf{r}, \mathbf{r}_0) \times \boldsymbol{\omega}(\mathbf{r}_0, t) dV(\mathbf{r}_0) \quad (A.23)$$

Where G is the Green's function of the Laplace equation and K is the gradient of G with respect to the first argument. The wake particles are generated from the wake panels after a prescribed number of time steps. In the following sections will be explained better how the wake particles model the evolution of the free vorticity (0) and how the wake panels are converted into particles (0).

Vortex Particle Method in DUST

By employing the Vortex Particle Method (VPM) the vorticity field and rotatory velocity is approximated as the sum of the contribution of vortex particles of intensity $\alpha_p(t)$ and position $\mathbf{r}_p(t)$:

$$\boldsymbol{\omega}(\mathbf{r}, t) = \sum_{i_p=1}^{N_p} \boldsymbol{\alpha}_{i_p}(t) \zeta(\mathbf{r} - \mathbf{r}_{i_p}(t)) \quad (A.24)$$

$$\mathbf{u}_\psi(\mathbf{r}, t) = \sum_{i_p=1}^{N_p} \mathbf{K}_\zeta(\mathbf{r}, \mathbf{r}_{i_p}(t)) \times \boldsymbol{\alpha}_{i_p}(t) \quad (A.25)$$

Where ζ is a cut-off function determining the distribution of vorticity induced by the vortex particles and \mathbf{K}_ζ is the discrete kernel chosen to be consistent with the cut-off function.

For example, if ζ is a Dirac-delta the corresponding kernel would be the Biot-Savart kernel. Considering DUST, the chose of ζ leads to the Rosenhead-Moore Kernel:

$$\mathbf{K}_\zeta(\mathbf{x}, \mathbf{y}) = -\frac{1}{4\pi} \frac{\mathbf{x} - \mathbf{y}}{(|\mathbf{x} - \mathbf{y}|^2 + R_v^2)^{3/2}} \quad (A.26)$$

The choice has been driven by the fact that this kernel fits particularly well with the cartesian Fast Multipole Method (another function implemented in dust) that allows to reduce the computational cost.

The evolution of the vorticity field (now modeled as a group vortex particles) is once again redefined using a Lagrangian discrete approximation by the VPM through the dynamical equation of the position and intensity of the vortex particles:

$$\begin{aligned} \frac{d\mathbf{r}_{i_p}}{dt} &= \mathbf{u}(\mathbf{r}_{i_p}(t), t) \\ \frac{d\boldsymbol{\alpha}_{i_p}}{dt} &= \nabla \mathbf{u}(\mathbf{r}_{i_p}(t), t) \cdot \boldsymbol{\alpha}_{i_p} + \nu " \Delta \boldsymbol{\alpha}_{i_p}" \end{aligned} \quad (A.27)$$

In the first equation the convection of the i^{th} vortex particle is described, while the second one describes the influence of vortex stretching tilting and vortex diffusion on the intensity of the particles.

So, the vortex particles which evolution is described in the upper equations models the free vorticity and by means of the Equation (A.25) gives their contribute to the total flow velocity field.

Wake panel conversion in vortex particles

The conversion of the wake panel into vortex particles is done by integrating the intensity of the vorticity from the sides of the vortex lattice element. However, since each vortex ring has constant intensity over a closed path the resultant value would be null. To avoid this even the contribute of the neighboring wake panels is considered as follows:

$$\alpha_{i_p} = J_{Left} + J_{Right} + J_{End Side} \quad (A.28)$$

Where:

$$J_{Left/Right} = \begin{cases} \int_S \frac{1}{2} (\mu_{w,i} - \mu_{w,j}) dl \\ \int_S \mu_{w,i} dl \end{cases} \quad (A.29)$$

$$J_{End\ Side} = \int_S (\mu_{w,i} - \mu_{w,j}) dl \quad (A.30)$$

The newly generated particle is positioned at the center of the previous panel, as shown in Figure 87 and starts evolving according to the equations described in 0.

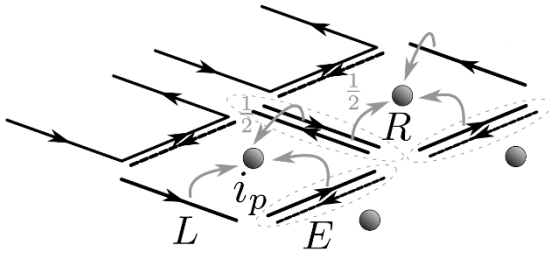


Figure 87 – Scheme of the wake panel to particle conversion in DUST

A.6.4. Dynamic System and Time Evolution

Now that has been explained how to compute $\mathbf{u}(r, t)$ in both potential and rotatory part starting from the singularities value, it's time to define the method to solve the linear system that has as unknown the singularities value themselves. At each time step a complete dynamic system containing the mixed solution of potential-velocity problem and lifting line fixed point problem is built and solved as follows:

1. Boundary condition σ are computed
2. Solution of the mixed potential-velocity problem is computed
3. Solution of the nonlinear problem for lifting line is found
4. Evolution of the panel wake
5. Evolution of the particles wake

The mixed potential-velocity problem is a linear system obtained by merging Equation (A.17) and Equation (A.19):

$$\begin{bmatrix} A_{ss} & A_{sv} \\ C_{vs} & C_{vv} \end{bmatrix} \begin{pmatrix} \mu_s \\ \mu_v \end{pmatrix} = - \begin{bmatrix} A_{sl} \\ C_{vl} \end{bmatrix} \boldsymbol{\mu}_l - \begin{bmatrix} B_{ss} & \emptyset_{sv} \\ D_{vs} & -I_{vv} \end{bmatrix} \boldsymbol{\sigma} - \begin{bmatrix} A_{sw} \\ C_{vw} \end{bmatrix} \boldsymbol{\mu}_w \quad (A.31)$$

DUST reorders the system to separate the stationary elements and the elements in motion. For the stationary part the system is factorized only the first time and then in the following time step only the non-stationary part is updated and computed.

Once the linear system is solved and (μ_s, μ_v) has been founded, the attention shifts on the fixed-point problem of the lifting line. Using the solution just computed, the value of $\boldsymbol{\mu}_l$ is retrieved by solving the Equation (A.21).

Now that every singularity value is solved for a defined time instant the wake must be updated.

For lifting line and vortex lattice elements the wake panel shed from the trailing edge has the same intensity as the vortex ring at the TE, to satisfy the Kutta condition. The situation is

different for surface panel elements, in this case a row of implicit wake panel is introduced to guarantee the Kutta condition.

$$\mu_{w,i_{TE}} = \mu_{s^{up},i_{TE}} - \mu_{s^{low},i_{TE}} = T \mu_{s,i_{TE}} \quad (A.32)$$

The Equation (A.31) can be changed as follows to consider the procedure of the implicit wake panel computation:

$$\begin{bmatrix} \tilde{A}_{ss} & A_{sv} \\ \tilde{C}_{vs} & C_{vv} \end{bmatrix} \begin{pmatrix} \mu_s \\ \mu_v \end{pmatrix} = - \begin{bmatrix} A_{sl} \\ C_{vl} \end{bmatrix} \boldsymbol{\mu}_l - \begin{bmatrix} B_{ss} & \emptyset_{sv} \\ D_{vs} & -I_{vv} \end{bmatrix} \boldsymbol{\sigma} - \begin{bmatrix} A_{s\tilde{w}} \\ C_{v\tilde{w}} \end{bmatrix} \boldsymbol{\mu}_{\tilde{w}} \quad (A.33)$$

Where \tilde{A}_{ss} and \tilde{C}_{vs} are the modified influence term that allows to compute the implicit wake panel and $\boldsymbol{\mu}_{\tilde{w}}$ is the normal wake panel considered until now.

$$\tilde{A}_{ss} = A_{ss} + A_{sw_{TE}} T \quad (A.34)$$

$$\tilde{C}_{ss} = C_{ss} + C_{sw_{TE}} T \quad (A.35)$$

A.6.5. Load Computation

Once all the singularities intensity are known, and so the velocity field, the aerodynamic loads acting on the different bodies can be computed. Because of the presence of the vortex particles the velocity field isn't irrotational and so the Bernoulli principles can't be applied.

Again, for the different aerodynamic models adopted, different ways to compute the loads on them are defined.

Surface Panel Loads

The inviscid load computation on the surface panels relies on the solution of Poisson's problem. In DUST is solved, once again, by recasting it in a boundary formulation:

$$\begin{aligned} E(\mathbf{r})B(\mathbf{r}, t) - \oint_{S_s} \hat{\mathbf{n}}(\mathbf{r}_0, t) \cdot \nabla_0 G(\mathbf{r}_0, \mathbf{r}) B(\mathbf{r}_0, t) dS(\mathbf{r}_0) &= \\ + \oint_{S_s} G(\mathbf{r}_0, \mathbf{r}) \hat{\mathbf{n}}(\mathbf{r}_0, t) \cdot \frac{\partial \mathbf{u}}{\partial t}(\mathbf{r}_0, t) dS(\mathbf{r}_0) \\ - \int_{\Omega_\varphi} \nabla_0 G(\mathbf{r}_0, \mathbf{r}) \cdot \boldsymbol{\omega}(\mathbf{r}_0, t) \times \mathbf{u}(\mathbf{r}_0, t) dV(\mathbf{r}_0) \\ - \nu \oint_{S_s} G(\mathbf{r}_0, \mathbf{r}) \hat{\mathbf{n}}(\mathbf{r}_0, t) \cdot \nabla_0^2 \mathbf{u}(\mathbf{r}_0, t) dS(\mathbf{r}_0) \end{aligned} \quad (A.36)$$

Where $B = (P - P_\infty)/\rho + (|\mathbf{U}|^2 - |\mathbf{U}_\infty|^2)/2$ and the solution is obtained by exploiting the matrices A_{ss} and B_{ss} of the potential velocity problem.

Vortex lattice loads

For vortex lattice element the loads computation relies on the unsteady formulation of the Kutta problem for incompressible flow:

$$\mathbf{F}_i = \rho \mathbf{u}_i \times \mathbf{l}_i (\mu_i - \mu_{i-1}) - \rho A_i \frac{d\mu_i}{dt} \mathbf{n}_i \quad (A.37)$$

Where \mathbf{l}_i is the vector of the first edge of the panel perpendicular to free stream, \mathbf{u}_i the velocity at the center of such edge, A_i the area of the panel, \mathbf{n}_i the normal of the panel, μ_i the intensity of the doublet of the panel and μ_{i-1} the intensity of the previous panel in chordwise direction.

Lifting lines loads

Considering the lifting lines elements the aerodynamic loads is obtained as a sum of two contributes. The steady contribution is evaluated with tabulated steady sectional aerodynamic coefficient (given as input in DUST), while, the unsteady contribution, is computed once again with the unsteady version of the Kutta-Joukowski theorem as done in Equation (A.37).

A.7. More on DUST

More details on DUST, regarding its workflow and architecture, are here presented for completeness. The sensitivity analyses and the STAD-1 modulization on DUST are also included in this section.

A.7.1. DUST Workflow

The typical and suggested workflow with DUST [29] is illustrated in Figure 88. The initial inputs are CAD surface mesh of the body in CGNS or ASCII format and/or parametric directive written in an .in file form which DUST_pre generates a binary geometry file. The output of the preprocessor is passed to DUST solver with a reference file, that assigns different reference systems to the components created by the preprocessor, and the simulation conditions (both inputs are given as “*.in” files).

The results produced by the solver can be then postprocessed to obtain some different results based on the input given to DUST_post. Some of the possible outcomes can be visualization, flow fields and loads distribution.

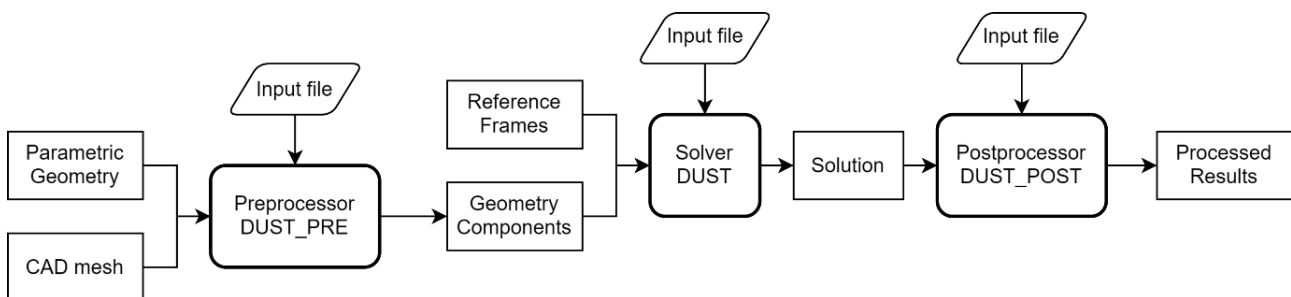


Figure 88 – suggested workflow for DUST

A.7.2. DUST Analysis Architecture

Considering all the different analysis to perform with DUST and the big number of results that must be post-processed, the aerodynamic code has been interfaced with MATLAB software by means of a custom infrastructure entirely written in MATLAB language and python 3. In the following lines the architecture of this project will be discussed and briefly explained with the help of the following flowchart:

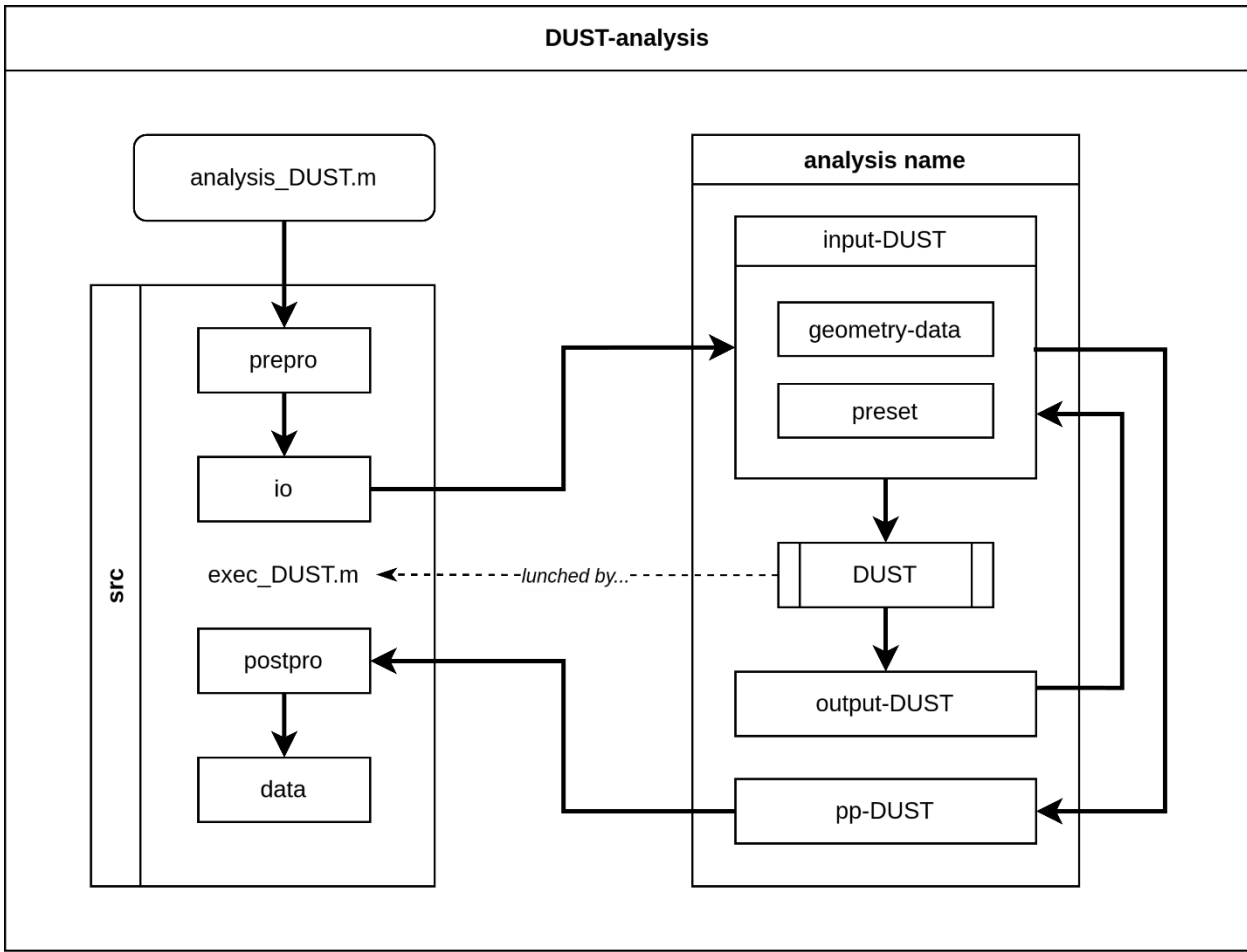


Figure 89 – DUST analysis MATLAB code architecture

The data flow always starts from the corresponding analysis MATLAB script. In this file the “INPUT” section must be used to define all the parametric variables object of the study and reference values. When the script is run all these variables are initialized in the workspace and will be used during all the analysis by different MATLAB functions to compute the result.

The next step consists in creating all the input file needed by DUST starting from the parametric variable just written and some preset assets written in the “preset” folder. The preset files can be easily edited to change some fixed input of the parametric run by following the DUST user guide [29], anyway is important to not change the file names otherwise the MATLAB functions won’t be able to read it anymore.

Once all the input files have been created the script automatically runs the complete DUST workflow previously presented (view A.7.1) for all the set of input variables defined by the user. The raw DUST output will be saved in “output-DUST” folder, while the post-processed results will be saved in “pp-DUST” folder. The integral loads computed during the different parametric simulations are automatically parsed and post-processed by MATLAB functions in three different “.mat” files: one containing the complete time-marching simulation result, one the aerodynamic loads and the last one for the structural loads.

All the simulations results stored in memory can be easily deleted whenever the user wants (to clean up “analysis cache”) by using the MATLAB functions contained in the “data” folder and already implemented in “main” and “analysis_DUST.m” scripts.

A.8. Validation on ONERA M6

A validation of the Euler and DUST analyses have been performed in this section by comparing their results with the ONERA M6 test case.

ONERA M6 is a swept symmetric semi-span wing designed in 1972 by ONERA Aerodynamics Department as an experimental geometry for studying three-dimensional, high Reynolds numbers flows with some complex flow phenomena such as transonic shocks.

M6 wing has been kept as a common test case in the computational fluid dynamic world, so, even if in the official experimental data doesn't contains lift and drag coefficient values, many people have done numerical studies and published data with different codes, mesh types, flow schemes etc. For this reason, we run some preliminary simulation on ONERA wing to validate and compare the precision of the different aerodynamic code that we are going to use in our experiments with the CFD and experimental data published on the web.

We have considered two different flow conditions, one subsonic and one transonic, to address and verify the limits of the formulations implemented in the different software used.

A.8.1. ONERA M6 Geometry

In the following table will be reported the complete set of model geometry data used to build the model of the ONERA M6 wing. The source of this data is the original research paper written by V. Schmitt and F. Charpin [32].

MAC [m]	Span [m]	AR [-]	Taper	LE sweep [°]	TE sweep [°]
0.646	1.196	3.800	0.562	30.0	15.8

Table 38 - ONERA M6 geometrical data.

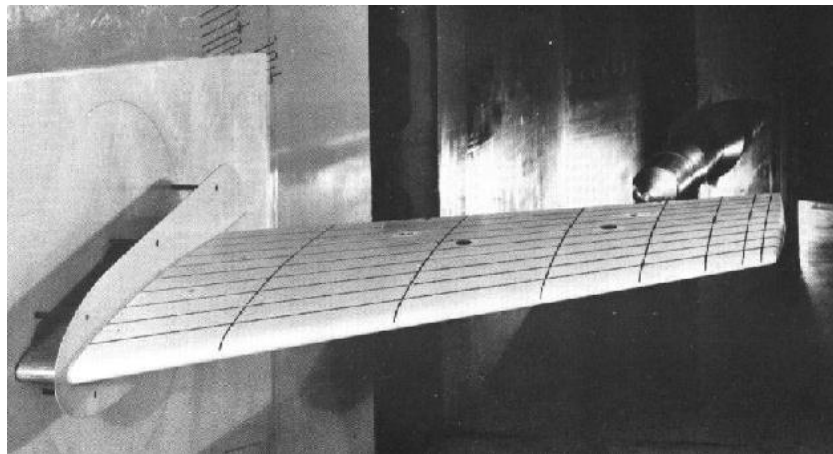


Figure 90 – ONERA M6 wing original wind tunnel testing model

A.8.2. DUST Model

The ONERA M6 wing has been reproduced in DUST using a parametric geometry input file (Figure 91). The aerodynamic model chosen for the analysis has been the “Surface panel” to have a good representation of the thickness of the body.

The airfoil data used are the one present in the original ONERA M6 paper [32] while the surface meshing and flow parameters input chosen has been reported in the following table:

Component type	Chord panels	Span panels	Panel distribution
Panels	20	50	Uniform

Table 39 – ONERA M6’s DUST panelization parameters.

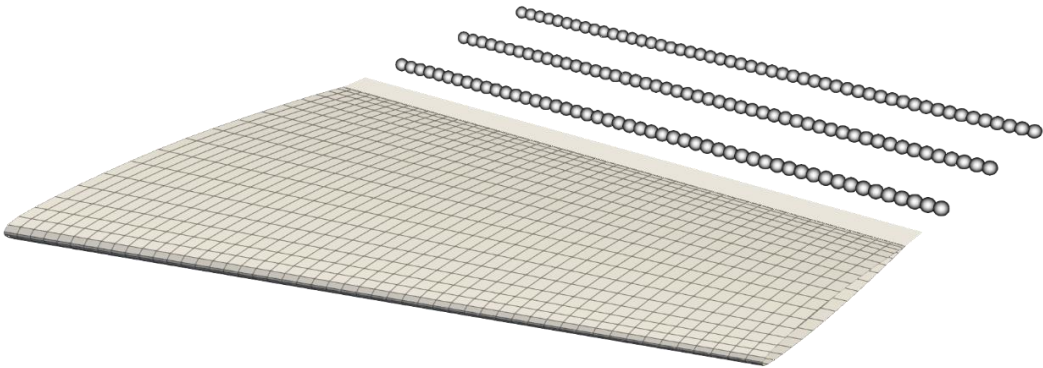


Figure 91 – ONERA M6 wing DUST panel model

A.8.3. SU2 Model

The computational domain for the CFD analysis of the ONERA M6 wing is a rectangular box with the wing mounted on one of the boundaries in the x-z plane, and the size of the domain is approximatively 17 times the mean aerodynamic chord in all the directions. The unstructured mesh has 5.82×10^5 cells. The solver used is Euler and a symmetry boundary condition is imposed on the side of the box, exploiting the symmetry of the problem and allowing to simulate only half of the problem. The Euler-wall boundary condition is applied to all the wing surface, and a Far-field condition is applied to the external wall.

The numerical scheme employed is the Jameson-Schmidt-Turkel (JST), which is a second order centered scheme. The main feature of this method is the use of a term of artificial dissipation in the numerical flux, which helps to stabilize the numerical solution and prevent non-physical oscillations, a crucial aspect when it comes to deal with discontinuities and shock waves. The convergence parameter is the root mean square residual of density and it has been set to 10^{-12} .

A.8.4. Subsonic Testing

We have analyzed the ONERA M6 wing at Mach 0.30 and three different angle-of-attack: 0° , 3.06° and 6.12° . Further info on the free stream condition can be found in Table 40.

The computation has been executed with different open-source software that implements different methods such as VLM, panel method and CFD.

Mach [-]	Static pressure [Pa]	Temperature [$^\circ$ C]	α [$^\circ$]	β [$^\circ$]
0.30	12767	15	0	0
0.30	12767	15	3.06	0
0.30	12767	15	6.12	0

Table 40 – ONERA M6 subsonic testing free stream condition

The main goal was to verify that in subsonic condition, where no shockwaves are expected, the low and mid-fidelity software gives a good approximation of the results in terms of aerodynamic integral load.

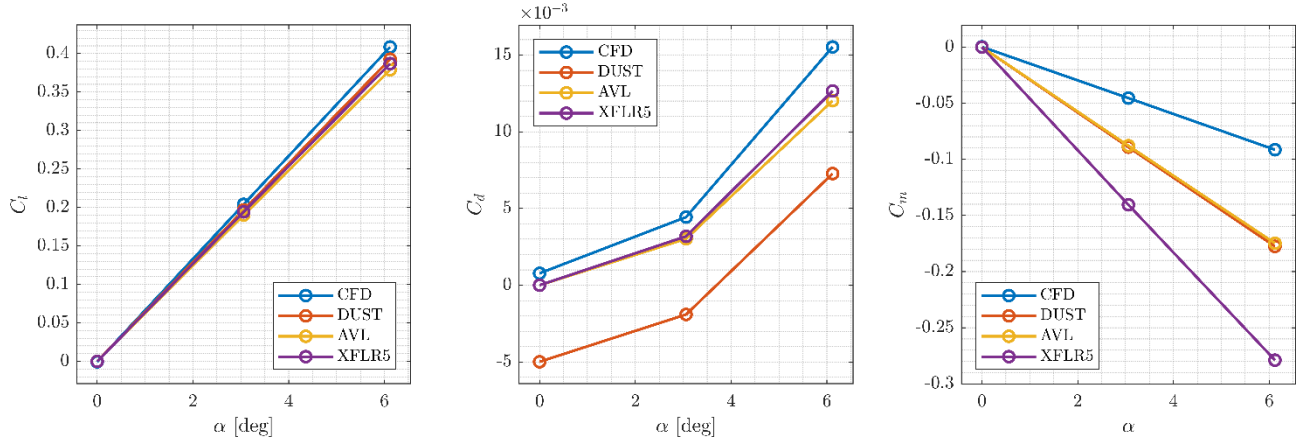


Figure 92 – ONERA M6 integral loads at Mach 0.30 and AOA 3.06°

The focus will be now put on the compare between DUST and CFD since the correlation between these two methods is a cornerstone of our Aerodynamics optimization that will be conducted later. The comparison will be executed considering the pressure coefficient distribution.

To provide initial qualitative insights, the comparison of the C_p distribution is presented side-by-side. In Figure 93 on the left can be seen the results obtained using DUST, and on the right, there are the results obtained using the Euler CFD model. Before considering numerical outputs, it is evident that the color patterns shown are relatively similar on both sides, so positive outcomes should be expected.

It is important to note that on the left, the panel discretization of the wing is visible, whereas on the right, the Euler method integrates results across the entire surface.

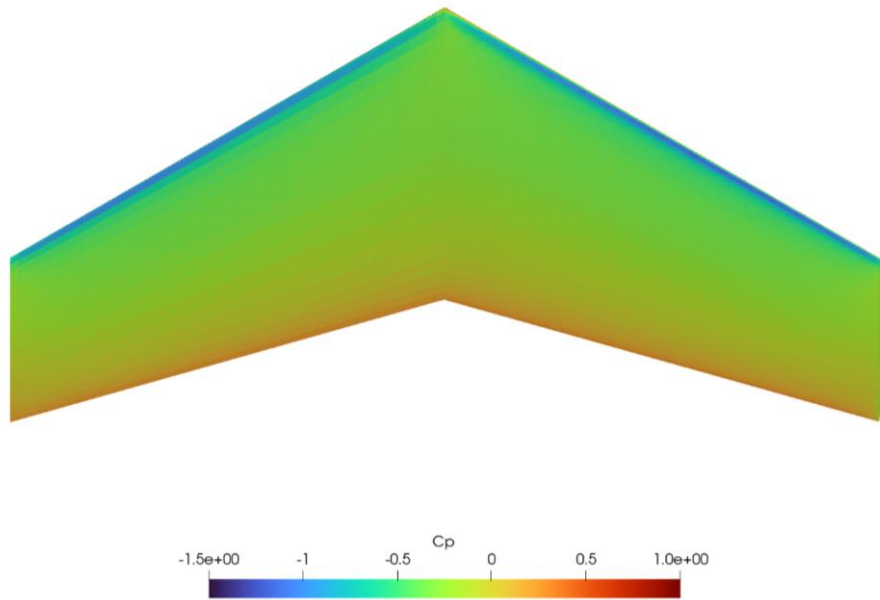


Figure 93 – ONERA M6 surface pressure distribution at Mach 0.30 and AOA 3.06°.

Looking more in detail at the results obtained, the C_p distribution along the chord at three different span stations is here plotted to understand how much DUST and the CFD get close one to the other. As anticipated, the DUST model provides only one output value per panel. Despite this, it allows us to see that the leading and trailing edges are the only zones where the results do not fully match, while along the rest of the chord, the two methods provide consistent outputs. The slight discrepancy between DUST and the Euler method is closely related to their

inability to capture viscous effects, which are significant in subsonic testing. This is why mismatches are particularly evident at the leading edge, where a high-pressure stagnation point occurs.

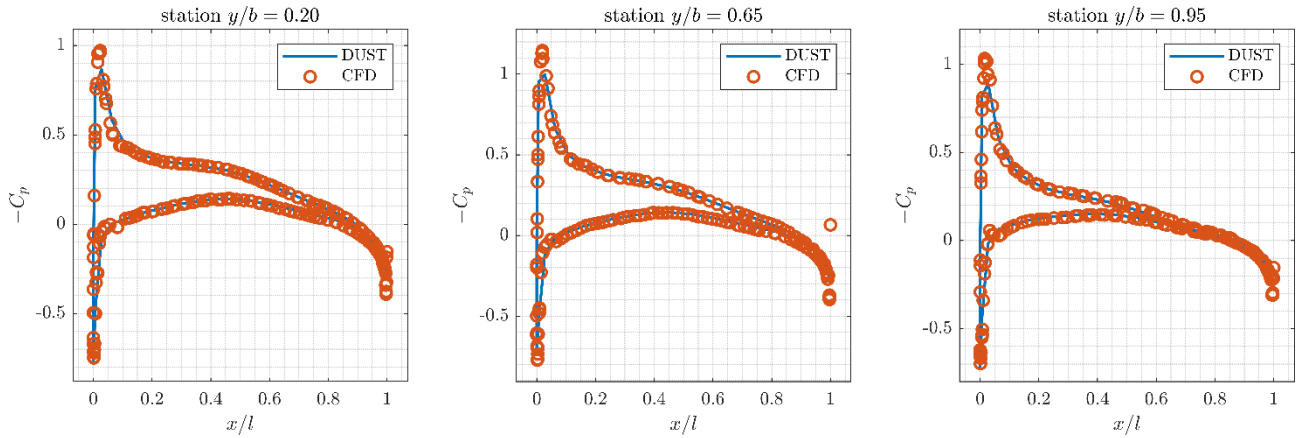


Figure 94 – ONERA M6 chordwise pressure distribution at Mach 0.3000 and AOA 3.06°

A.8.5. Transonic Testing

The flow condition chosen for the transonic testing has been the same used in the original research paper written by V. Schmitt and F. Charpin [32]. This choice has been made to have the possibility to compare our computational results with some reliable experimental data. The angles of attack considered have been the same as the subsonic test. Further information on the free stream condition can be found in Table 41.

Mach [-]	Static pressure [Pa]	Temperature [°C]	α [°]	β [°]
0.84	99974	15	0	0
0.84	99974	15	3.06	0
0.84	99974	15	6.12	0

Table 41 – ONERA M6 transonic testing free stream condition

Once again, the simulations have been executed with different open-source aerodynamic codes. In this case the expected result is to see some noticeable difference between low to mid fidelity method and high fidelity (CFD). When reporting C_L , C_D and C_M values over the angle of attack is clear that inconsistency between these methods is no longer negligible.

The presence, as expected in a transonic regime, of shockwaves over the surface of the wing introduces significant effects of compressibility. This is why potential flow methods like AVL, XFLR5 and DUST which rely only on the Prandl-Glauert transformation to apply a small correction to their results disagree with what is obtained with the Euler method.

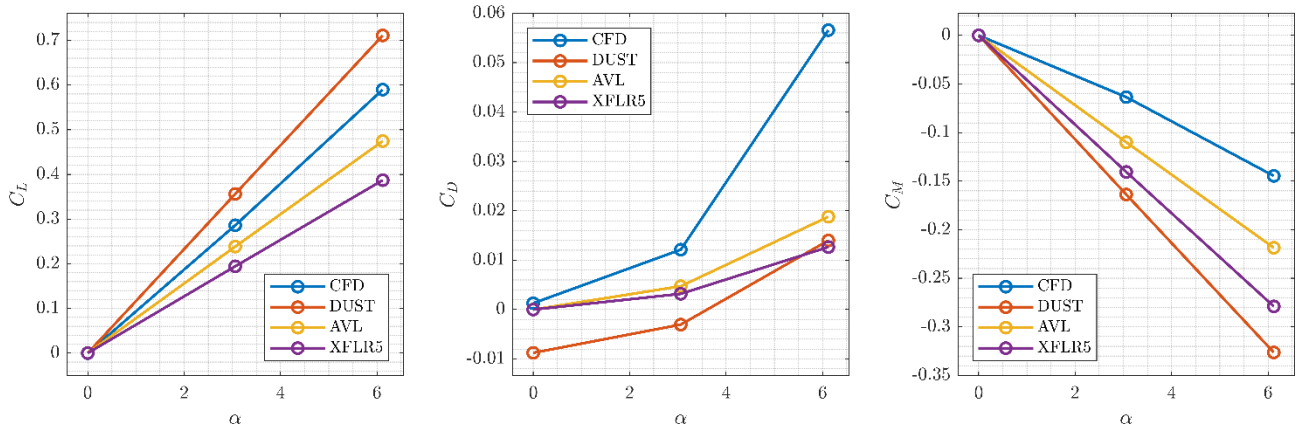


Figure 95 – ONERA M6 integral loads at Mach 0.84 and AOA 3.06°

The accuracy of the latter is further evident when considering once again the pressure coefficient distribution over the wing.

The image below clearly highlights the inaccuracies of the DUST method in a transonic case: the left side of the wing fails to capture any effects of shockwaves. This is something which perfectly aligns with our initial project conditions and hypothesis.

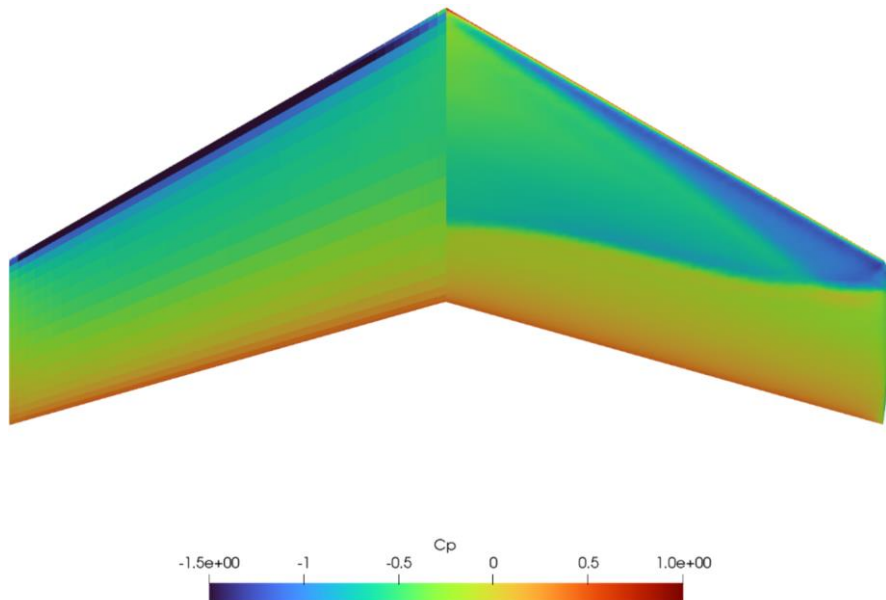


Figure 96 – ONERA M6 surface pressure distribution at Mach 0.84 and AOA 3.06°

What remains important to consider as a significant result from this comparison is how closely the SU2 Euler code aligns with the experimental curve obtained from wind tunnel tests by V. Schmitt and F. Charpin. While discrete CFD results may not match the wind tunnel outcomes at every point, it is evident that at least the overall trend is accurately captured.

We can in fact find in the Euler equations an effective method for capturing shockwaves effects even though it does not account for viscous effects such as boundary layer formation, skin friction, and heat transfer, which are crucial in high Reynolds number flows and in accurately predicting drag and thermal effects in aerodynamics.

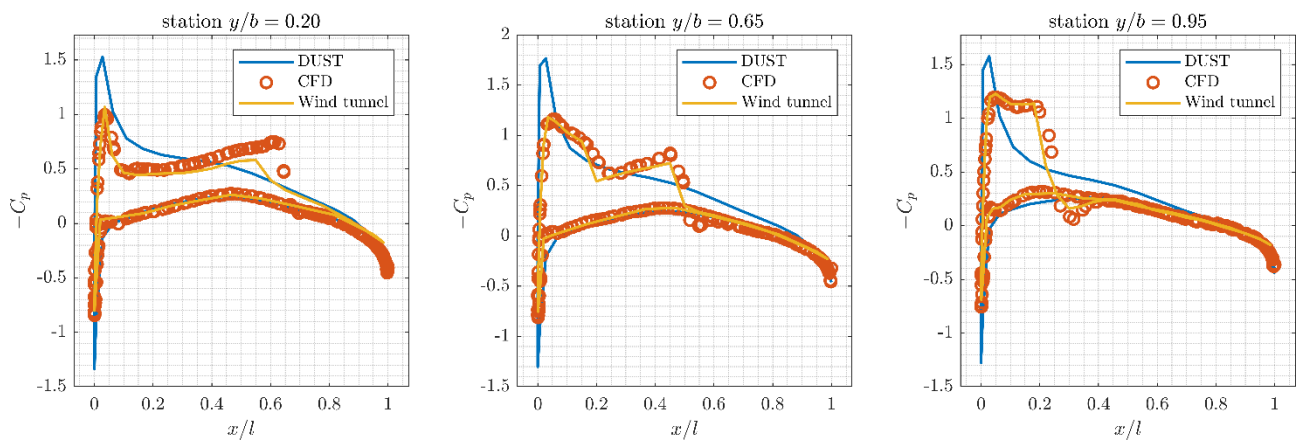


Figure 97 – ONERA M6 chordwise pressure distribution at Mach 0.84 and AOA 3.06°